Modeling and Control of Rapid Cure in Polydimethylsiloxane (PDMS) for Microfluidic Device Applications

by

Eehern J. Wong

B.S., Electrical Engineering (2002)
M.S., Electrical Engineering (2003)
Stanford University

Submitted to the Department of Mechanical Engineering
in Partial Fulfillment of the Requirements for the Degree of

DOCTOR OF PHILOSOPHY IN MECHANICAL ENGINEERING

at the

MASSACHUSETTS INSTITUTE OF TECHNOLOGY

June 2010

Signature of Author: .....
Department of Mechanical Engineering
May 19, 2010

Certified by: .....
Jung-Hoon Chun
Professor of Mechanical Engineering
Thesis Supervisor

Accepted by: .....
David E. Hardt
Professor of Mechanical Engineering
Chairman, Department Committee on Graduate Students

Modeling and Control of Rapid Cure in Polydimethylsiloxane (PDMS) for Microfluidic Device Applications

by

Eehern J. Wong

Submitted to the Department of Mechanical Engineering
on May 19, 2010 in Partial Fulfillment of the Requirements for the Degree of
Doctor of Philosophy in Mechanical Engineering

ABSTRACT

Polydimethylsiloxane (PDMS) is an important thermosetting elastomer for microfluidic devices because it can replicate nano-scale features and form flexible membranes useful for microactuation. PDMS is used extensively in research environments because it is readily available and biocompatible. However, the prototyping process is too slow for volume manufacturing. The dominant rate limiting step is curing, and high temperature cures used to speed the curing process have adverse effects on the shape of the parts produced. This thesis examines the PDMS cure process and presents a methodology to intelligently design faster cure processes without compromising the quality of parts produced.

The first part of this thesis applies statistical mechanics to relate the time evolution of cure with the modulus of elasticity. This enables mechanical testing strategies to be used *in situ* to monitor the extent of cure, which is important to determine the critical gel point and quantify when the cure process is complete. The gel point describes when PDMS first transitions from a liquid to a solid, and is important for modeling shrinkage and warpage. A novel heated micro-indentation setup is designed to monitor curing of thin PDMS films, and experimentally validate the theory.

The second part of this thesis presents a model for final PDMS shrinkage and warpage using the gel point. Gelation is spatially and temporally distributed, and temperature at the gel point has a direct impact on the shrinkage and warpage observed. The model is validated with experimental data. Since gel temperature is the only parameter to affect shrinkage and curvature, the cure process is accelerated after the gel point without affecting dimensional quality. Increasing the process temperature immediately following gelation is indeed shown to decrease the current cure process time by a factor of five, while maintaining comparable quality. Tolerances on shrinkage and curvature can be used with these models to determine the gel temperatures required, and design multi-temperature processes that speed the cure process.

Thesis Committee:

Prof. Jung-Hoon Chun (Committee Chair), Department of Mechanical Engineering
Prof. David E. Hardt, Department of Mechanical Engineering
Dr. Daniel E. Whitney, Engineering Systems Division

ACKNOWLEDGEMENTS

I wish to thank all the people who have helped, supported, and guided me throughout my experience at MIT. This thesis is a culmination of their time and efforts and would not have been possible without them.

First and foremost, I would like to thank my advisor Professor Jung-Hoon Chun. I value his patience and guidance as a mentor, and will treasure his teachings over the past four years. I would also like to thank Professor David Hardt and Dr. Daniel Whitney for serving on my thesis committee. They have provided continual guidance over my thesis, and invaluable suggestions that have undoubtedly improved the clarity of the work.

I would like to thank the Singapore-MIT Alliance (SMA) Flagship Research Program (FRP) for funding this research, and providing the opportunity to visit and collaborate with all of the wonderful faculty and students in Singapore.

I have enjoyed the warmth of all of the faculty and students involved with the Center for Polymer Microfabrication (CPM). In particular, I would like to thank Aaron Mazzeo, with whom I have spent endless hours discussing all matters PDMS. Matt Dirckx and Hayden Taylor have also been wonderful resources for knowledge, and provided great insights into many research questions. I would also like to thank Shawn Chester for his dynamic personality, and frequent help with all of the mechanical testing equipment.

The LMP staff has been tremendous during my stay at MIT. Gerry Wentworth and Pat McAtamney have always taken the time to teach best practices, and help me around the LMP machine shop. Erica McDaniel and Rachel Russell have always been extremely helpful in large purchase orders, and shielded me from complexity of so many administrative details.

To the many students who have passed through the LMP Graduate Student Office, I would like to thank all of them for their friendly faces and the lunches we have shared together. In particular, I wish to thank Aaron Mazzeo, Kevin Miu, and Michael Cullinan, who have been instrumental in the success of the LMP socials, weekly LMP basketball games, and the new friendships forged in these activities.

My labmates Catherine Mau, Thor Eusner, and AJ Schrauth, have been with me since the beginning of my time at MIT, and I thank them for always sharing their research and personal wisdom. They have always added extra color to the workplace, and have become my family away from home. I thank them for so many memories that I will cherish.

I would like to thank my friends in California who have continued to support me from afar. Serena Wong, Alan Chen, and Alex Tung have always provided wonderful inspiration with their experiences in the PhD program. And every year I look forward to new and exciting ski and camping trips that would not have been possible without the efforts of PJ Balin, David Gutierrez, Hang Lauv, Gloria Wong, and Janet Cheng.

I wish to thank my best friend John Lin, for always providing a welcome distraction.

Finally, I am grateful to my parents and my sister Luchin for their unconditional love. I appreciate all the sacrifices they have made to open opportunities and provide new experiences that have enriched the quality of my life.

CONTENTS

FIGURES

TABLES

CHAPTER

1

INTRODUCTION

1.1 Background

One could say that the origin of the microfluidic device can be traced back to a miniaturized gas chromatography system developed at Stanford University in 1979 [1]. A major motivation of the work was the ability to reduce laboratory scale machines down to pocket sized devices. In the spirit of integration, over the years microfluidic devices have become an interdisciplinary field involving chemical analysis, molecular biology, and microelectronics [2]. Today, many devices in the field of microfluidics are now called lab-on-chip (LOC) devices or micro total analysis systems (μTAS) because of their widespread use in biological experiments and chemical analysis.

Many microfluidic devices can be categorized into four major product groups: assays, cytology, proteomics/genomics, and surface patterning [3]. Assays are devices that mix reagents of many different proportions. They are generally used in the field to test properties of an unknown substance. Miniaturization has the effect of requiring smaller quantities of typically expensive reagents. More complex microfluidic chips are even capable of processing several different tests in parallel, increasing the speed to determine a particular result.

Cytology is the study of cells, and generally involves exposing cells to different environments and studying their response. This can be useful for testing how drugs interact with human cells, or for growing and sorting cells with different properties. Cells are typically on the order of 10 μm, and microfluidic channels are of the same length. Consequently, microfluidic devices can be used to sort, capture, and study each cell individually. Laminar flow, which is also characteristic at these length scales, enables cells to be moved repeatedly and predictably. Again, using smaller quantities of cells and reagents can be advantageous, especially when the

cells are rare or difficult to obtain.

Proteomics is the study of proteins, while genomics is the study of genetic information stored in DNA and RNA. A good understanding of both allows scientists to detect hereditary information early, and preemptively treat diseases. The human genome project took 13 years to map the sequence of human DNA. New DNA sequencing on a chip [4] and other DNA analysis tools [5] are capable of accomplishing the same task faster and cheaper because of smaller and lower cost reagent supplies.

In surface patterning, channels are formed above a planar surface, and biological material is transferred from the fluid to the surface. Channels can subsequently be removed from the surface, leaving a distinctive pattern of biological materials. For example, cells patterned in this way can be appropriate as biosensors, or used for drug screening [6]. Many self assembled monolayers can also be patterned to perform as surface coatings for wetting and adhesion, or as biological sensors integrated into microfluidic systems [7].

All of these applications require substrates to be patterned with micron scale features, and enclosed to form channels or wells that direct the flow of fluids. All features on the chip are usually patterned to the same depth. An example micromixer chip, developed as part of the collaborative μFAC teaching center at MIT [8], is schematically shown in Figure 1-1. Typically, one side of the device is patterned, as in Figure 1-1a, and then bonded with a flat cover plate to enclose the features, as in Figure 1-1b. Fluids can be delivered into the chip by piercing the surface of the assembled unit shown in Figure 1-1b, and connecting syringes to the two circular input wells on the right side of the chip. The fluids can then be mixed through the long serpentine channel, and purged through a pierced hole in the circular output well on the left.

A typical cross-section of an individual channel is shown in Figure 1-2a, and enclosed in Figure 1-2b. The two layers of the device can be made with same or different materials, as long as there is a method to bond the two layers together. Typical width and height dimensions are on the order of 10 to 100 μm, and result in laminar flow behavior because of their small size scales. The Reynolds number, Re, is defined below, where ρ is density, V is the velocity of the fluid, D_h is the hydraulic diameter, and μ is the dynamic viscosity of the fluid. Reynolds numbers of less than around 2000 are used to describe laminar flow.

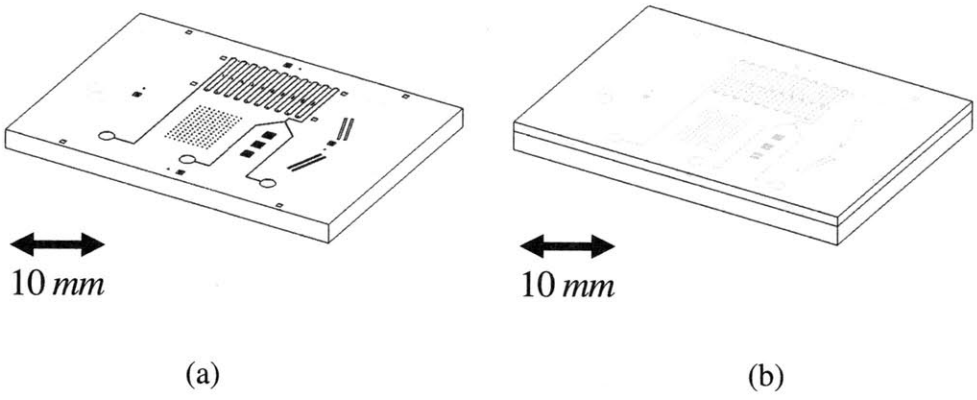

Figure 1-1: The μFAC micromixer (a) patterned into a substrate and (b) assembled.

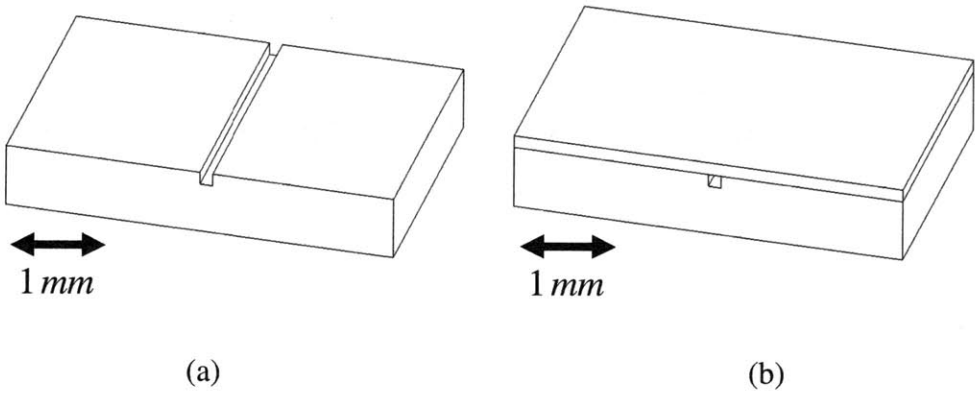

Figure 1-2: Cross-section of a typical microfluidic channel (a) patterned into a substrate and (b) enclosed to form a fluidic pathway.

$$\mathrm{Re} = \frac{\rho V D_h}{\mu} \tag{1.1}$$

Water has density of approximately 1000 kg/m^3, and dynamic viscosity of 1 mPa-s. For water flowing in a channel with a hydraulic diameter of 100 μm, we find that microfluidic chips exhibit laminar flow characteristics for flow rates of up to 23 m/s. Less than 1 MPa of pressure is typically used to drive fluid flow in these small channels, so rates are closer to 1 cm/s and well within the laminar regime [9].

Several different patterning techniques exist to transfer a micro-scale pattern into a substrate. Although a wealth of knowledge from micro-electronics exists on how to pattern silicon, material and fabrication costs are high and cost prohibitive for creating disposable microfluidic devices. On the other hand, plastics are significantly less expensive and are already used for many disposable low cost products. Plastic microfluidic devices have been made with injection molding, hot embossing, and casting [10-12]. Injection molding and hot embossing are preferred for thermoplastics such as polymethylmethacrylate (PMMA) and polystyrene (PS), while casting processes are preferred for thermal or ultraviolet curable crosslinking polymers such as PDMS and polyurethane (PUR). Injection molding has an advantage in that it can produce parts extremely quickly, but tooling is expensive and capital costs are high. For smaller lot processes, hot embossing requires cheaper tooling and capital costs, and have the capability to go down to nano-scale features. Cast polymers have perhaps the greatest stability in shape because crosslinks limit the amount of creep. They can also replicate nano-scale features, and offer more flexibility, since in thermosets such as PDMS, the modulus of elasticity can be changed by its pre-polymer mixing composition [13-16]. The range of stiffness that can be created and its excellent replication properties make PDMS the polymer of choice for many research applications.

1.2 PDMS in Microfluidic Devices

1.2.1 The rise of polydimethylsiloxane (PDMS)

In 1993, Whitesides [17] decided to use PDMS for something he would later coin "soft lithography". In soft lithography, an elastomeric stamp is used to transfer nano-scale features

onto a new substrate. The first challenge was to find an elastomeric stamp that could be patterned with nano-scale features. Feature resolution down to 30 nm was demonstrated in 1998 [18]. Because PDMS pre-polymer was liquid at room temperature, it could flow around any micro- or nano- patterned mold. Crosslinks could then form over time, and eventually solidify the polymer in the shape of the mold. Certain variants of PDMS, particularly Dow Corning's Sylgard 184, did not experience any chemical shrinkage during crosslinking, so room temperature cures resulted in PDMS stamps that very accurately replicated nano-scale features.

The original purpose of soft lithography was to actually transfer this pattern one step further from the PDMS stamp to a subsequent film or substrate. However, the replication quality of PDMS caught the imagination of researchers from around the world. PDMS was not only a useful material capable of replicating small features, but a transparent and flexible material that was compatible with many chemical and biological processes. PDMS could itself be used as a device material for microfluidic systems.

Room temperature cures very accurately replicated the dimensions of the master tooling, but required that PDMS sit undisturbed for two days while it solidified [19]. Elevated temperatures could actually increase the cure rate of PDMS, but at the cost of dimensional stability. Shrinkage was observed to occur at higher temperatures, and thought to increase linearly with the process temperature [20]. If PDMS was cured at a temperature above ambient, it solidified at that temperature, and at that temperature and time would exactly replicate its surroundings. Subsequent cooling to room temperature would cause linear thermal contraction, and the overall part to shrink. For some applications, this shrinkage could be tolerated, and the ability to rapid prototype a single device in hours instead of days was worth the tradeoff. In the following years, PDMS became commonplace among lab-on-chip devices, although mostly as a substrate material.

Although the flexible nature of PDMS was explicitly chosen for soft lithography, nobody had exploited its flexibility for microfluidic devices until 2000, when Quake [21] published a revolutionary application. The idea was to stack multiple layers of PDMS together and create on-chip actuators. The bottom layer would be patterned with flow channels, while the top layer patterned with control channels. By placing a thin flexible PDMS layer between the control and flow layers, fluid pressurized in the control layer could be used to deform the sandwiched PDMS membrane, and close off channels in the flow layer. They had developed a new way to actuate

fluid flow; in the same way semiconductors controlled the flow of electrons, Quake was now controlling the flow of fluids. They integrated valves, pumps, and mixing chambers all on the same chip. PDMS was no longer just a low cost replacement for silicon, but also a unique material that could integrate actuation on chip.

With the innovations of Whitesides and Quake, PDMS cemented its role as the leading material for rapid prototyping. PDMS continued to be used in microfluidic devices for complex fluid routing and micro-actuation, as shown in Figure 1-3, and scores of researchers continued using this material, and found innovative ways to create novel applications. Thorsen [22] demonstrated large scale integrated fluidic chips that could be used for assays, while Leclerc [23, 24] demonstrated bioreactors that could be used for cell cultures. PDMS showed much promise as the low cost alternative to glass and silicon, and as the material that would enable commercialization of lab-on-chip devices.

1.2.2 Commercialization of PDMS microfluidic devices

Although PDMS was lauded in the research community, commercial microfluidic chipmakers had been slow to adopt PDMS as their material of choice. Becker [25] described the primary problem to be material and process variability. For applications where permeability was important, the repeatability was unreliable since crosslink density was not well controlled and was directly related to permeability [26, 27]. Furthermore, the rate of producing a single PDMS part was much slower than competing processes like injection molding or even hot embossing.

However, PDMS was unique because it was much more flexible than the thermoplastics used for microfluidic devices. Its flexibility has enabled commercial fabrication of intricate integrated fluidic circuits, which are capable of performing complex tasks on a single chip. Although these devices are currently produced in low volumes, solving the manufacturing issues related to PDMS can enable similar chip designs to be efficiently mass produced.

1.3 PDMS Device Fabrication

There are five basic steps in creating a PDMS device, which are briefly outlined below. A typical process flow is shown in Figure 1-4.

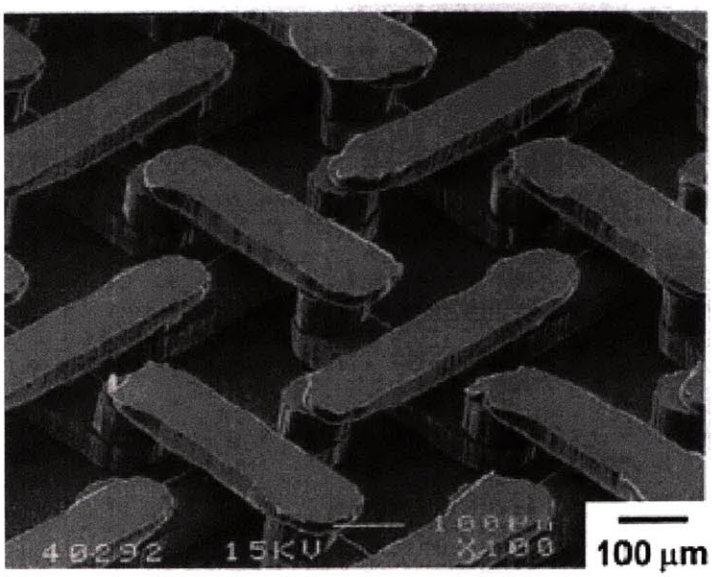

(a)

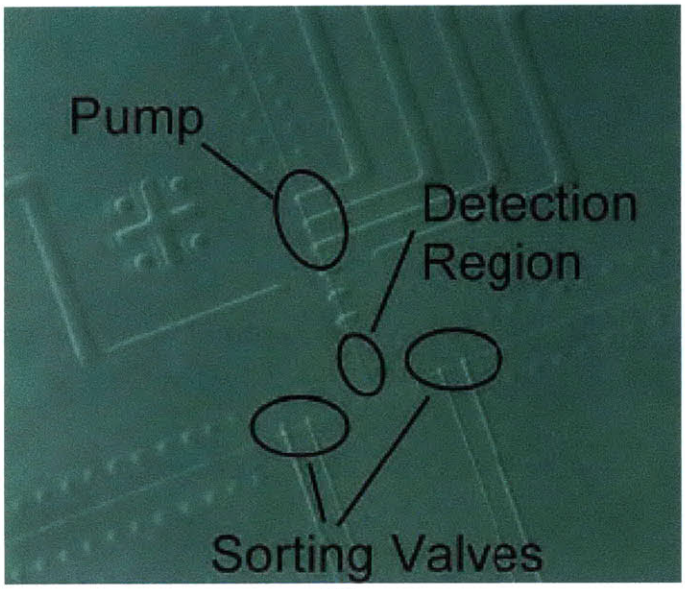

(b)

Figure 1-3: PDMS devices for (a) multilayer [28] **and (b) micro-actuation** [29] **applications.**

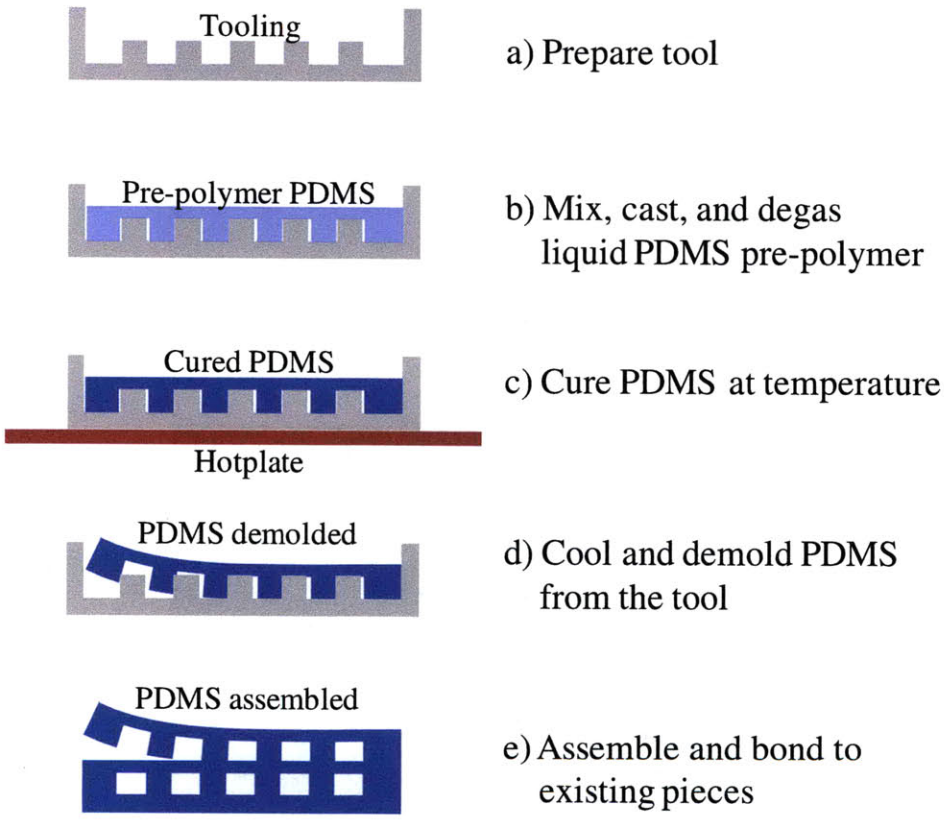

Figure 1-4: Typical PDMS process flow.

1.3.1 Tooling and surface preparation

The first step is to create tooling that can be used to pattern PDMS. Tooling can be made with nearly any material that can be patterned with micro-scale features. Some examples include silicon, thin films on silicon, micromachined aluminum, and bulk metallic glass (BMG). Micro- and nano-scale patterns can be created in silicon or films on silicon using standard microfabrication processes, but these tools are typically brittle and less robust than metal tools. Micron scale features can be micromachined into aluminum tools, but exhibit inferior surface finish because of tool marks. BMG can heated to its glass transition temperature and embossed with a patterned silicon tool, and combine the resolution and surface finish of a silicon tool with the robustness of a metal tool. However, these tools are expensive, and their costs can be prohibitive if tooling is changed frequently. For tools that are less robust, additional demolding agents can be added to the tool surface to extend the life of the tool. These tools are typically assembled into a mold, as shown in Figure 1-4a, into which a liquid pre-polymer can be cast.

1.3.2 Casting and degassing

The second step is to cast and degas PDMS. PDMS is typically provided as a multi-part liquid pre-polymer, and is mixed and poured into a mold as shown in Figure 1-4b. The mixing and casting process introduces bubbles, which are removed by a degassing step. Degassing is typically done in a vacuum chamber for 30 minutes, or industrially with a Thinky mixer for three minutes. However, degassing can be expedited using centrifugal casting techniques described by Mazzeo [12]. Furthermore, centrifugal casting and degassing can be integrated into a single step to reduce this time further.

1.3.3 Thermal curing

Solidification is accomplished by heating the liquid pre-polymer. The recommended cure time for Dow Corning Sylgard 184 is 2 hrs at 65C. Increasing the process temperature increases the cure rate, so this time can be reduced to 1 hr at 75C or 30 minutes at 85C. Similarly, decreasing the process temperature to room temperature increases the cure time to two days. Although higher process temperatures increase the process rate, shrinkage is observed, and this reduces the replication quality of the part. Hotplate curing is shown schematically in Figure 1-4c, although convection ovens are also commonly used for curing. The heating strategy used affects

the spatial temperature profile experienced by the part, and we will show that this can have a direct impact on the shape or curvature of the produced part.

1.3.4 Demolding

Once fully cured, the PDMS part is removed from the mold. Because of its flexible nature, PDMS is often peeled from the mold manually, as in Figure 1-4d, although liquid parting and other alternatives have been proposed by several researchers [12, 30, 31]. PDMS is an elastomer, so large strains during demolding do not permanently change the final geometry of the part. However, PDMS is prone to tearing, so excessive demolding stresses may tear thin membranes produced with PDMS.

1.3.5 Assembly

After PDMS is demolded, it is usually assembled and bonded with additional layers to form a usable device. Today, assembly is generally performed by hand, where one PDMS part is rolled onto another, as shown in Figure 1-4e. Overlay issues occur when both parts experience different shrinkages from the thermal curing process, and manual stretching is required to align the parts as best as possible. This process is tedious, and the final alignment of the parts depends entirely on the skill of the operator. The manual assembly process introduces additional distortion to the sample pattern. To eliminate user-induced distortion, the assembly process will eventually become automated, and process-induced warpage will need to be quantifiably compensated for.

Furthermore, the effects of stretching on bonding have not been studied thoroughly. Bonding of PDMS is generally performed in one of three ways. First, two PDMS parts exposed to oxygen or air plasma will bond spontaneously upon contact, making it difficult to compensate for shrinkage mismatches. Second, two parts cured with different ratios of PDMS base to curing agent can be made, and pressed together to form a reversible seal. This allows misalignment issues to be corrected, albeit a tedious manual process, and then made permanent by subsequently baking the assembled part. Third, PDMS can form a conformal seal with smooth substrates such as silicon or glass. These seals are reversible, but can only support low fluid pressures. However, they are useful for surface patterning applications when the PDMS channels need be removed from the substrate. In all three cases, shrinkage mismatches can lengthen the

bonding process or create unusable devices. Furthermore, bowing or warpage due to non-uniform shrinkage can trap air bubbles, which can reduce feature fidelity and potentially decrease the quality of the bond.

1.4 Thesis Organization

This thesis is organized to tackle the cure process design problem. In the process flow shown in Figure 1-4, the dominant rate limiting step is curing. The goal is to produce a process that can reduce the time required to cure, while maintaining same or better quality. To accomplish this, quality metrics will be defined to provide constraints on the process, and the necessary manufacturing knowledge will be developed to design a faster multi-temperature cure.

Today, the thermal cure process in Figure 1-4c is commonly performed at a single process temperature T_1 for a total process time of t_1, as shown in Figure 1-5. Although this process time varies depending on the application and researcher, it is commonly stopped when PDMS is sufficiently "firm to touch" [32]. Increasing process temperature to T_2 or T_3 has the effect of decreasing the total process time to t_2 or t_3 that will achieve the equivalent stiffness. Although this process requires days at room temperature, increasing the temperature increases the reaction rate, and is often adopted to reduce the process time. Table 1.1 shows hold times that have been successfully used by different researchers at different temperatures.

The cure process time is also rarely carefully controlled. For instance, in some cases PDMS is allowed to cure overnight at 65C [33], while in other cases PDMS is cured to 2 hours at 65C [34]. Part of the reason is due to "convenience" [33], while part of the reason is simply due to inability to quantify the end product. Consequently, parts that are not carefully cured experience an aging effect [14, 35]. Some researchers compensate for this problem by adding a second high temperature cure [36], but the transition point is not optimal and adds to the total length of a single temperature cure process.

The first part of this thesis quantifies when the end product is sufficiently cured, and when the process is complete. This provides a fair comparison of two different cure processes. Curing is a chemical crosslinking process that converts liquid PDMS to a solid, and the percentage of crosslinks formed during the cure process is given by the cure extent p. The transition point when PDMS begins to behave as a solid instead of a liquid is called the gel point, and from this point forward the modulus increases from zero asymptotically towards its fully

Table 1.1: Typical cure times (minutes) of Sylgard 184.

Source	25C	65C	80C	85C	100C	125C	150C
[19]	2880	-	-	-	35	20	10
[20]	-	240	-	120	60	-	-
[37]	720	90	-	-	-	-	-
[38]	-	-	150	-	-	-	10

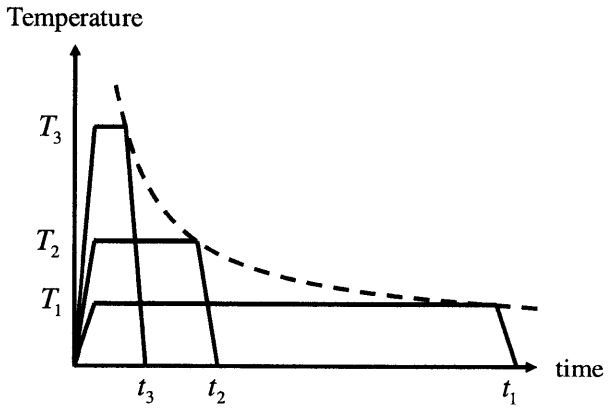

Figure 1-5: Current single temperature PDMS cure cycles. Higher temperature cures can be held for shorter periods to achieve equivalent extents of cure.

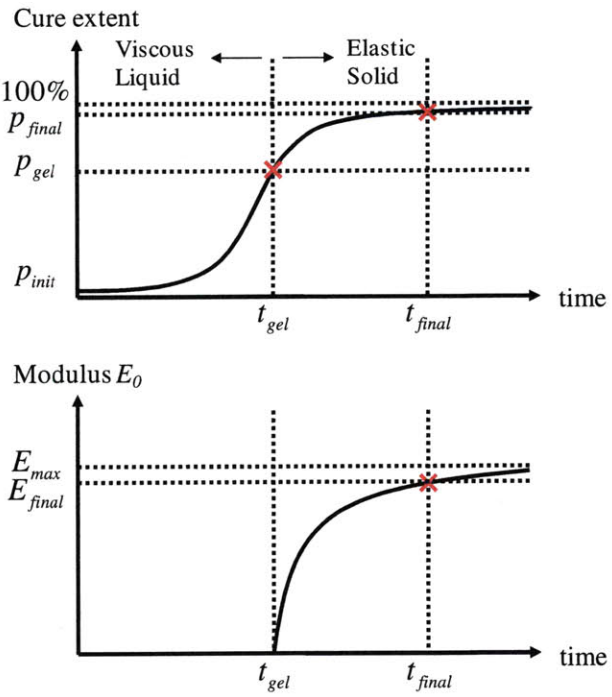

Figure 1-6: Cure extent and modulus over time asymptotically approach their fully crosslinked values.

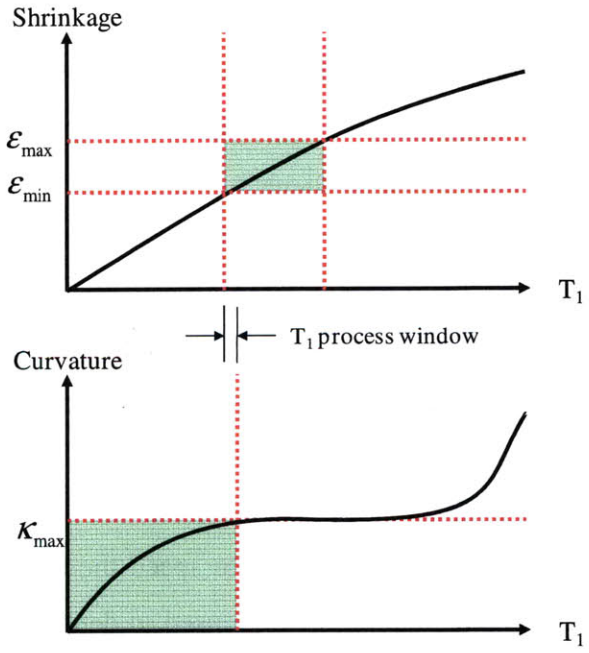

Figure 1-7: Specifications on shrinkage and curvature can be used to determine the range of process temperature T_1 which can be used.

cured value E_{max}, as shown in Figure 1-6. Since this value is approached but never reached, time aged PDMS has been shown to increase in modulus over time [14]. Consequently, to limit the modulus variability of cured parts, PDMS should be cured to a modulus E_{final}, specified as a large percentage of E_{max} and be used to quantify when the cure process is complete. Determination of E_{max} and the time evolution of modulus and cure is the subject of Chapter 2. In Chapter 3, these models are experimentally validated, and heated micro-indentation is introduced as a tool to mechanically monitor the cure extent during the cure process.

Next, in order to produce the same part with different cure processes, the part is required to have the same shape at the end of both processes. Shape change is a result of shrinkage ε, which occurs during the cure process. Out of plane shrinkage variations throughout the part can also cause warpage, which can be quantified by part curvature κ. In Chapter 4, shrinkage and curvature are found to change with process temperature. It is postulated and later shown that dimensional changes to part geometry are affected by the temperature at which gelation occurs. Unlike the glass transition temperature and melting temperature in thermoplastics, which are intrinsic material properties, this gel temperature is process dependent. If the process is designed such that the gel temperature is very close to ambient, there will be very little shrinkage or warpage. The spatial and temporal distribution of the gel point inside the part is modeled and used to generate a mathematical model of shrinkage and curvature dependence on process temperature. This enables the creation of shrinkage and curvature plots, schematically shown in Figure 1-7, which can be used with tolerance specifications to determine the range of process temperatures, T_1, which will yield an acceptable part. Typically a range of shrinkages may be specified, as well as a maximum curvature that can be tolerated for assembly. These are shaded green in Figure 1-7, and the process temperature overlap suggests a range of process temperatures that may be used to achieve such specifications.

Finally, because the gel temperature directly impacts the shape of the part produced, the process temperature can be increased after gelation to speed the remainder of the process. The methodologies developed in Chapters 2 and 4 can be used to determine the gel time for a given material at a particular process temperature, and enable process designers to rapidly increase the process temperature immediately after to reduce the total cure time. This combines the quality benefits of low shrinkage and curvature in a low temperature cure, with the rate benefits of a

high temperature cure. Compared with current single temperature processing conditions, the total cure process time can be reduced by up to five times with this two-temperature process, and this strategy is experimentally validated in Chapter 5.

Nomenclature

D_h = hydraulic diameter [m]

E_{max}, E_{final} = the fully cured modulus and modulus at process completion [N/m^2]

p, p_{gel}, p_{final} = cure extent, cure extent at gelation, cure extent at process completion

Re = Reynolds number

t_{gel}, t_{final} = time to gel and cure process completion [s]

t_1, t_2, t_3 = process time for single temperature cure process [s]

T_1, T_2, T_3 = process temperature for single temperature cure process [K]

V = velocity of the fluid [m/s]

ε = shrinkage

κ = curvature [m^{-1}]

μ = dynamic viscosity [Pa-s]

ρ = density [kg/m^3]

CHAPTER

2

MECHANICS OF CURE IN THERMOSETTING ELASTOMERS

This chapter models the modulus of elasticity and its relationship with cure. The first part of this chapter describes how the chemical structure of PDMS can be described by its crosslink composition. Different mixing compositions of the PDMS pre-polymer change the total number of crosslinks that are created during cure. Similarly, the number of crosslinks created during cure is directly related to the extent of cure. Using a statistical mechanics approach, Young's modulus can be described by the crosslink density, and used to monitor cure.

2.1 PDMS Pre-polymer Chemistry and Composition

PDMS pre-polymer is a viscous liquid at room temperature. The pre-polymer has a siloxane backbone, with alternating silicon and oxygen atoms. Connected to most silicon atoms are two $-CH_3$ methyl groups. However, to enable crosslinking to occur, some of these methyl groups are replaced with a hydrogen atom, or a $-CH=CH_2$ vinyl group. The methyl groups are nonreactive and experience no chemical change during crosslinking. However, the hydrogen and vinyl terminated ends react with one another under the presence of a platinum catalyst, and these functional ends form crosslinks as shown in Figure 2-1. This reaction is exothermic, and in addition to the new crosslinks formed, heat is released as a byproduct.

Dow Corning's Sylgard 184 comes as a two part pre-polymer, as shown in Figure 2-2. The MSDS datasheets suggest that the base contains vinyl terminated groups, while the curing agent contains hydrogen terminated groups and platinum catalyst. Each part is nonreactive when stored on its own, but when combined together the hydrogen and vinyl groups react and form crosslinks. Although the density of hydrogen groups in the curing agent and vinyl groups in the

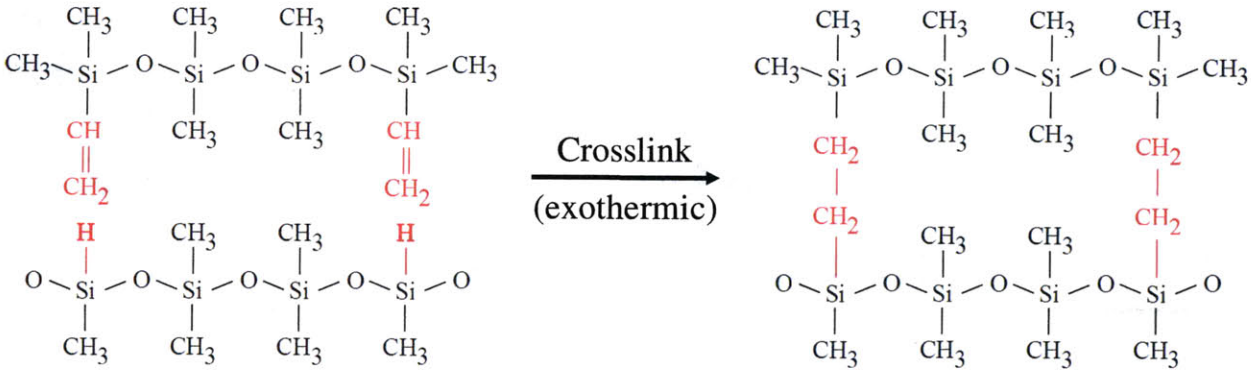

Figure 2-1: Hydrogen and vinyl terms crosslink in the presence of a platinum catalyst.

- PDMS:
  Two part liquid pre-polymers

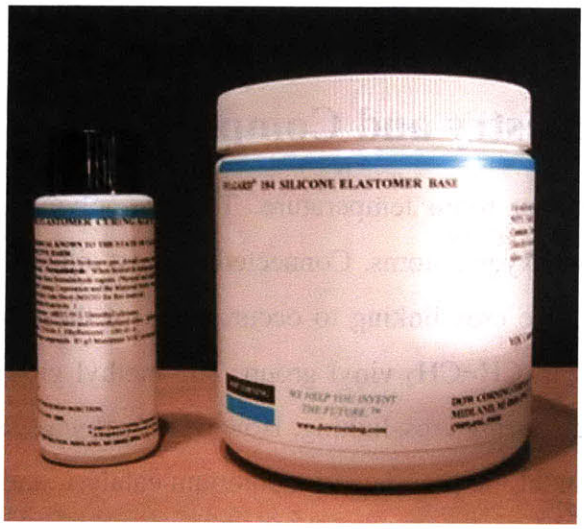

Curing Agent Base

- PDMS:
  Methyl terminated ends

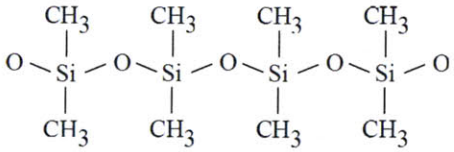

- Curing agent:
  Hydrogen terminated ends

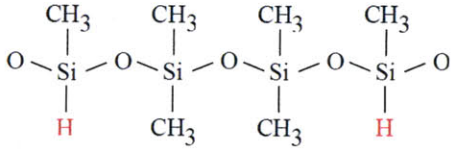

- Base
  Vinyl terminated ends

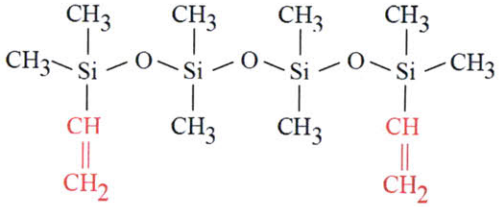

Figure 2-2: Sylgard 184 PDMS is a two part liquid pre-polymer that is non-reactive until both base and curing agent are combined.

base are proprietary, the manufacturer recommends a base to curing agent volume ratio R_{mix} = 10:1, which suggests that hydrogen and vinyl groups are stoichiometrically matched at or near this ratio. The final crosslink density when all hydrogen and vinyl groups have reacted is denoted by n_{max}. When there is excess hydrogen, as in the case of excess curing agent, the crosslink density is determined by the amount of vinyl. Similarly, when there is excess vinyl, as in the case of excess base, the crosslink density is determined by the amount of hydrogen. The final crosslink density n_{max} is the largest when hydrogen and vinyl content is equal at a mixing ratio of $R_{mix} = R_{stoich}$.

The number density of silicon bonded vinyl in the base can be defined as n_b, and the number density of silicon bonded hydrogen in the curing agent can be defined as n_c. If a volume V_b of base is mixed with a volume V_c of curing agent at a mixing ratio $R_{mix} = V_b / V_c$, the total amount of vinyl and hydrogen in the mixture is $n_b V_b$ and $n_c V_c$, respectively. The maximum number of crosslinks that can form is then equal to the minimum of these two quantities:

$$n_{max} V = \min\left(n_b V_b, n_c V_c\right) \tag{2.1}$$

where V is the total volume $V_b + V_c$, and n_{max} is the crosslink density. When all $n_{max}V$ crosslinks have formed, the cure is 100% complete. It follows that if a mixture is stoichiometrically matched,

$$n_{max} = \frac{n_b V_b}{V} = \frac{n_c V_c}{V} = \frac{R_{stoich}}{R_{stoich}+1} V n_b = \frac{1}{R_{stoich}+1} V n_c \tag{2.2}$$

If it is base limited,

$$n_{max} = \frac{n_b V_b}{V} = \frac{R_{mix}}{R_{mix}+1} V n_b \tag{2.3}$$

and if it is curing agent limited,

$$n_{max} = \frac{n_c V_c}{V} = \frac{1}{R_{mix}+1} V n_c \tag{2.4}$$

When n_{max} is normalized to the stoichimetric crosslink density n_{stoich}, the new ratio n_r reduces to a

simple function of R_{mix} and R_{stoich}. When stoichiometrically matched, $n_r = 1$, when base limited,

$$n_r = \frac{R_{mix}}{R_{stoich}}\left(\frac{R_{stoich}+1}{R_{mix}+1}\right) \tag{2.5}$$

and when curing agent limited,

$$n_r = \frac{R_{stoich}+1}{R_{mix}+1} \tag{2.6}$$

The ratio n_r is a convenient way to express the fraction of crosslinks in the current mixture to the maximum fraction of crosslinks that can be designed by altering the mixing composition.

2.2 Crosslinking, Curing, and Formation of a Solid

During the thermal cure process, the number of crosslinks increases from zero to n_{max}. The cure extent p is defined as the percentage of crosslinks that have formed:

$$n_p = pn_{max} \tag{2.7}$$

where n_p is the crosslink density at a cure extent p. Cure extent can be modeled as a reaction rate phenomenon, so the curing kinetics for Sylgard 184 can be described by an Arrhenius equation of the form

$$\frac{dp}{dt} = k(T)p^m(1-p)^n, \quad k(T) = k_0 e^{-E/RT} \tag{2.8}$$

where dp/dt is the cure rate, p is the cure extent, k_0 is the pre-exponential constant, E is the activation energy, R is the gas constant, and T is the temperature. The exponents m and n are empirical constants used to calibrate the equation. A more detailed description about the origins Equation (2.8) is found in Section 4.4.2, and calibration of its parameters is performed in Section 4.5.1. When cure occurs at a higher temperature, the cure rate increases and the cure process completes in a shorter period.

A typical progression of cure extent over time is shown in Figure 1-6. Depending on the composition of pre-polymer, the initial cure extent is usually modeled as a non-zero quantity p_{init}.

The pre-polymer initially starts as a viscous polymer with many short PDMS strands. The molecular weight of a strand describes its length, and the average molecular weight of all strands is related to viscosity. Shorter strands are more capable of flowing as a fluid, while longer strands are more likely to become entangled. As the pre-polymer crosslinks over time, strands combine and the average molecular weight of each strand increases. Consequently, viscosity increases as more crosslinks form over time. Finally, the cure reaches a point when the viscosity of the pre-polymer approaches infinite, and the material becomes an elastic solid. This is called gelation, and happens with the formation of a macromolecule. The macromolecule forms when all original strands of pre-polymer are first interconnected, as shown in Figure 2-3. At this point, each original strand is connected at two points. The functionality of a strand is defined as the number of hydrogen or vinyl groups that are connected to the strand. The original strands in Figure 2-3 are all shown to have a functionality of three. The average functionality f_{avg} of the pre-polymer can then be used to estimate gelation with the Carothers Equation [39]:

$$p_{gel} = \frac{2}{f_{avg}} \tag{2.9}$$

For PDMS, the average functionality is approximately three, and the gel point $p_{gel} = 67\%$ [40].

At the gel point, each of the original strands is connected to the macromolecule by two crosslinks. The crosslink density is n_{gel}. The macromolecule is consequently modeled as an infinite length polymer chain. If each original pre-polymer strand is modeled as a spring, the macromolecule becomes nearly an infinite chain of springs in series and has nearly zero stiffness. However, crosslinks formed after gelation internally connect the macromolecule. As the number of crosslinks increases, some chains of springs in series shorten and become springs in parallel, and the modulus grows towards the fully cured stiffness. Shown in Figure 2-4, more crosslinks prevent the polymer from stretching as much under the same load. The incremental crosslink density above gelation is usually related to the chain density n, since $n/2$ crosslinks subdivide the macromolecule into n chains. This chain density has a value between 0 and $n_{max} - n_{gel}$, and can be related to cure extent by

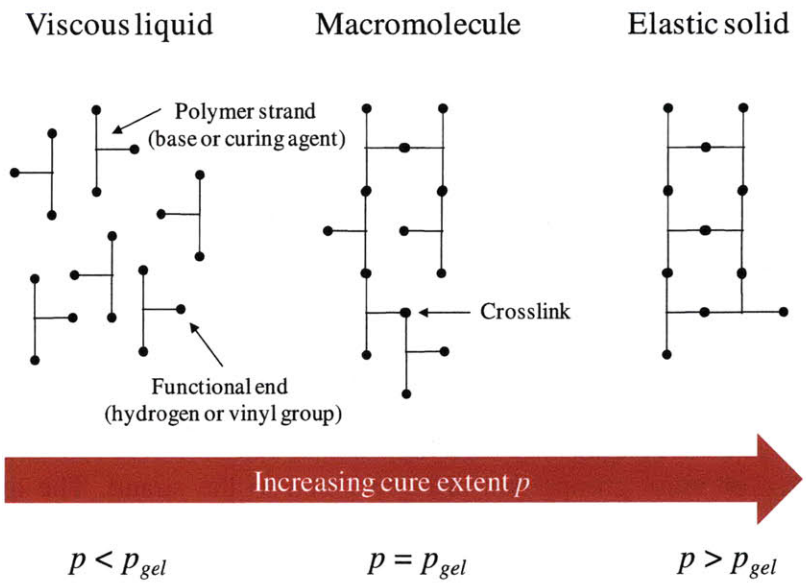

Figure 2-3: As the viscous pre-polymer crosslinks, the polymer strands become a part of a single macromolecule at the gel point. Thereafter, crosslinks continues to stiffen the macromolecule until all potential crosslinks are formed.

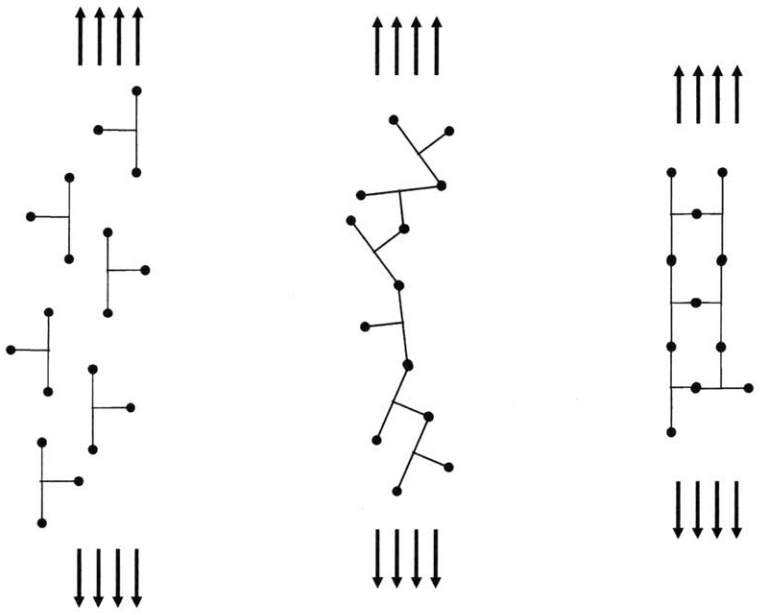

Figure 2-4: Young's modulus in the polymer distinctly increases after the macromolecule is formed.

$$n = \frac{p - p_{gel}}{1 - p_{gel}}\left(n_{max} - n_{gel}\right) = \left(p - p_{gel}\right)n_{max} \tag{2.10}$$

The chain density relation is useful for relating crosslink density to modulus, and will be used in Section 2.3. It is also useful for us to define a reduced cure extent p_r as the percentage of chains produced:

$$p_r = \frac{p - p_{gel}}{1 - p_{gel}} \tag{2.11}$$

2.3 Statistical Mechanics Approach to Modeling Modulus

Statistical mechanics is a method used to model the deformation of polymers. Meyer was first to apply statistical mechanics to the chain-like structure in polymers [41]. His major realization was that polymer networks could be modeled by a chain of N links of length l, where each link could essentially rotate freely. The orientations of these links were statistically modeled with probability density functions, and summed to determine the final length and orientation of the chain. The average length of the chain was found to be $\sqrt{N}l$, and in Gaussian statistics, the force required to stretch the chain was assumed to be linear to the stretch λ. In actuality, the maximum length of the chain was Nl, and the force required to stretch the chain near this fully stretched length was much larger than predicted using Gaussian statistics. Using Langevin statistics, this force required to stretch the chain was modeled nonlinearly as a function of the inverse Langevin function, and approached infinity as the chain approached length Nl. Figure 2-5 shows a small portion of a crosslinked polymer with two crosslinks. The incremental number of crosslinks after gelation divides the macromolecule into n chains. On average, each chain is modeled as a series of N rigid links of length l.

To more accurately model the actual polymer, these Langevin chains were arranged in multi-chain networks. Wang and Guth [42] proposed a three chain network, Flory and Rehner [43] proposed a four chain network, and Arruda and Boyce [44] proposed an eight chain model. For rubber elastic materials, the Arruda-Boyce model was found to most accurately match experimental results, and required only two parameters, both of which were physics based [45].

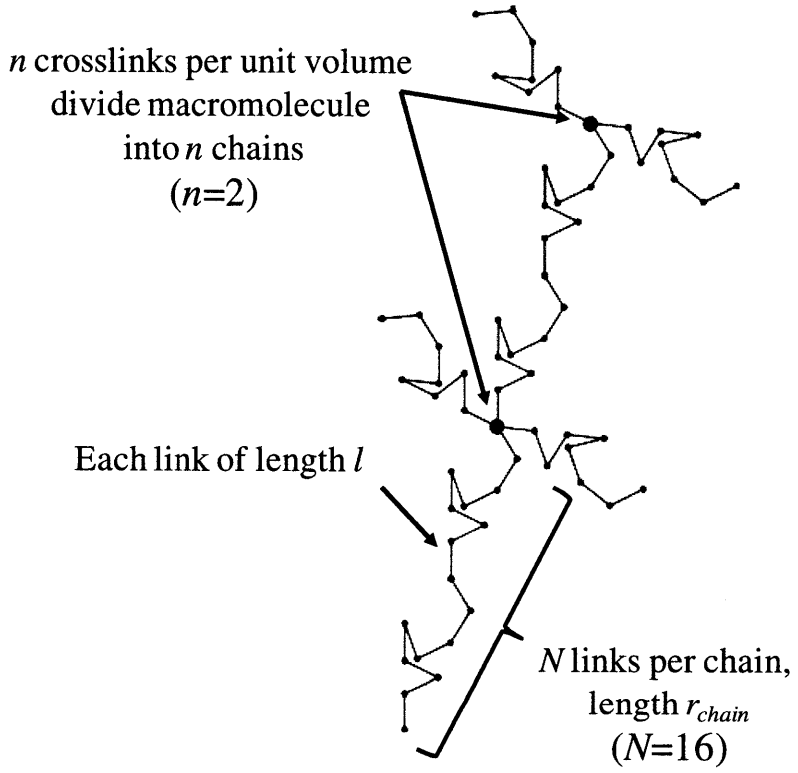

Figure 2-5: Model of a polymer with two crosslinks.

These models were indeed better at capturing the three-dimensional stress-strain relationship of rubbers, however they were more difficult to analyze analytically. To determine the model complexity that is necessary with PDMS, we compare the simplest three chain Gaussian network with the Arruda-Boyce Langevin network. Strain energy formulations of these statistical models are useful, since modulus can be directly extracted and easily compared with that from mechanical testing experiments.

2.3.1 Gaussian network model of polymer elasticity

The most basic approach is to assume Gaussian statistics. If the chain density is n chains per unit volume, the strain energy density can be computed by combining n of these together. Summing the strain energy density in each of the three axes, the strain energy function W is estimated by Equation (2.12), where k is the Boltzmann's constant, and T is temperature [41].

$$W = \frac{1}{2} nkT\left(\lambda_1^2 + \lambda_2^2 + \lambda_3^2 - 3\right) \tag{2.12}$$

To determine Young's modulus for isotropic materials, the stress-stretch relation for uniaxial stress is examined with $\lambda_2 = \lambda_3$. For elastomers, incompressibility is also assumed with $\lambda_1 \lambda_2 \lambda_3 = 1$, and simplifies the strain energy equation to

$$W = \frac{1}{2} nkT\left(\lambda_1^2 + \frac{2}{\lambda_1} - 3\right) \tag{2.13}$$

For incompressible deformation, the stress equation also reduces to Equation (2.14), where pressure $p_{pressure}$ is determined by equilibrium and $i = 1, 2, 3$.

$$\sigma_i = \lambda_i \frac{\partial W}{\partial \lambda_i} + p_{pressure} \tag{2.14}$$

To eliminate pressure, it is common to express the stress equation as the difference of two principal stresses in Equation (2.15).

$$\sigma_1 - \sigma_2 = \lambda_1 \frac{\partial W}{\partial \lambda_1} - \lambda_2 \frac{\partial W}{\partial \lambda_2} \tag{2.15}$$

Applying Equations (2.13), Equation (2.15) reduces to Equation (2.16).

$$\sigma_1 = nkT\left(\lambda_1^2 - \frac{1}{\lambda_1}\right) \tag{2.16}$$

Young's modulus is given by differentiating uniaxial stress by strain in Equation (2.17).

$$E = \frac{d\sigma_1}{d\varepsilon_1} = \frac{d\sigma_1}{d\lambda_1} = nkT\left(2\lambda_1 + \frac{1}{\lambda_1^2}\right) \tag{2.17}$$

Finally the initial modulus E_0 is defined as the modulus evaluated at the unstretched state in Equation (2.18).

$$E_0 = \left.\frac{d\sigma_1}{d\lambda_1}\right|_{\lambda_1=1} = 3nkT \tag{2.18}$$

In Gaussian statistics, Young's modulus is found to be directly proportional to n, the crosslink density past gelation.

2.3.2 Eight chain network with Langevin statistics

A Gaussian chain behaves similarly to a linear elastic spring: the force required to stretch a chain is directly proportional to the incremental stretch. Theoretically this allows chain lengths to be infinitely large with some finite stretch force. In real thermoset polymers, the maximum length per chain is constrained by the total number of links. Consequently, stresses increase dramatically for strains close to the maximum extensibility limit, and the chain behaves more like a nonlinear elastic spring. Langevin statistics, first described by Kuhn and Grun [46], captures this effect.

In Langevin statistics, the strain energy function for a single chain can be described by Equation (2.19) [45]. This is derived from the entropy of a stretched chain of length r_{chain}. The quantity β is physically proportional to the force Z required to stretch a chain from its average

unstretched length $\sqrt{N}l$ to a length r_{chain}. The quantity c' combines remaining constants that are independent of r_{chain}.

$$W_{chain} = nkT\left(\frac{r_{chain}}{Nl}\beta + \ln\frac{\beta}{\sinh\beta}\right) - Tc', \quad \beta = \frac{Zl}{kT} \tag{2.19}$$

To solve for Z as a function of the chain length r_{chain}, the inverse Langevin function is required. The Langevin function is defined in Equation (2.20), and equals the ratio of the chain length to the maximum chain length, from the work of James and Guth [47].

$$\mathcal{L}(\beta) = \coth\beta - \frac{1}{\beta} = \frac{r_{chain}}{Nl} \tag{2.20}$$

For small values of β, the output is linear, but as $\beta \to \infty$, the output approaches 1. This effectively models the extensibility limit in which r_{chain} has a maximum chain length of Nl.

Applying the eight chain network geometry proposed by Arruda-Boyce, r_{chain} is related to λ_{chain} according to

$$\lambda_{chain} = \frac{r_{chain}}{\sqrt{N}l} \tag{2.21}$$

where λ_{chain} is defined as the total stretch from all three spatial stretches in Equation (2.22).

$$\lambda_{chain} = \sqrt{\frac{\lambda_1^2 + \lambda_2^2 + \lambda_3^2}{3}} \tag{2.22}$$

The maximum stretch is defined as the locking stretch and computed as the maximum chain length to the average chain length: $\lambda_L = \sqrt{N}$. Thus, as $\lambda \to \sqrt{N}$, $\beta \to \infty$ so the inverse Langevin function can be used to represent large increases in stress as polymer chains approach the locking stretch.

$$\mathcal{L}^{-1}\left(\frac{\lambda_{chain}}{\sqrt{N}}\right) = \beta, \quad 0 < \frac{\lambda_{chain}}{\sqrt{N}} < 1 \tag{2.23}$$

Stress is obtained by substituting Equations (2.15), (2.19), and (2.21) into Equation (2.24).

$$\sigma_1 - \sigma_2 = \frac{nkT\sqrt{N}}{3} \mathcal{L}^{-1}\left(\frac{\lambda_{chain}}{\sqrt{N}}\right)\left(\frac{\lambda_1^2 - \lambda_2^2}{\lambda_{chain}}\right) \tag{2.24}$$

As before, initial Young's modulus is determined by differentiating uniaxial stress by strain. The inverse Langevin function is approximated to four terms by Treloar [41] with a Taylor series expansion as

$$\mathcal{L}^{-1}(\lambda) = 3\lambda + \frac{9}{5}\lambda^3 + \frac{297}{175}\lambda^5 + \frac{1539}{785}\lambda^7 + \ldots \tag{2.25}$$

This method is used by Arruda-Boyce to compute the strain energy function below [45], where I_1 is the first invariant of the left Cauchy Green Tensor, and defined by $I_1 = \lambda_1^2 + \lambda_2^2 + \lambda_3^2 = 3\lambda_{chain}^2$:

$$W = nk\Theta\left[\begin{array}{l}\frac{1}{2}(I_1 - 3) + \frac{1}{20N}(I_1^2 - 9) + \frac{1}{1050N^2}(I_1^3 - 27) \\ + \frac{19}{7000N^3}(I_1^4 - 81) + \frac{519}{673750N^4}(I_1^5 - 243) + \ldots\end{array}\right] \tag{2.26}$$

Treloar's polynomial expansion for the inverse Langevin function loses accuracy as $\lambda \to 1$. An arbitrary number of terms can be used to converge to an appropriate solution, but will never estimate the value at $\lambda = 1$ exactly. Similarly, regression can be used to more accurately fit the Langevin function with the same order polynomial [48], but again is incapable of estimating the infinite value for β as $\lambda \to 1$, and loses physical significance. A better method is to use the Pade approximation presented by Cohen [49] and shown as

$$\mathcal{L}^{-1}(\lambda) = \lambda\frac{3 - \lambda^2}{1 - \lambda^2} \tag{2.27}$$

This approximation overestimates the Langevin function, but by no more than 5%, and approaches its exact value for both $\lambda \to 0$ and $\lambda \to 1$. The comparison is plotted for $\beta = \mathcal{L}^{-1}(\lambda)$ in Figure 2-6, and is more accurate than both the linear Gaussian statistics approximation and the Taylor series approximation to four terms in Equation (2.25). Equation (2.24) can be rewritten using the Pade approximation as

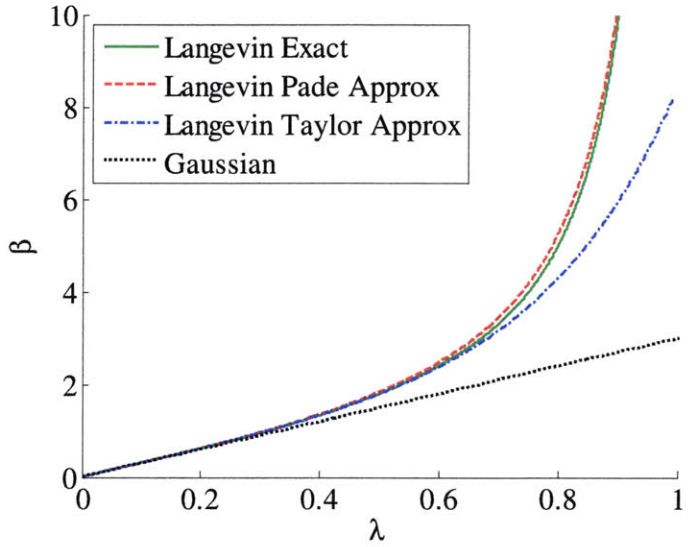

(a)

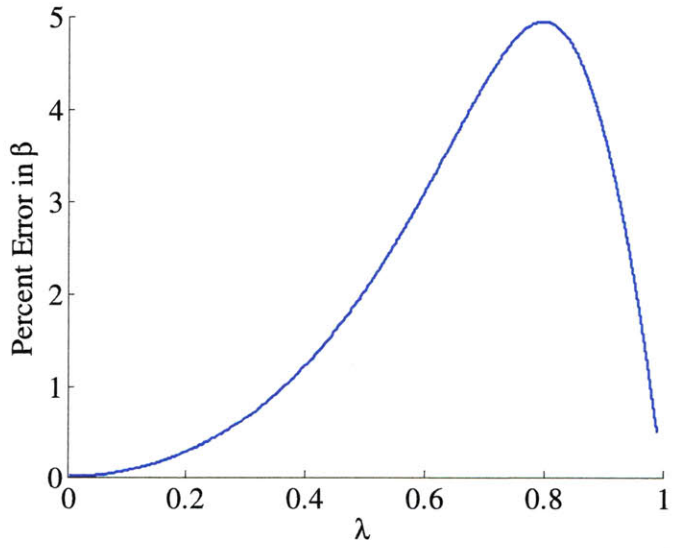

(b)

Figure 2-6: (a) The Pade approximation correctly captures the behavior of the inverse Langevin function as λ approaches 1, and is superior to both the linear Gaussian statistics approximation and the Taylor series approximation to four terms. (b) The error of the Pade approximation is bounded to less than 5%.

$$\sigma_1 - \sigma_2 = \frac{nkT\sqrt{N}}{3}\left(\frac{\lambda_{chain}}{\sqrt{N}}\right)\frac{3-\left(\frac{\lambda_{chain}}{\sqrt{N}}\right)^2}{1-\left(\frac{\lambda_{chain}}{\sqrt{N}}\right)^2}\left(\frac{\lambda_1^2-\lambda_2^2}{\lambda_{chain}}\right) \tag{2.28}$$

Again, incompressibility and uniaxial tension are assumed to solve for uniaxial stress.

$$\sigma_1 - \sigma_2\big|_{\sigma_2=\sigma_3=0,\lambda_1\lambda_2\lambda_3=1} = \frac{nkT}{3}\frac{3N-(\lambda_{chain})^2}{N-(\lambda_{chain})^2}\left(\lambda_1^2-\frac{1}{\lambda_1}\right) \tag{2.29}$$

It is helpful to simplify this expression with the first invariant I_1.

$$\sigma_1 = \frac{nkT}{3}\frac{9N-I_1}{3N-I_1}\left(\lambda_1^2-\frac{1}{\lambda_1}\right) \tag{2.30}$$

Young's modulus is derived by differentiating stress for uniaxial tension.

$$E = \frac{d\sigma_1}{d\lambda_1} = \frac{nkT}{3}\left(\frac{9N-I_1}{3N-I_1}\left(2\lambda_1+\frac{1}{\lambda_1^2}\right)+\frac{12N\lambda_1}{(3N-I_1)^2}\left(\lambda_1^2-\frac{1}{\lambda_1}\right)\right) \tag{2.31}$$

Initial modulus evaluated at the unstretched state gives

$$E_0 = \left.\frac{d\sigma_1}{d\lambda_1}\right|_{\lambda_1=1} = nkT\left(\frac{3N-1}{N-1}\right) \tag{2.32}$$

In the limit as $N \to \infty$, $E_0 \to 3nk\Theta$ and is equivalent to initial modulus computed with Gaussian statistics in Equation (2.18).

For the remainder of this thesis, the expression for initial modulus E_0 will be used to compare experimental results. However, for completeness, strain energy is included for the eight chain network by integrating Equation (2.28) into Equation (2.33). As N approaches infinity, the eight chain model approaches the Gaussian statistics result. Equation (2.33) is preferable to Equation (2.26), since it requires fewer terms for small values of N.

$$W = \frac{nkT}{6}\left[(I_1 - 3) + 2\ln\left(1 + \frac{I_1 - 3}{3N - I_1}\right)^{3N}\right] \tag{2.33}$$

Shown in Figure 2-7 is a comparison of strain energy calculated for a uniaxial stretch of $\lambda_1 = 1.1$ using the Gaussian network approximation in Equation (2.12), the Taylor series expansion of the Arruda-Boyce model to five terms in Equation (2.26), and the new Pade approximation of the eight chain model in Equation (2.33). For small values of N close to one, the Pade approximation more accurately depicts the extensibility limit of Langevin statistics, and should be preferentially used for materials with small N. To determine the value of N, Equation (2.31) can be fitted with uniaxial tension or compression experiments, such as those in [50]. Table 2.1 shows strain energy and initial modulus expressions for a Gaussian network, and eight chain networks using Taylor series or Pade approximations.

2.4 Fully Cured Modulus of PDMS

2.4.1 The effect of mixing ratio on modulus in a Gaussian network

Combining Equation (2.10) with Equation (2.18), initial Young's modulus is found to be directly proportional to the fully cured crosslink density n_{max}, for any arbitrary cure extent p.

$$E_0 = 3\left(p - p_{gel}\right)n_{max}kT \tag{2.34}$$

The fully cured modulus is then directly

$$E_{0,cured} = 3\left(1 - p_{gel}\right)n_{max}kT \tag{2.35}$$

It follows that E_0 is the maximum when $n_{max} = n_{stoich}$, and the mixing ratio is stoichiometrically matched. If this maximum modulus is defined as E_{stoich}, the ratio of E_0 to E_{stoich} is n_r,

$$\frac{E_{0,cured}}{E_{stoich}} = \frac{n_{max}}{n_{stoich}} \equiv n_r \tag{2.36}$$

and directly given by Equations (2.5) and (2.6) for base and curing agent limiting conditions. The

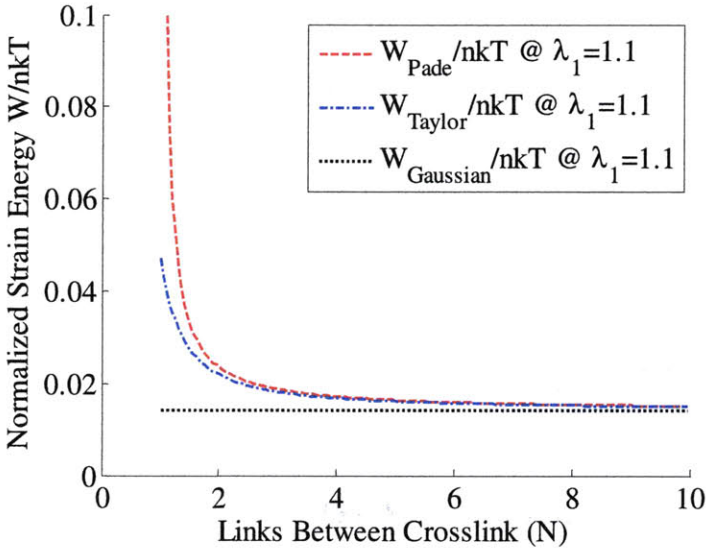

Figure 2-7: An improved strain energy estimate using the Pade approximation captures the asymptotic increase in strain energy as the number of links per chain approaches 1.

Table 2.1: Comparison of strain energy and initial modulus.

Quantity	Gaussian	Eight chain network (Taylor)	Eight chain network (Pade)
Strain energy W	$\frac{nkT(I_1-3)}{2}$	$nkT\left[\frac{I_1-3}{2}+\frac{I_1^2-9}{20N}+\ldots\right]$	$\frac{nkT}{6}\left[(I_1-3)+2\ln\left(1+\frac{I_1-3}{3N-I_1}\right)^{3N}\right]$
Initial Young's modulus E_0	$3nkT$	$3nkT\left(1+\frac{40425}{67375N}+\ldots\right)$	$nkT\left(\frac{3N-1}{N-1}\right)$

ratio n_r is a function of the user controlled input R_{mix}, and the material parameter R_{stoich}.

2.4.2 The effect of mixing ratio on modulus in an eight chain network

Combining Equation (2.10) with Equation (2.32), initial Young's modulus is now a function of an additional parameter N.

$$E_0 = \left(p - p_{gel}\right) n_{max} kT \left(\frac{3N-1}{N-1}\right) \tag{2.37}$$

Similarly, the fully cured modulus is

$$E_{0,cured} = \left(1 - p_{gel}\right) n_{max} kT \left(\frac{3N_f - 1}{N_f - 1}\right) \tag{2.38}$$

where N_f denotes the links per chain in the fully cured polymer. Since the volume is unchanged for different mixing ratios, the total number of links $n_{max}N_f$ is conserved:

$$n_{max} N_f = n_{stoich} N_{stoich} \tag{2.39}$$

or equivalently,

$$N_f = \frac{N_{stoich}}{n_r} \tag{2.40}$$

where is n_r is given by Equation (2.36). It follows that the normalized modulus is given by

$$\frac{E_{0,cured}}{E_{stoich}} = n_r \left(\frac{3N_{stoich} - n_r}{N_{stoich} - n_r}\right)\left(\frac{N_{stoich} - 1}{3N_{stoich} - 1}\right) \tag{2.41}$$

Compared with the Gaussian network, the eight chain network contains the additional physics based parameter N_{stoich}, which describes the links per chain at the stoichiometric mixing ratio.

2.5 Time Evolution of Modulus During Cure

2.5.1 The effect of cure extent on modulus in a Gaussian network

The time evolution of modulus in a Gaussian network can be normalized and expressed by

$$\frac{E_0}{E_{0,cured}} = \frac{p - p_{gel}}{1 - p_{gel}} = p_r \tag{2.42}$$

where p_r is given by Equation (2.11) and changes over time.

2.5.2 The effect of cure extent on modulus in an eight chain network

As with changes to the mixing ratio, the total volume is unchanged during cure, so the total number of links nN is conserved

$$nN = \left(n_{max} - n_{gel}\right) N_f \tag{2.43}$$

If the mixing and stoichiometric ratios are known, N_f can be determined using Equation (2.39). From Equations (2.10) and (2.11), Equation (2.43) can be rewritten as

$$N = p_r N_f \tag{2.44}$$

Consequently, the normalized modulus in an eight chain network is given by

$$\frac{E_0}{E_{0,cured}} = p_r \left(\frac{3N_f - p_r}{N_f - p_r} \right) \left(\frac{N_f - 1}{3N_f - 1} \right) \tag{2.45}$$

This is analogous to Equation (2.41), except n_r and N_{stoich} terms are replaced with p_r and N_f terms. Equation (2.45) is plotted in Figure 2-8 for N_f values of 2 and infinity. It follows that as N_f approaches infinity, Equation (2.45) approaches Equation (2.42). When p_r is modeled by Equations (2.8) and (2.11) using the calibration constants from Table 4. for 10:1 mixing ratio of PDMS, the time evolution of modulus can be modeled and shown in Figure 2-9 for the case where the cure takes place at room temperature.

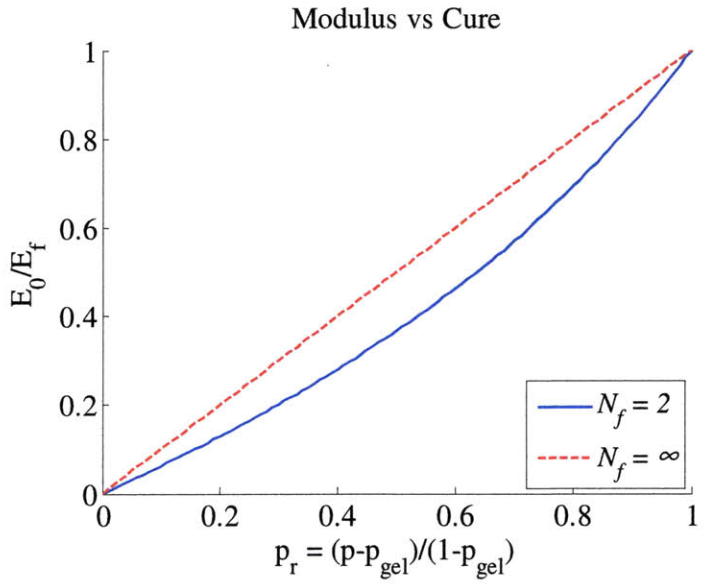

Figure 2-8: Simulated non-dimensional modulus versus cure.

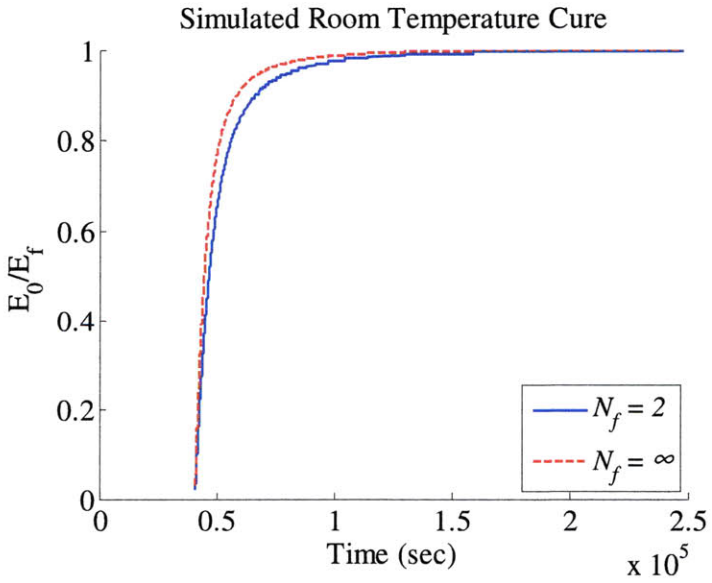

Figure 2-9: Simulated non-dimensional modulus versus time at room temperature.

2.6 Summary

Statistical mechanics is applied to describe the fully cured modulus by the mixing ratio, and the time evolution of cure by the time evolution of modulus. These formulations for modulus enable mechanical testing techniques to be used to detect the cure extent of a cure process. In this chapter is also presented an improved approximation for the strain energy of the Arruda-Boyce eight chain rubber model. This form can be simpler and more accurate for low N materials and high stretch deformations, compared to the series expansion given by Arruda.

Nomenclature

E, E_0 = Young's modulus, small strain initial Young's modulus [N/m^2]

$E_{0,cured}$ = fully cured modulus [N/m^2]

E_{stoich} = fully cured modulus at the stoichiometric mixing ratio R_{stoich} [N/m^2]

f_{avg} = average functionality

I_1 = first invariant of the left Cauchy Green Tensor

k = Boltzmann's constant [J/K]

l = length per link [m]

n = chain density, or incremental crosslink density after gelation [m^{-3}]

n_b, n_c = crosslink density of base and curing agent [m^{-3}]

n_p = crosslink density at a cure extent of p [m^{-3}]

n_r = n_{max} normalized by n_{stoich}

n_{max}, n_{stoich} = fully cured crosslink density at a mixing ratio of R_{mix} and R_{stoich} [m^{-3}]

n_{gel} = crosslink density at gelation [m^{-3}]

N = number of links per chain

N_{stoich} = number of links per chain at a mixing ratio of R_{stoich}

N_f = number of links per chain when fully cured

p, p_{gel} = cure extent, cure extent at gelation

r_{chain} = chain length [m]

R_{mix}, R_{stoich} = mixing and stoichiometric ratio of base to curing agent

T = temperature [K]

V_b, V_c, V = volume of base, curing agent, and the combined mixture [m^3]

W = strain energy [J/m^3]

β = non-dimensional force required to stretch a chain to r_{chain}

λ = stretch

$\lambda_1, \lambda_2, \lambda_3$ = stretches in the principal directions

λ_{chain} = total stretch from all three spatial stretches

λ_L = locking stretch

$\mathcal{L}(\beta)$ = Langevin function

CHAPTER

3

EXPERIMENTAL VALIDATION OF THE MODULUS MODELS

In Chapter 2, models for fully cured modulus and time evolution of modulus were developed. In this chapter, these models are validated by tension and compression tests previously published in literature, as well as durometer and micro-indentation tests.

3.1 Fully Cured Modulus

In Chapter 2, Gaussian and Langevin statistics were used to produce two models for fully cured modulus. The first model, based on a Gaussian network model, neglected locking behavior in materials with many links per chain N. The latter model, based on the Arruda-Boyce eight chain network, used Langevin statistics with a Pade approximant and could more accurately predict materials with small N.

To determine which model is applicable for PDMS, two datasets are examined. First, data is taken from tensile tests performed by Huang and Anand in unpublished work [35], and second, durometer indentation tests. Tension tests performed by Huang are reproduced in Figure 3-1 for various base to curing agent mixing ratios. Initial modulus can be extracted as the small strain slope of the stress-stretch curve, and are tabulated in Table 3.1.

Tension tests are ideal for extracting Young's Modulus in an unknown material, but durometer indentation tests can be more convenient since they can be performed on tests specimens of all shapes and sizes. A Longacre durometer, shown in Figure 3-2, is used for these experiments. Its large indentation area is capable of smoothing out local inhomogeneities that are smaller than the tip area.

In the durometer experiments, 2.7 mm samples of PDMS were prepared with a base to

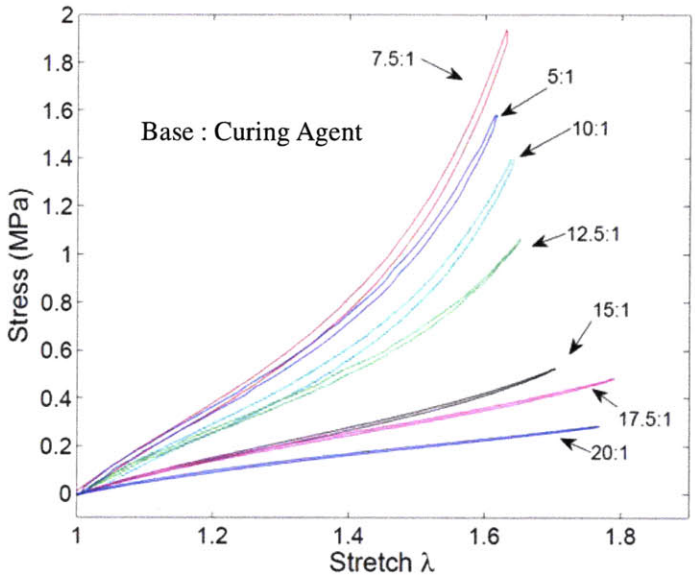

Figure 3-1: Tension tests performed by Huang and Anand [35] **for various mixing ratios (base:curing agent).**

Table 3.1: Initial modulus extracted from Huang tension tests.

Mixing Ratio R_{mix}	E_0 (MPa)
5:1	1.8
7.5:1	1.9
10:1	1.5
12.5:1	1.3
15:1	0.75
17.5:1	0.75
20:1	0.5

Figure 3-2: Longacre durometer for testing Shore A tire hardness.

Table 3.2: Initial modulus from durometer experiments.

Mixing Ratio R_{mix}	E_0 *Avg.* (MPa)	E_0 *Std Dev* (MPa)
5:1	6.35	0.52
7.5:1	7.65	0.30
10:1	6.55	0.64
12.5:1	4.97	0.54
15:1	4.10	0.30
20:1	3.22	0.11

curing agent ratio of 5:1, 7.5:1, 10:1, 12.5:1, 15:1, and 20:1. Six samples at each mixing ratio were cured at 150C for 30 minutes, and subsequently measured with the durometer. Gent theory [51], shown in Equation (3.1), was used to convert the Shore A hardness reading (S_A) to initial modulus.

$$E_0 = \frac{15.75 + 2.15(S_A)}{100 - S_A} \tag{3.1}$$

The mean and standard deviation of these results are tabulated in Table 3.2. These values are higher than those found using tension tests. The main reason is that elastomers such as PDMS are nonlinear elastic material. In fact, the modulus increases at higher strains. Consequently, during durometer indentation, part of the polymer undergoes large compressive strain, and exhibits a stiffness value that is larger than you would expect from the initial modulus.

Using a least squares minimization technique, n_{stoich} and R_{stoich} can be adjusted to fit Equation (2.36) to both tension and durometer data in Figure 3-3. Similarly, n_{stoich}, N_{stoich}, and R_{stoich} can be adjusted to fit Equation (2.41) to the same data sets in Figure 3-4. A Gaussian network model for modulus in Figure 3-3 appears to capture the correct trends in the data, but an eight chain network model indeed provides a better fit. This is not surprising, since N_{stoich} is found to have similar values of 1.9 and 2.1 in tension and durometer experiments, and indicates that Langevin statistics should be used with PDMS.

Another point of interest is that the stoichiometric mixing ratio is found to be 7.2:1 and 8.4:1 in Figure 3-3, and 8.5:1 and 9.2:1 in Figure 3-4. Dow Corning recommends Sylgard 184 to be mixed at a base to curing agent ratio of 10:1, which is much closer to the values determined in Figure 3-4. Compared with Gaussian statistics, Langevin statistics more accurately capture the faster drop-off in stiffness as the mixing ratio moves away from the stoichiometric ratio, and produces the sharper peak seen in Figure 3-4.

In Langevin statistics, the locking stretch is the stretch value when a polymer chain is fully extended; hence, its value is given by Equation (3.2).

$$\lambda_L = \sqrt{N} \tag{3.2}$$

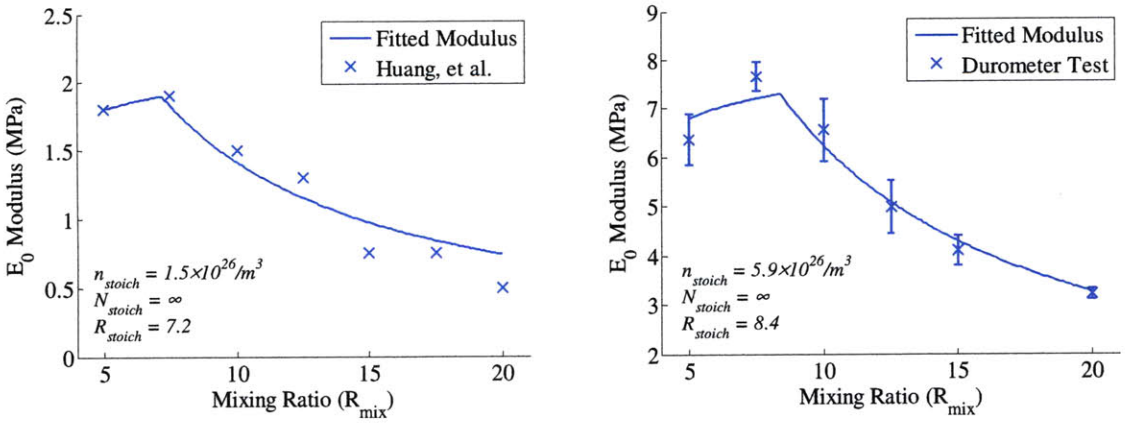

Figure 3-3: Gaussian network model for tension (left) and indentation (right).

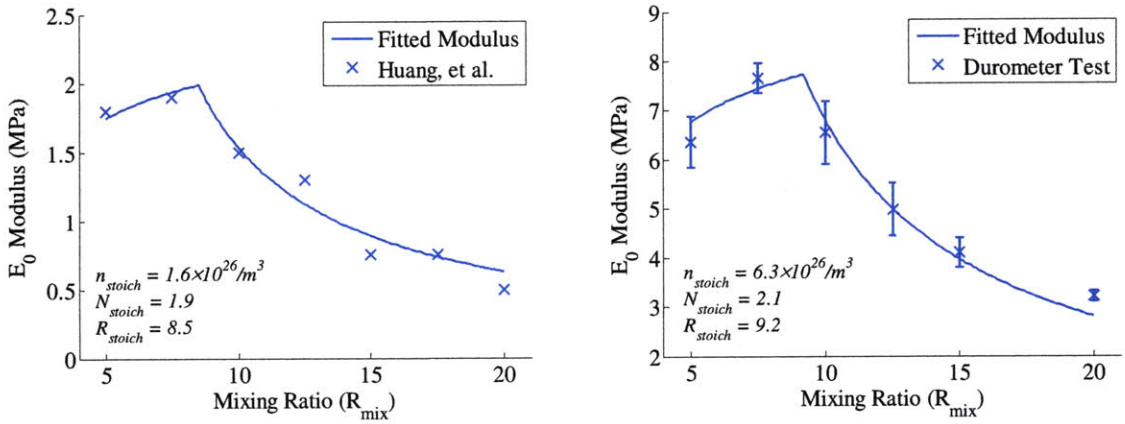

Figure 3-4: Eight chain network model for tension (left) and indentation (right).

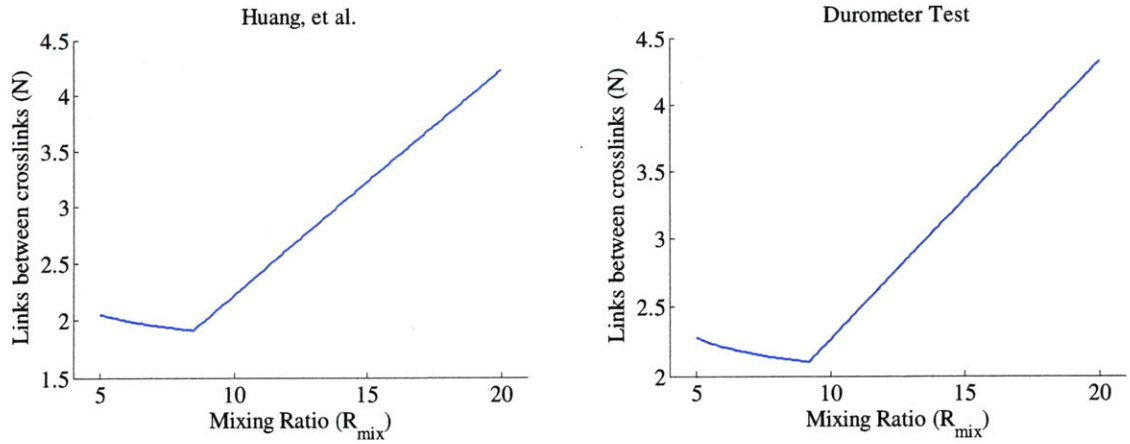

Figure 3-5: Links between crosslinks (*N*) model for tension (left) and indentation (right).

Tension and compression tests can also be used to determine the network locking stretch. In tension and compression tests performed by Huang [50] in Figure 3-6, this value is found to be λ_L=*1.24* and *1.44* for a 5:1 ratio, and λ_L=*2.06* and *2.38* for a 20:1 ratio. Equivalently λ_L and N are related such that N=*1.54* and *2.07* for 5:1, and N=*4.24* and *5.66* for 20:1.

Using Equation (2.40), values of N can be plotted for different mixing ratios as shown in Figure 3-6. At ratios of 5:1 and 20:1, data from the tension tests produces values of N=*2.05* and *4.22*, and data from the durometer tests produces values of N=*2.27* and *4.34*. These are shown in Table 3.3, both of which are similar with Huang's observations when fitting macro-scale tension and compression curves at these ratios.

3.2 Time Evolution of Modulus: Heated Micro-indentation

3.2.1 Apparatus

To validate the model for the time evolution of modulus, a heated micro-indentation setup was developed. Several mechanical options exist for measuring modulus and are summarized in Table 3.4. A durometer can be used to capture modulus, but its deep indentation depth in soft substrates restricts the thickness of parts that can be measured. Rheometry is a common technique used to characterize viscous liquids, but requires a large test volume and is impractical to remove after gelation. Ultrasound provides a noncontact technique to characterize solid samples, but requires them to be freestanding; consequently, cast PDMS parts cannot be measured unless they are solid enough to demold. Atomic force microscopy (AFM) offers an interesting option since its small tip leaves the sample mostly undisturbed, but heating systems do not exist to allow measurement during heated cure. Micro-indentation offers similar benefits, but because research quality equipment is available to modify, a heated stage can be integrated and custom probing recipes can be programmed into the device.

In micro-indentation, the load-displacement relationship is dependent on the indenter tip geometry and the substrate material. For axis-symmetric tip geometries, Sneddon [52] describes indentation into an linear elastic material by Equation (3.3):

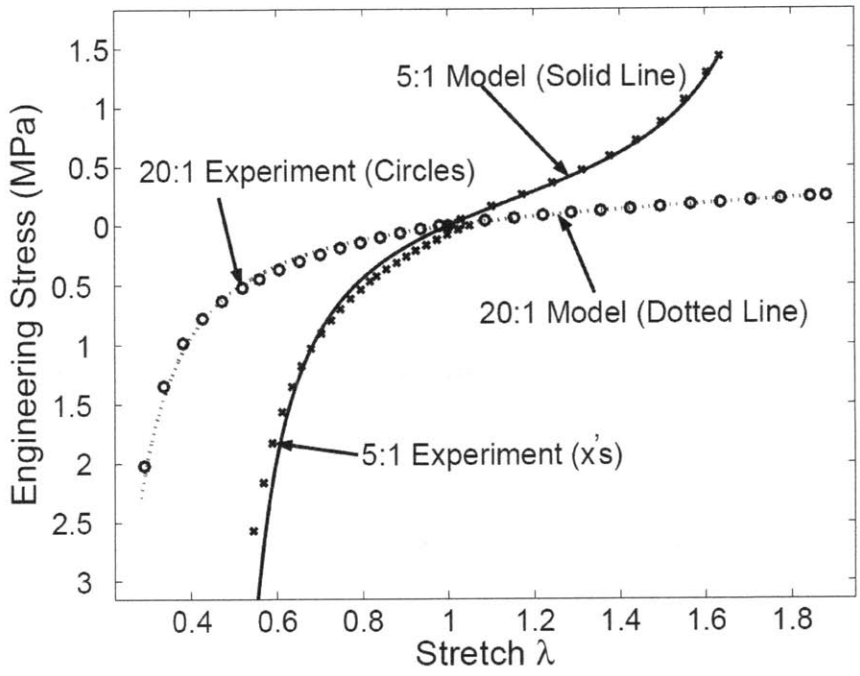

Figure 3-6: Tension and compression experiments from Huang [50].

Table 3.3: Links between crosslinks (*N*) from tension and compression experiments [50]**, and the crosslink model are similar.**

Test method	N (R_{mix} = 5:1)	N (R_{mix} = 20:1)
Huang tension	1.54	4.24
Huang compression	2.07	5.66
Crosslink model: Huang E_0	2.05	4.22
Crosslink model: Durometer E_0	2.27	4.34

Table 3.4: Measurement strategies for modulus.

Strategy	Sensitivity	Capability	Flexibility
Durometer	mm	Thick samples	Manual data collection
Rheometry	mm	Thick samples	Large volumes
Ultrasound	mm	Solid samples	Freestanding samples
AFM	nm	No heating	No heating
Micro-indentation	μm to nm	Thin samples	Custom stage

Table 3.5: Load/displacement relationship for various tip geometries.

Indenter geometry	Load	Contact radius *r(h)* or area *A(h)*
Cylinder, radius b	$P = 2\frac{E}{1-\nu^2}bh$	$r(h) = b$
Sphere, radius R	$P = \frac{4}{3}\frac{E}{1-\nu^2}\sqrt{R}h^{\frac{3}{2}}$	$r(h) = \sqrt{Rh}$
Cone, semi-included angle θ	$P = \frac{2}{\pi}\frac{E}{1-\nu^2}\tan\theta h^2$	$r(h) = \frac{2}{\pi}h\tan\theta$
Vickers pyramid	$P = 1.845\frac{E}{1-\nu^2}h^2$	$A(h) = 9.673h^2$
Berkovich pyramid	$P = 1.932\frac{E}{1-\nu^2}h^2$	$A(h) = 8.958h^2$

$$P(h) = \frac{2E}{1-\nu^2} \int_0^{r(h)} \frac{x^2 \cdot z'(x)}{\sqrt{r(h)^2 - x^2}} dx \tag{3.3}$$

with E as Young's modulus, v as Poisson's ratio, $r(h)$ as the radius of the contact surface, $z(x)$ as the axis-symmetric depth of the tip, and $z'(x)$ as its derivative with respect to x.

The result for several common tip profiles is calculated by Briscoe [53] and reproduced in Table 3.5. For any tip geometry, the load P is directly proportional to modulus E at any arbitrary depth. For a rubbery material, if the stresses are small, E is approximately E_0. To minimize the possibility of tear and high stress concentrations, a spherical tip profile is used. Under displacement control, E_0 is a function of time and h is constant, so Briscoe's expression for a spherical tip can be rewritten as Equation (3.4) and drawn schematically in Figure 3-7.

$$P(t) = \frac{4}{3} \frac{E_0(t)}{1-\nu^2} \sqrt{R} h^{\frac{3}{2}} \tag{3.4}$$

The material remains nearly incompressible during cure, so $1-\nu^2$ changes insignificantly and is independent of time. At any arbitrary time, the force measurement $P(t)$ at depth h is directly proportional to initial modulus $E_0(t)$.

Ideally, the loading and unloading curves of a perfectly linear elastic solid traverse the same path. In this case, Equations (3.3) and (3.4) are capable of returning a perfect estimate for elastic modulus. In reality, the loading and unloading curves of micro-indentation often follow different paths during curing. There are some viscoelastic and surface effects that cause this to occur. However, the Oliver-Pharr method [54] can be used to extract the modulus from the initial portion of the unloading curve. The slope is given by Equation (3.5) for a spherical tip geometry, and shown schematically in Figure 3-8.

$$S(t) = \frac{dP(t)}{dh} = \frac{2\sqrt{Rh}}{1-\nu^2} E_0(t) \tag{3.5}$$

By using $S(t)$ instead of $P(t)$ to calculate $E_0(t)$, the Oliver-Pharr method is less sensitive to errors in depth measurements h.

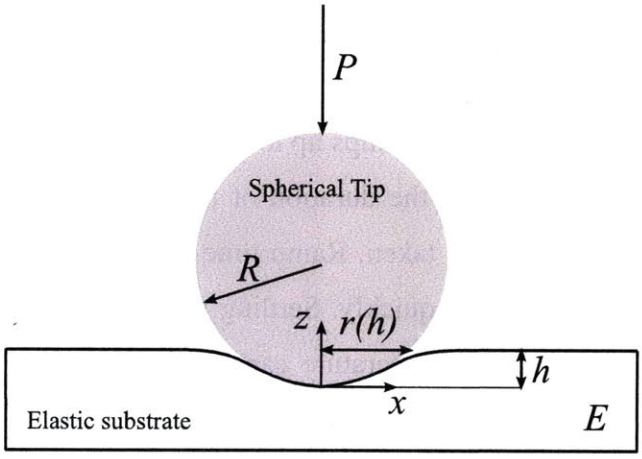

Figure 3-7: A spherical tip indenting a perfectly elastic material.

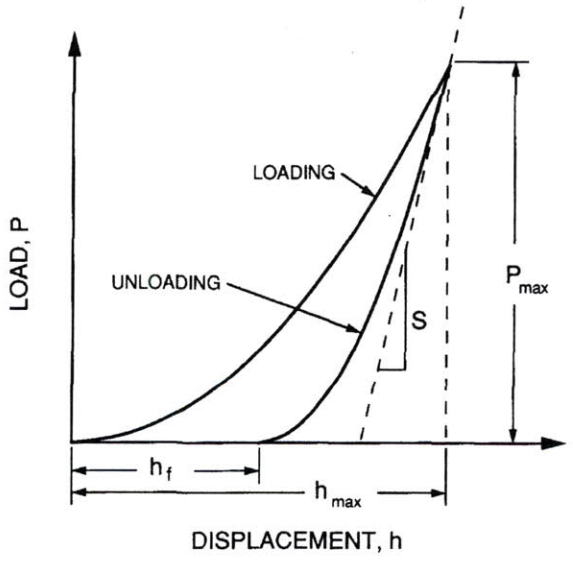

Figure 3-8: Modulus extraction using the Oliver-Pharr method [54].

The setup used for micro-indentation is a flexure based design created by Gearing [48] and shown in Figure 3-9. The small voice coil actuator and soft flexural bearings are ideal for indentation of soft materials, since the stiffness of the flexure and stiffness of the test material are added together in series.

A heated stage, which can be used to hold a liquid PDMS pre-polymer sample, was implemented to add capability for micro-indentation to capture stiffness changes during cure. The ideal heated micro-indentation stage ramps up to a setpoint temperature instantaneously, and maintains that temperature throughout the duration of the cure. To make a stage that behaves nearly ideally, the following steps are taken. Ramp time is reduced by designing a high output heater to supply the system with heat quickly. Settling time is reduced by designing high heat dissipation so that any overshoot in temperature can be quickly reduced. Finally, temperature control is maintained by a proportional controller programmed in LabView.

The final design is shown in Figure 3-10. Two 50W resistive heaters are used to rapidly supply heat into the system. The resistive heaters also have scalloping on the sides to help remove heat from the system. They are mounted on an aluminum backplate to distribute the heat uniformly beneath the PDMS sample. An acrylic piece is then cut to form the walls of the PDMS mold, and attach to the legs of the setup. Attaching legs to the acrylic allows any expansion of the aluminum backplate and heaters to occur away from the indenter tip, restricting vertical shifts to only the PDMS test part. Finally, a bare 30 AWG K-type thermocouple (Omega P/N 5SRTC-GG-K-30-36) is placed beneath the aluminum backplate to sense hotplate temperature and feedback to the control system.

The control system is managed by a custom LabView program. The control program calculates the amount of heat necessary to bring the system up to the process temperature, and turns the heaters fully on until this energy has been dissipated by the resistors. The system subsequently switches to proportional control to maintain the system near the process temperature.

3.2.2 Micro-indentation of fully cured PDMS at various mixing ratios

As the mixing ratio of base to curing agent is varied, the modulus can be extracted by either Equation (3.4) or (3.5). If the samples are perfectly linear elastic and the indentation depth is known accurately, both methods should yield the same results. Several micro-indentation

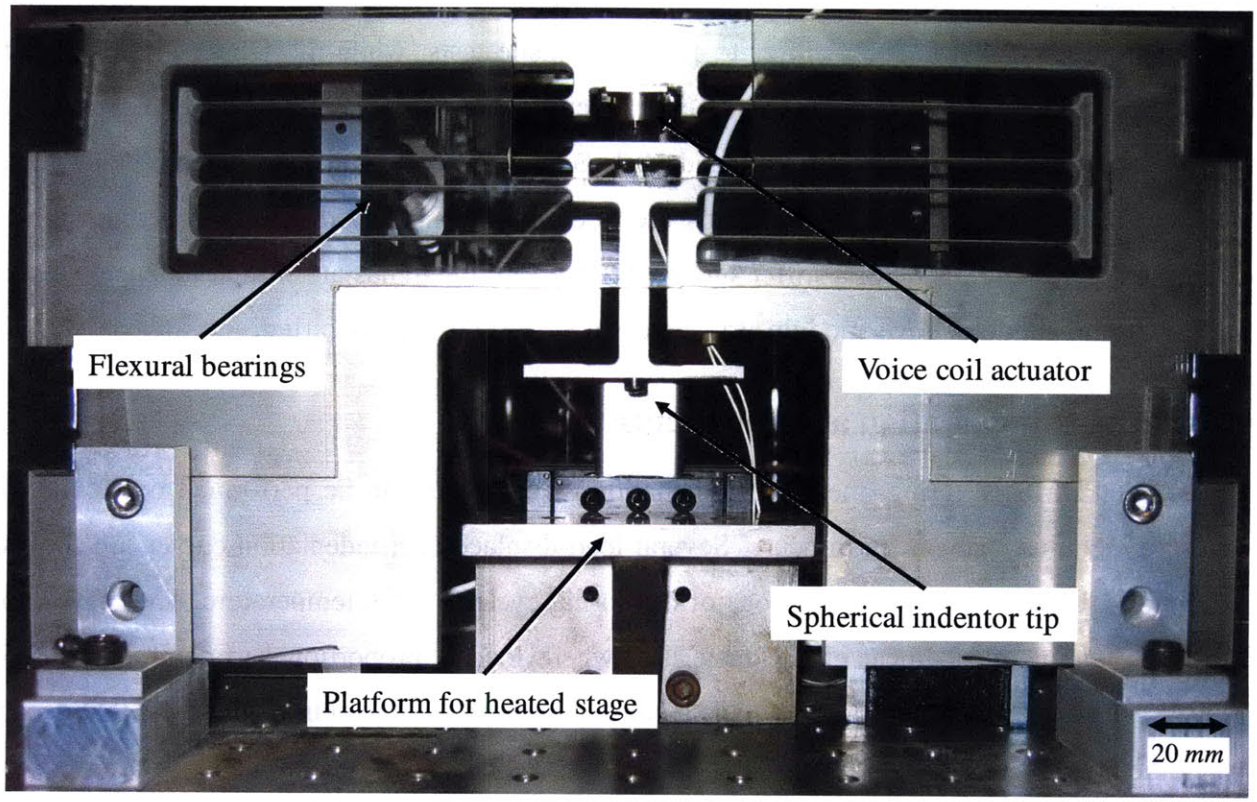

Figure 3-9: Flexure based micro-indentation.

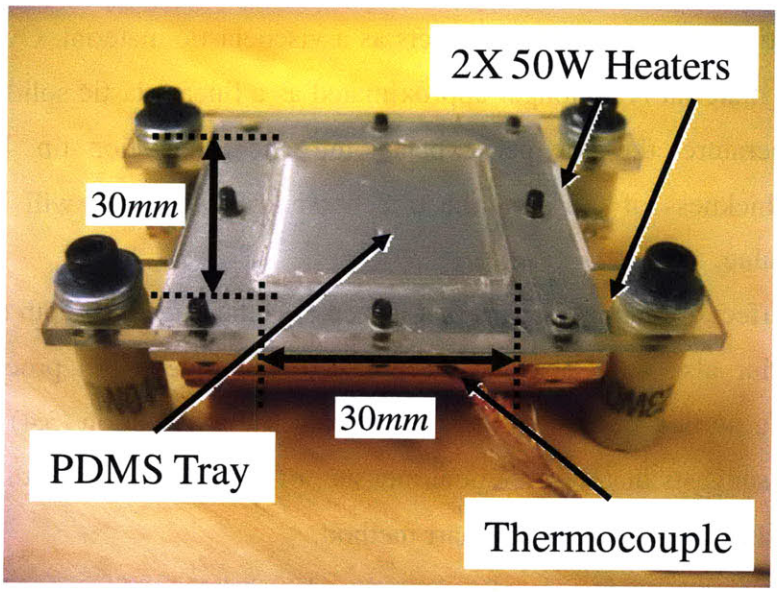

Figure 3-10: Heated stage for micro-indentation.

loading/unloading curves are shown in Figure 3-11, and their modulus values tabulated in Table 3.6 show the same trend as tension and durometer experiments, except for a scale factor. The load method provides modulus closer to Huang's tensile tests, while the Oliver-Pharr method gives larger values closer to the durometer experiments. As before, the largest modulus predicted occurs for a mixing ratio between 7.5:1 and 10:1. Both micro-indentation results are larger than the tension tests, since indentation strains are not infinitesimal. Modulus increases at higher strains and gives an illusion of a stiffer substrate. However, the trends are similar to tension tests, and micro-indentation allows modulus to be measured while PDMS is curing.

3.2.3 Micro-indentation at various cure extents

As PDMS is curing, the same indentation experiments can be performed over time to measure modulus changes during cure. Several load-displacement indentation curves are shown in Figure 3-12, during different portions of the curing cycle at room temperature. The curves no longer behave as ideal linear elastic materials, where load is proportional to depth to the 1.5 power, as given by Equation (3.4). This is a consequence of several additional effects that occur when the polymer is not fully cured. First, as a liquid, a meniscus forms on the indentation tip as shown by Figure 3-13. This effectively increases the indentation depth. Furthermore, as the polymer cures, this meniscus clasps onto the indentation tip with additional adhesion. Second, as the polymer transitions through gelation, it acts as a viscoelastic material. Over the entire depth of indentation, the material is no longer approximated as a linear elastic solid. Finally, for cures above room temperature, the polymer expands into the indentation tip. Depending on the temperature and thickness of the part, the true depth of indentation will be larger than the original nominal value.

The main effect of the meniscus is that it increases the effective depth of indentation. The viscoelastic behavior also adds non-elastic energy to the indentation process, and therefore changes the loading portion of the indentation curve such that Equation (3.4) is no longer valid. Both these effects suggests that a differential measure of force during unloading should be used, which is accomplished using the Oliver-Pharr method.

The other major consequence of indentation during cure is the uncertainty and shifts in depth during cure. For isothermal cures, the system reaches thermal equilibrium and the meniscus and expansion changes to depth are constant. From Equation (3.5), this only causes an

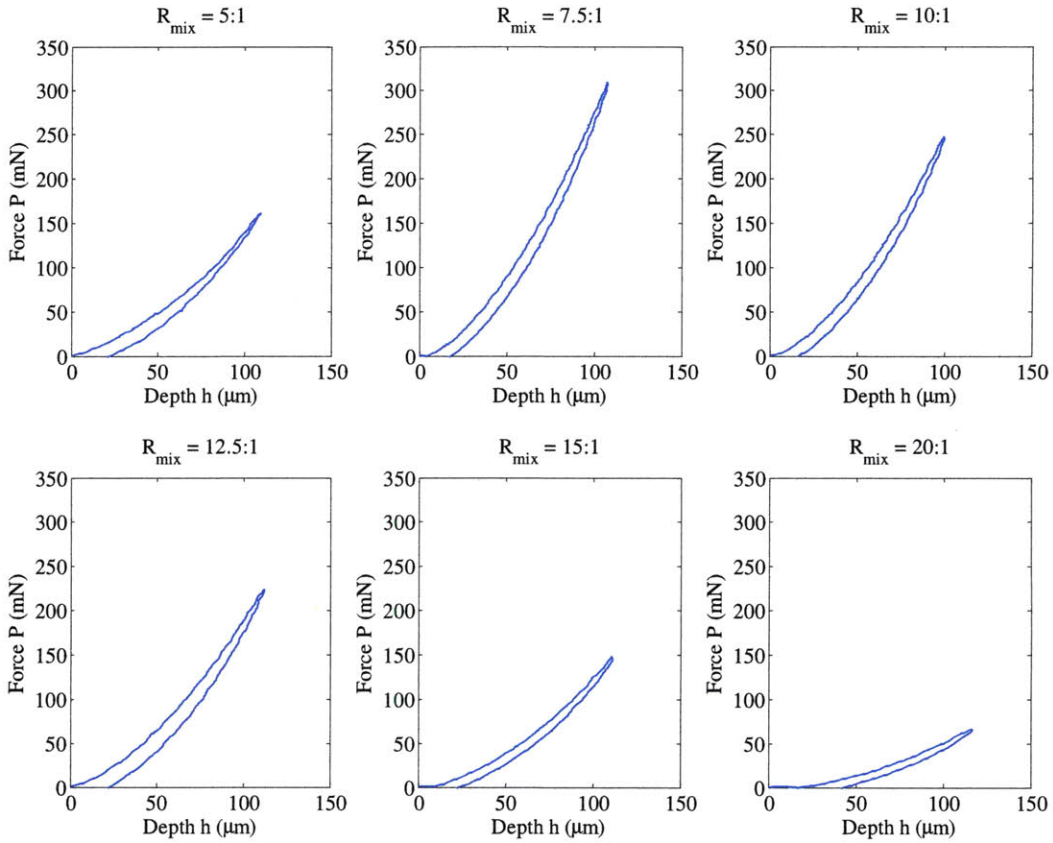

Figure 3-11: Typical micro-indentation curves with a 1/8" diameter spherical tip at different mixing ratios show capability to discern modulus changes.

Table 3.6: Initial modulus estimate E_0 (MPa) using various test methods.

Mixing Ratio R_{mix}	Tension test (Huang)	Durometer test (Gent theory)	Micro-indentation (load method)	Micro-indentation (Oliver-Pharr)
5:1	1.8	6.4	2.0	3.1
7.5:1	1.9	7.7	3.9	7.2
10:1	1.5	6.5	3.5	7.2
12.5:1	1.3	5.0	2.7	4.7
15:1	0.75	4.1	1.8	2.7
20:1	0.5	3.2	0.7	1.3

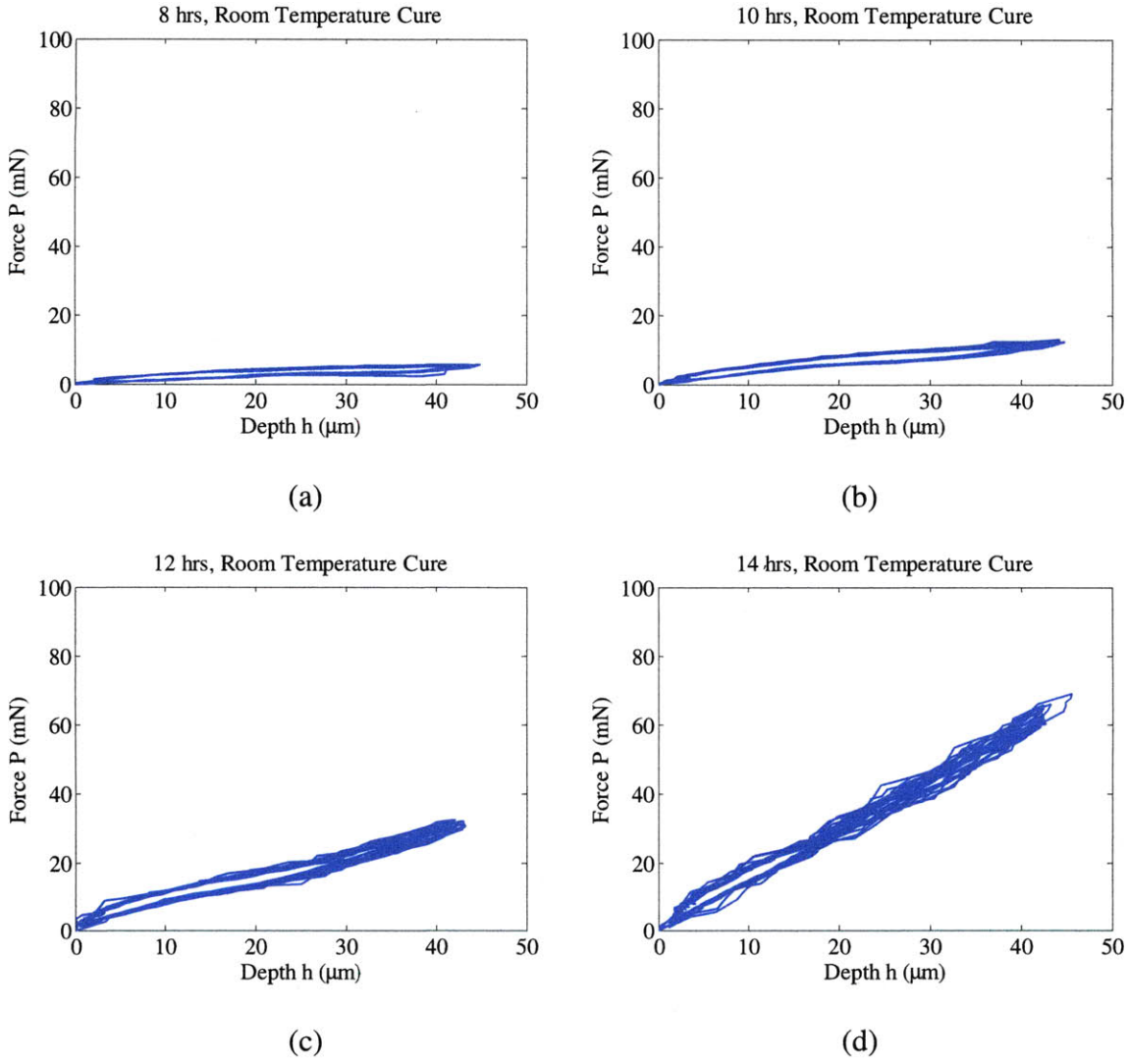

Figure 3-12: Micro-indentation load-displacement curves for PDMS cure at room temperature after curing for (a) 8 hrs, (b) 10 hrs, (c) 12 hrs, and (d) 14 hrs.

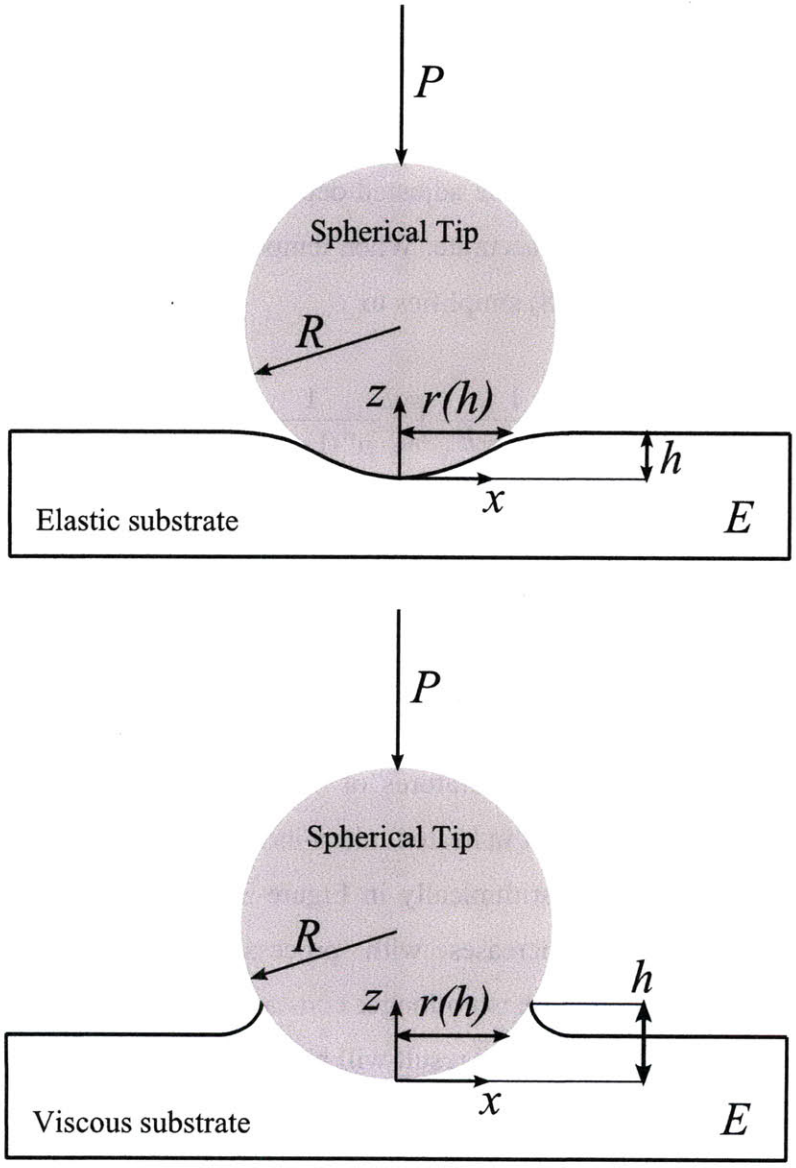

Figure 3-13: Indentation into a perfectly elastic solid (top) and a viscous liquid (bottom). The formation of a meniscus increases the effective depth of indentation.

error in the scale factor of modulus. The relative relationship of modulus over time is still accurate, when normalized to its final fully cured modulus. For non-isothermal cures, the time dependent change in depth will affect the measured modulus over time. However, the gel point is independent of the magnitude of modulus, and can still be easily observed.

3.2.4 Gelation identification and calibration of initial cure extent

At the gel point, the polymer begins to show a finite modulus, which sharply increases over time. At room temperature, since the adjusted depth is constant throughout the duration of the cure, the trend of the modulus is accurate. When temperature T is constant, as in the case of room temperature cure, Equation (2.8) simplifies to

$$t_{gel} = \frac{1}{k_0 \exp(\frac{-E}{RT})} \int_{p_0}^{p_{gel}} \frac{1}{p^m (1-p)^n} dp \tag{3.6}$$

where t_{gel} is the time to reach gelation. From the room temperature plot in Figure 3-14 and the reaction rate constants from Table 4. for 10:1 mixing ratio, the initial cure extent p_o is determined to be 0.02%. Using Equations (2.8) and (2.45), if polymer temperature is assumed to be constant, modulus can be modeled as a function of time for N_f = 2. The model fits well at room temperature, but at higher process temperatures of 45C, 65C, and 85C, the model begins to underestimate gel time. This is evident in heated micro-indentation experiments plotted in Figure 3-15. The time scale is plotted logarithmically in Figure 3-15, and shows that the percentage underestimation of the model increases with process temperature. At higher process temperatures, the polymer temperature is no longer constant, and the reaction occurs at a slower rate than predicted by Equation (3.6). This result will be discussed in more detail in Chapter 4.

3.3 Summary

Langevin statistics are found to be more applicable for the modeling of Sylgard 184 PDMS, since its links per chain N is small. The links per chain N is found to be approximately 2 for both tension tests from literature and durometer tests that are performed. Furthermore, the eight chain model with the Pade approximant is capable of predicting N and the locking stretch λ_L for different mixing compositions without performing additional tension or compression tests.

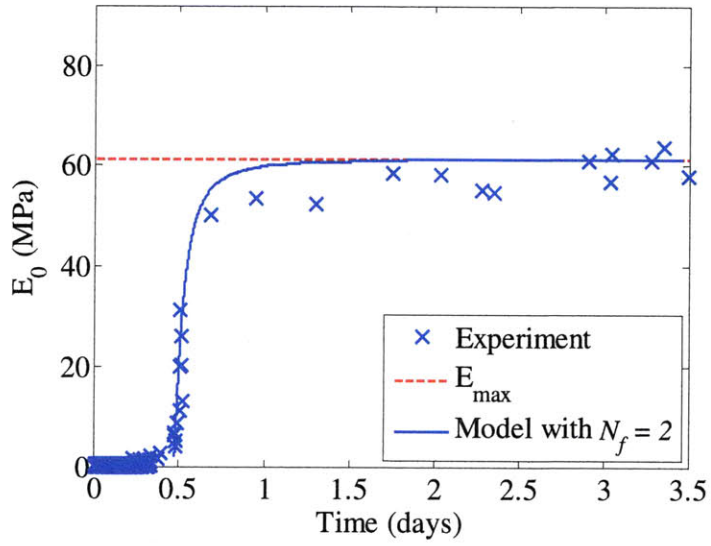

Figure 3-14: Isothermal modulus model (solid) and micro-indentation modulus measurement ("x") at room temperature during cure.

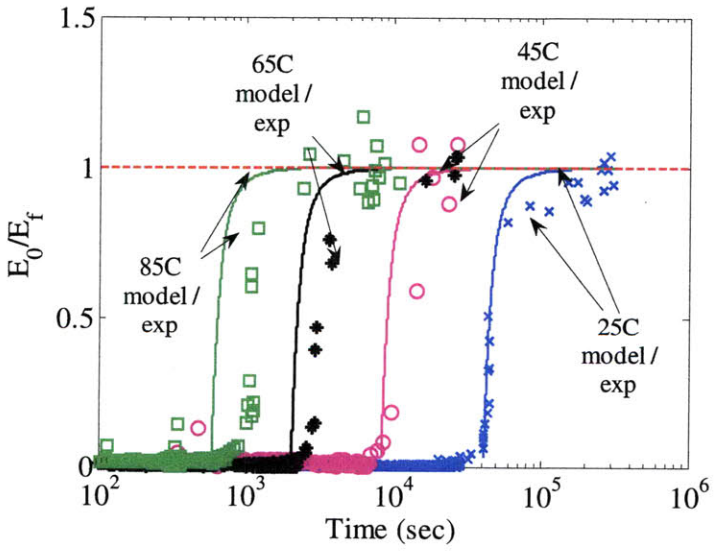

Figure 3-15: Modulus model and experiment at different process temperatures.

Micro-indentation is then shown as a method to measure modulus change over time. The Oliver-Pharr method is particularly useful for extracting modulus when indenting during cure, because of the viscoelastic behavior of the material. Although the absolute value of the modulus is measured to be higher than its true value, its trend is consistent with an isothermal reaction rate model at room temperature. Furthermore, micro-indentation shows a marked increase in modulus at the gel point, and can be used with strategies described in Chapter 5 to increase the cure process rate.

Nomenclature

E = Young's modulus [N/m^2]
E_0 = small strain initial Young's modulus [N/m^2]
h = indentation depth [m]
k = Boltzmann's constant [J/K]
n = chain density, or incremental crosslink density after gelation [m^{-3}]
N = number of links per chain
N_{stoich} = number of links per chain at a mixing ratio of R_{stoich}
p, p_{gel} = cure extent, cure extent at gelation
$P(t)$ = indentation load [N]
$r(h)$ = radius of the indentation contact radius [m]
R = indentation spherical tip radius [m]
R_{mix}, R_{stoich} = mixing and stoichiometric ratio of base to curing agent
$S(t)$ = indentation unloading slope [N/m]
$z(x)$ = axis-symmetric depth of the tip [m]
ν = Poisson's ratio

CHAPTER

4

PROCESS-INDUCED SHRINKAGE AND WARPAGE IN PDMS

Curing PDMS at room temperature takes days. To speed up the cure, the sample is heated. If PDMS is cured at an elevated temperature, it gels to a solid at that temperature. When it is cooled down to room temperature, thermal contraction typically occurs. Bulk contractions cause replicated features to shrink from the master mold, while spatial gradients cause the entire part to warp. The presence of shrinkage is noted in literature, but its dependence on process temperature has yet to be explored in depth. This chapter presents linear models for predicting shrinkage and warpage, and non-dimensional parameters that are relevant to the relationship. Although these models are valid for low temperature cures, experimental results show that knowledge of the gel temperature is required to determine shrinkage and warpage at higher temperatures.

In order to determine the gel temperature at these higher temperature cures, several analytical approximations and numerical techniques are presented. These analytical approximations can be used to advise when process temperature has a greater impact on process rate. The lower bound for process time and upper bound for shrinkage and warpage can also be determined. Using these numerical techniques, the dependence of shrinkage and warpage on process temperature can be established, and plots similar to Figure 1-7 can be generated and used to determine the ideal temperature for the process.

The chemical reaction in thermosetting polymers is accelerated in the presence of heat. The distribution of this heat in time and space affects the rate at which the polymer cures and the rate at which cure extent increases. Crosslinking chemistry and the origin of the reaction rate equation will be reviewed. This is followed by a lumped parameter model for heat transfer to the part, which is applied to two limiting cure conditions. In thin polymers, or under slow reaction

rates, temperature is assumed to be constant with time. In thick polymers, or under fast reaction rates, temperature increases linearly with time. For conditions where neither of these assumptions is valid, a numerical method is described.

4.1 Background

Many cases of thermal contraction during PDMS cure have been documented in literature [20, 28, 55-59]. These are tabulated in Table 4.1 and plotted in Figure 4-1. When designing a device, thermal contraction is important, since it may adversely affect flow behavior and device functionality. When assembling a multilayer device, an understanding of thermal contraction is important, since mismatches can result in overlay problems. Assembling two parts of unknown shapes can also result in void entrapments or decreased bond strength. Many of these problems can be compensated for by oversizing features during mold design, or by trial and error in adjusting process inputs like cure temperature. Knowing precisely how much to oversize and at what temperature to cure can significantly improve the quality of devices produced and decrease the time required to determine the ideal process conditions.

One thought is that the majority of shrinkage occurs from thermal contraction after cure. In other words, when PDMS changes from a liquid to a solid, it takes the shape of its surroundings at that temperature and pressure. When this transition occurs during the cure process, PDMS is usually at a temperature above ambient and at atmospheric pressure. Subsequent changes in temperature impose thermal strain on the PDMS part. Consequently, cooling after the cure process causes the PDMS part to shrink.

Other potential sources of shrinkage include chemical shrinkage due to outgassing, or structural shrinkage due to new molecular bonds formed by crosslinks during cure. Although chemical shrinkage has been observed with certain PDMS variants, this study concentrates on Sylgard 184, which only exhibits thermal shrinkage. Consequently, a room temperature cure causes no shrinkage in Sylgard 184 PDMS. However, because chemical and structural shrinkage in other variants are independent of the time-temperature history, they can potentially be compensated for with a constant design offset.

Very few thermal studies have been performed on the shrinkage of PDMS. The manufacturer's datasheet for Sylgard 184 estimates shrinkage of approximately 1%. Qualitatively, Michel [60] explained that thermal and chemical shrinkages are small and can

Table 4.1: Shrinkage of Sylgard 184 PDMS.

Source	Process Temperature (°C)	Shrinkage
[55]	25	0.25%
[56]	60	1.10%
[57]	60	1.50%
[55]	65	1.50%
[20]	65	1.07%
[58]	70	0.92%
[59]	75	1.00%
[28]	75	1.00%
[20]	80	1.54%
[61]	80	1.70%
[20]	100	1.98%

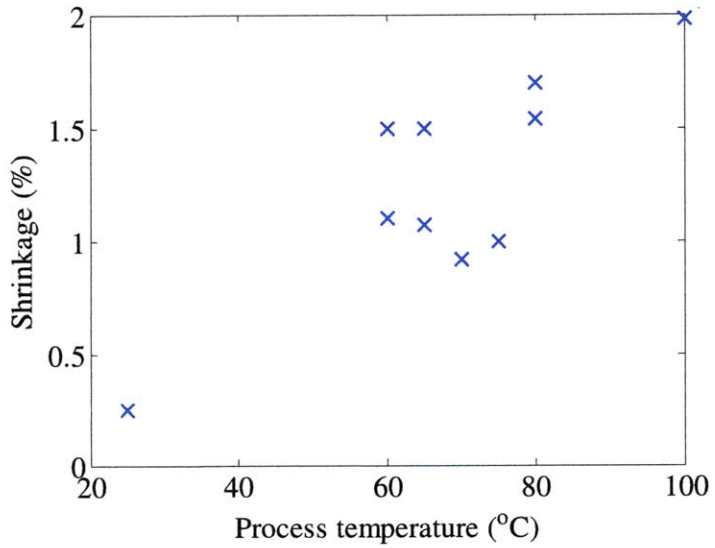

Figure 4-1: Reported shrinkage values in Sylgard 184 PDMS in literature, listed in Table 4.1.

currently be compensated for in the design of the master patterning tool; however, to further improve soft lithography, shrinkage must be more accurately modeled. Choi [56] identified low shrinkage as an important factor for multilevel pattern registration over large areas. Rogers [34] identified shrinkage as a key contributor to distortion, which can be qualitatively analyzed using Moire techniques. Pagliara [62] performed a study on registration errors; however, he did not explicitly account for shrinkage.

Quantitatively, the only formal shrinkage study on PDMS was performed by Lee [20]. Lee examined shrinkage while varying cure process temperature and the mixing ratio of base to curing agent. At 65C, 80C, and 100C, shrinkage was found to be approximately linear with process temperature, but uncorrelated to the mixing composition ratio. Shrinkage was related to process temperature by a linear coefficient of 258 μm/m-K, which is slightly below Dow Corning's published value for the coefficient of thermal expansion of 325 μm/m-K [19]. Lee concluded that shrinkage was correlated to thermal expansion, but provided no explicit relationship.

4.2 Shrinkage

To explore the relationship between process temperature and shrinkage, this study begins by examining bulk lateral shrinkage. Shrinkage is an important characteristic on many length scales. On chip scale lengths on the order of 10s of mm, it can affect alignment during assembly. On feature scale lengths on the order of 10s of μm, it can affect functional characteristics. In both cases, it is important to quantify shrinkage, and determine the factors that affect its value. In this section a set of lateral shrinkage experiments are performed, and the results on the relationship between shrinkage and process temperature are discussed.

4.2.1 Shrinkage model

Gelation describes the point during the cure process when PDMS transitions from a liquid to solid. Shrinkage is believed to be described by thermal strain on a part cooled from its temperature at gelation T_{gel}, to room temperature T_{rm}. Consequently, shrinkage is assumed to be given by

$$\varepsilon = \alpha\left(T_{gel} - T_{rm}\right) \tag{4.1}$$

where ε is linear thermal strain, defined by a change in length over original length, and α is the linear coefficient of thermal expansion. For Sylgard 184, α = 325 μm/m-K. If the reaction occurs slowly, the part reaches thermal equilibrium before it reaches gelation. In an ideal thermal system, the part heats to the process temperature $T_{setpoint}$ at thermal equilibrium so $T_{gel} = T_{setpoint}$ and shrinkage is given by

$$\varepsilon = \alpha\left(T_{setpoint} - T_{rm}\right) \tag{4.2}$$

In a real thermal system, there are boundary conditions and temperature gradients throughout the part. A common method for curing PDMS is on a hotplate. In the case of hotplate heating, a more accurate model accounts for contact resistance and natural convection. Contact resistance between the bottom surface of PDMS and the hotplate is described by a heat transfer coefficient $h_{contact}$, and natural convection between the top surface and air is described by h_{air}. The heat transfer coefficient $h_{contact}$ takes into account the resistance between the tooling and PDMS, as well as the tooling and the hotplate. At thermal equilibrium, the temperature profile across the thickness of the part is linear, and can be modeled as $T_{equil}(z)$:

$$T_{equil}(z) = T_{setpoint} - \frac{\left(h_{contact}h_{air}\right)k\left(T_{setpoint} - T_{rm}\right)}{k\left(h_{contact} + h_{air}\right) + \left(h_{contact}h_{air}\right)L}\left(\frac{1}{h_{contact}} - \frac{z}{k}\right) \tag{4.3}$$

where z is the vertical distance from the hotplate, k is the conduction coefficient and L is the thickness of the part. Using the average value for gel temperature, bulk lateral shrinkage can be modeled as

$$\varepsilon = \alpha\left(1 - \frac{\left(h_{contact}h_{air}\right)k}{k\left(h_{contact} + h_{air}\right) + \left(h_{contact}h_{air}\right)L}\left(\frac{1}{h_{contact}} - \frac{L}{2k}\right)\right)\left(T_{setpoint} - T_{rm}\right) \tag{4.4}$$

It is convenient to define several dimensionless Biot numbers to simplify Equation (4.4). First,

$$Bi = \frac{h_{char} L}{k} \tag{4.5}$$

where the quantity h_{char} is the characteristic heat transfer coefficient, and defined by the equivalent series heat transfer coefficient of the top and bottom surfaces:

$$h_{char} = \left(\frac{1}{h_{air}} + \frac{1}{h_{contact}} \right)^{-1} = \frac{h_{air} h_{contact}}{h_{air} + h_{contact}} \tag{4.6}$$

A second Biot number for the contact resistance of the hotplate can also be defined:

$$Bi_{contact} = \frac{h_{contact} L}{k} \tag{4.7}$$

The heat transfer coefficients used to calculate the Biot numbers in Equations (4.6) and (4.7) are found to be approximately 100, and the thermal conductivity approximately 0.2. Consequently, a sample part of thickness 2 mm produces a Biot number of 1. Real microfluidic devices consist of PDMS layers that are typically a few hundred microns to a few millimeters thick. Using the dimensionless Biot numbers in Equations (4.5) and (4.7), Equation (4.4) can be expressed in terms of dimensionless temperature, which is non-dimensionalized by multiplying temperature by its thermal expansion coefficient α:

$$\varepsilon = \left(1 - \frac{Bi / Bi_{contact}}{Bi + 1} - \frac{1}{2} \frac{Bi}{Bi + 1} \right) \left[\alpha \left(T_{setpoint} - T_{rm} \right) \right] \tag{4.8}$$

Equation (4.8) is a linear function of setpoint temperature. However, the slope is smaller than Equation (4.2) because of heat losses in real systems, which is represented here by non-zero values for *Bi*. Lee also observed a linear relationship between process temperature and shrinkage that was smaller than the coefficient of thermal expansion.

4.2.2 Experimental setup for measuring shrinkage

To evaluate the dependence of shrinkage on process temperature, samples were produced by casting PDMS into the μFAC bulk metallic glass (BMG) mold [8], shown Figure 4-2. The BMG tool is a $Zr_{41.2}Ti_{13.8}Cu_{12.5}Ni_{10}Be_{22.5}$ (Vitreloy-1) alloy, with a thermal expansion coefficient

of about 32 μm/m-K [63], which is an order of magnitude less than Sylgard 184. PDMS was cast over the BMG tool to a thickness of 2.1 mm, and placed onto a hotplate at temperatures between 75C and 200C. After curing to manufacturer specifications [19], the PDMS was removed from the mold and diced as shown in Figure 4-3. The gratings portion of the pattern, circled in red on Figure 4-4a, was measured to determine shrinkage. These gratings were then imaged with a Dino-Lite Pro AM413T5 optical microscope. Gratings images of the tool and PDMS replica are shown in Figure 4-4c and Figure 4-4d. PDMS is capable of replicating nano-scale features, so even surface scratches on the BMG tool can be seen replicated into the PDMS samples.

For the purpose of this shrinkage study, two channels were picked from the field of grating to maximize the distance in the field of view. An individual grating is schematically shown in Figure 4-4b. Each grating has a width of 25 μm, and is spaced 50 μm apart. Points along their edges are selected and fitted to lines to calculate the normal distance between the gratings. The nominal distance between the outermost edges of the first and 17th gratings on the tool design is 875 μm. The actual distances on the tool and replicas are measured and computed with a custom MATLAB script, and the change in distance is plotted as its shrinkage.

4.2.3 Shrinkage results

The thermal strain ε is given by the shrinkage $\Delta l/l$, where l is the linear spacing between the first and 17th gratings, Δl is the change in this spacing from master to replica:

$$\varepsilon = \frac{\Delta l}{l} \tag{4.9}$$

In Figure 4-5, shrinkage is plotted as a function of the hotplate setpoint temperature. In Figure 4-6, shrinkage is plotted on non-dimensional axes, as described by Equation (4.8). Shown by the blue crosses are the measured shrinkages of the samples, while shown by the red dashed line is the simple model described in Equation (4.2). For temperatures below 100C, shrinkage increases linearly to setpoint temperature, with the slope proposed by Equation (4.2). However, shrinkage observed at higher temperatures is smaller than predicted, and this error increases with setpoint temperature in Figure 4-5. One option is to calibrate for the contact resistance, but Equation (4.4) is still linear with setpoint temperature. Another option is to test if this downward trend is statistically significant.

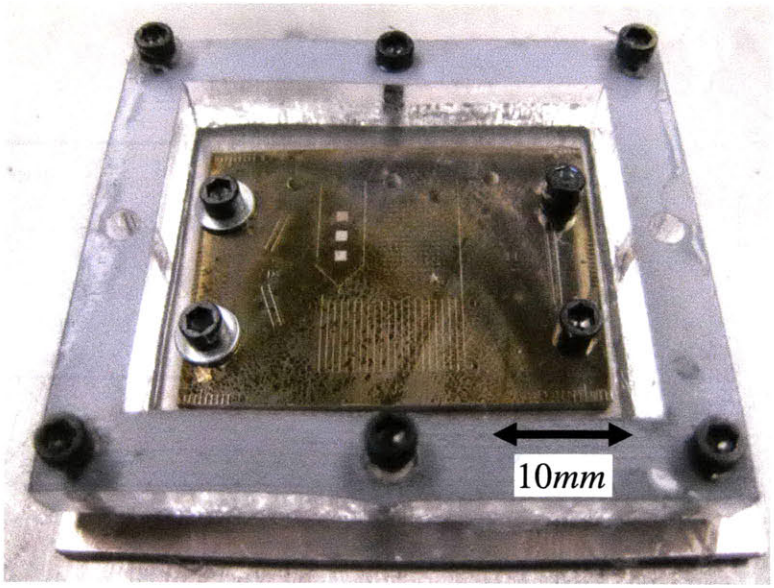

Figure 4-2: Bulk metallic glass (BMG) mold for PDMS replication.

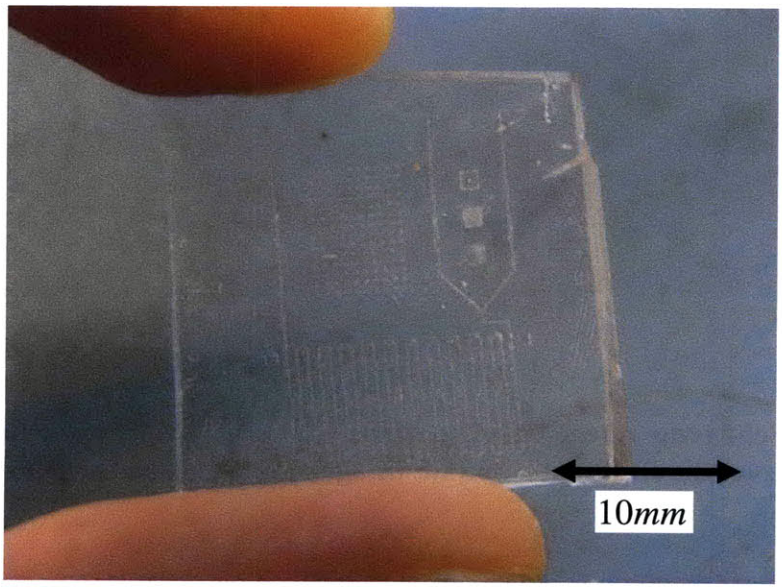

Figure 4-3: Diced PDMS replica.

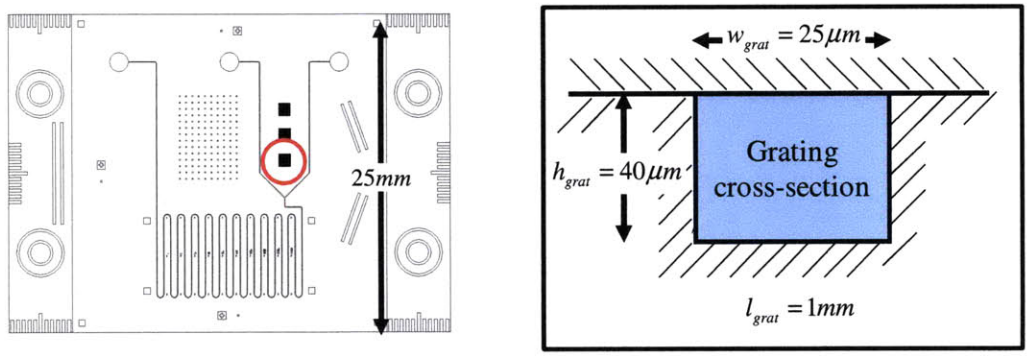

(a) (b)

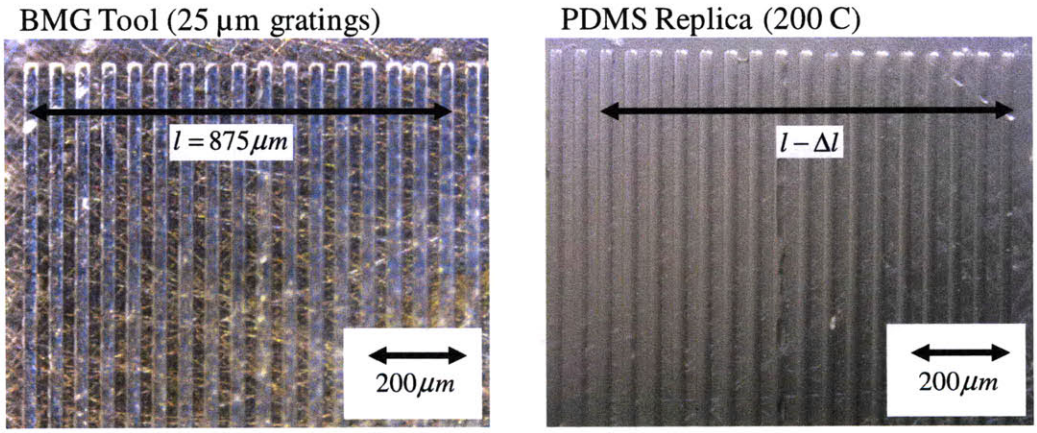

(c) (d)

Figure 4-4: (a) Schematic of the µFAC pattern , (b) cross-section of a single grating, (c) image of gratings on the BMG tool, and (d) image of gratings on the PDMS replica.

From Equation (4.1), shrinkage must be zero at room temperature, so the relationship of shrinkage and setpoint temperature can be mathematically modeled by a polynomial expansion of the following form:

$$\frac{\Delta l}{l} = C_1\left(T_{setpoint} - T_{rm}\right) + C_2\left(T_{setpoint} - T_{rm}\right)^2 + C_3\left(T_{setpoint} - T_{rm}\right)^3 + \ldots \qquad (4.10)$$

The linear coefficient C_1 is physically related to the coefficient of thermal expansion and the slope in Equation (4.4). However, higher order coefficients have no physical meaning in this model. They are included to test if the linear model in Equation (4.4) is sufficient.

Linear regression is performed to determine the coefficients C_1, C_2, and C_3 for linear, quadratic, and cubic forms of Equation (4.10). Coefficients are determined and tabulated in Table 4.2. The linear and quadratic fits are plotted in Figure 4-7, which shows that an additional quadratic term can significantly improve the fit of the model. Furthermore, the mean square errors in the higher order models can be compared with the pure error to determine if the lack of fit in the lower order models is statistically significant. Pure error is calculated from the variability of the replicates. The sum of squares (SS), degrees of freedom (DOF), mean square (MS), F-ratio, and p-values are tabulated in Table 4.3. The p-value increases significantly from the linear to quadratic models, and confirms that a linear model is indeed inadequate.

Furthermore, as additional higher order terms are included, the linear coefficient C_1 approaches a value slightly below the manufacture specified linear coefficient of thermal expansion for Sylgard 184, which is also consistent with Equation (4.4). The R^2 value also increases significantly with the addition of a quadratic term, although less drastically when higher order coefficients are added. These values are shown in Table 4.2.

Physically, these higher order terms are believed to result because gelation occurs before the PDMS part internally reaches thermal equilibrium. This results in a gel temperature below the average steady state temperature described by Equation (4.4). Consequently, when PDMS is cooled back down to room temperature, a smaller shrinkage value is observed at high temperatures. Determination of this gel temperature requires additional understanding of the cure kinetics. The gel temperature will be found using a thermo-chemical model described in Section 4.4, and validated in Section 4.7.2.

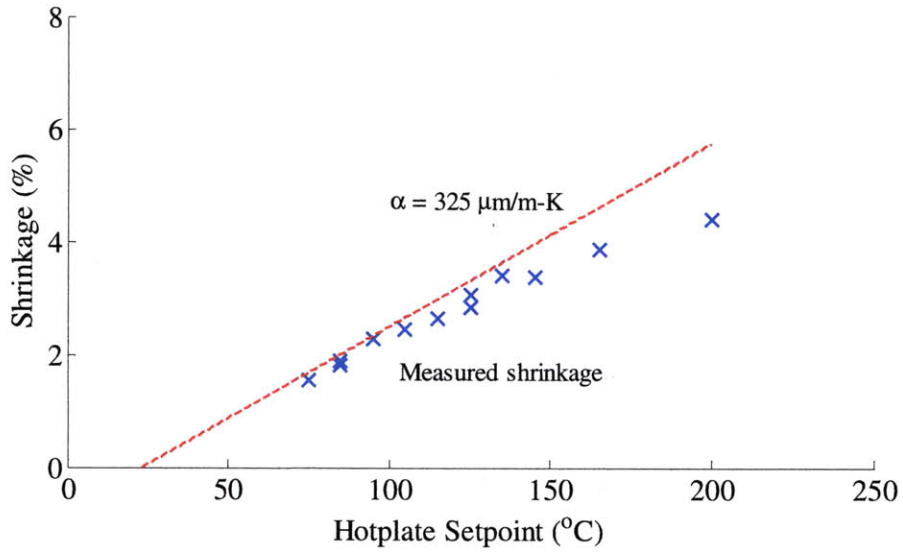

Figure 4-5: Lateral shrinkage at various cure temperatures is bounded by the linear coefficient of thermal expansion.

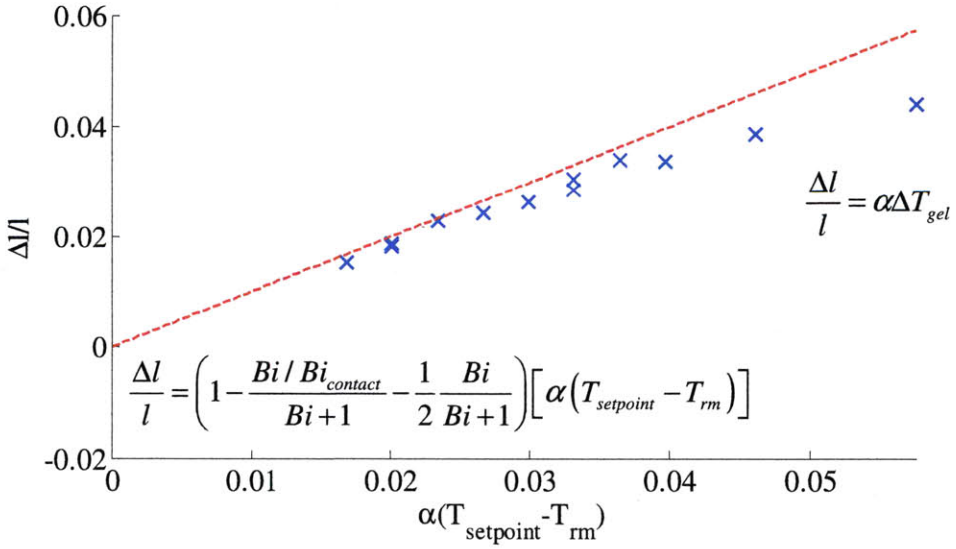

Figure 4-6: Non-dimensional shrinkage plotted against non-dimensional temperature.

Table 4.2: Regression coefficients for bulk shrinkage.

Order	C_1 (μm/m-K)	C_2 (μm/m-K^2)	C_3 (μm/m-K^3)	R^2
Linear	284	-	-	0.92
Quadratic	352	-0.556	-	0.98
Cubic	319	0.041	-0.002	0.99

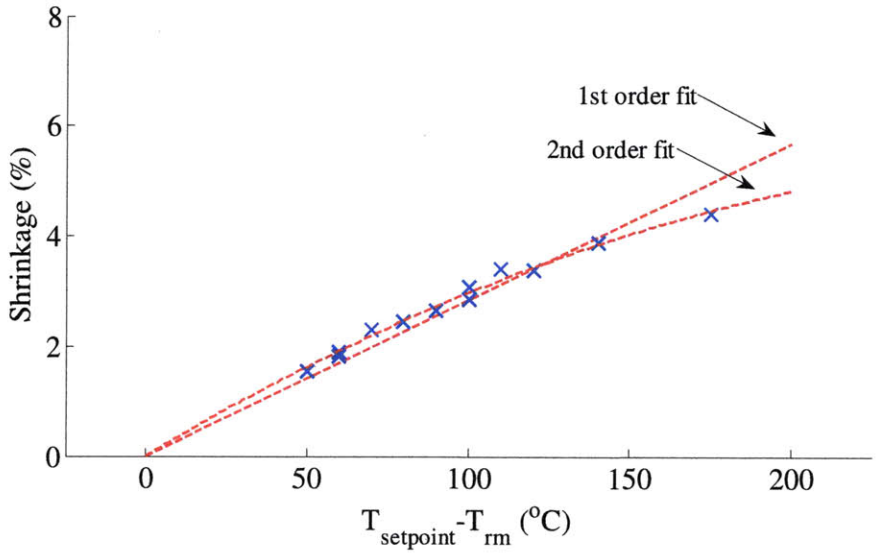

Figure 4-7: Higher order terms significantly improve fit for bulk shrinkage.

Table 4.3: Statistical significance of higher order terms.

	SS	DOF	MS	F ratio	p-value
Total		11			
Pure	0.027	2	0.0133		
Linear Err	0.650	8	0.0779	6.10	0.148
Quad Err	0.102	7	0.0107	1.09	0.557
Cubic Err	0.088	6	0.0102	1.10	0.548

4.3 Warpage

Part concavity is important during assembly and bonding. Two concave parts pressed into contact will trap air bubbles or voids. On the other hand, two convex parts pressed into contact will initially touch at a single point and grow a single surface towards the edge of the part. The impact of concavity on bond strength has yet to be analyzed in detail, but ideally, mildly convex parts are desirable to minimize the possibility of trapped air or voids.

4.3.1 Curvature model

Curvature is observed when there is an asymmetric vertical gradient in the gel temperature of a part. Mismatched strains as the part cools to room temperature can cause the part to bow. Figure 4-10a shows a viscous pre-polymer cast into the shape of a flat rectangular sample. As the sample is heated in Figure 4-10b, it crosses the gel point at different gel times t_{gel} throughout the sample. The temperatures at these gel times are given by the gel temperatures T_{gel}, and are a function of position, as shown in Figure 4-10c. Consequently, if $\Delta T_{gel}(z)$ is the difference between gel temperature and ambient at a distance z from the hotplate, it is possible to balance moments and estimate curvature by the strain equation

$$\kappa = \frac{12\alpha}{L^3}\int_{\frac{L}{2}}^{\frac{L}{2}} z\left\{\Delta T_{gel}(z)\right\}dz \tag{4.11}$$

In Equation (4.11), α is the coefficient of thermal expansion, and L is the thickness of the part. In the case of hotplate curing, the equilibrium temperature gradient is a linear function of z, as derived in Equation (4.3). The resulting curvature is shown in Figure 4-10d. If everywhere the polymer reaches thermal equilibrium before t_{gel}, $\Delta T_{gel}(z)$ can be linearly modeled as

$$\Delta T_{gel}(z) = \frac{\Delta T_{total}}{L} z \tag{4.12}$$

where ΔT_{total} is the difference between equilibrium temperatures at the top and bottom surfaces. This is the specific case shown in Figure 4-10c. Consequently, curvature is exactly calculated by

$$\kappa = \frac{\alpha \Delta T_{total}}{L} \tag{4.13}$$

If the heating mechanism is symmetric, ΔT_{total} is zero and there is no curvature. Consequently, a double sided heating strategy is ideal for PDMS curing. However, as a case study, we will consider hotplate curing, since this is commonly used today, and gives us a way to purposefully impose a gel temperature gradient into a part and measure shrinkage more accurately. In hotplate curing, ΔT_{total} is determined by conduction and the heat transfer coefficients on the boundaries. Under this condition,

$$\Delta T_{total} = \frac{(h_{contact} h_{air}) L}{k(h_{contact} + h_{air}) + (h_{contact} h_{air}) L} (T_{setpoint} - T_{rm}) \tag{4.14}$$

As with the linear models for lateral shrinkage, these conditions only apply at low temperatures. Consequently, curvature at low temperatures also approaches a linear function of setpoint temperature.

$$\kappa = \frac{(h_{contact} h_{air}) \alpha}{k(h_{contact} + h_{air}) + (h_{contact} h_{air}) L} (T_{setpoint} - T_{rm}) \tag{4.15}$$

Non-dimensional curvature can be defined as curvature multiplied by its thickness L, and written as a function of non-dimensional temperature and the Biot number defined by Equation (4.5).

$$\kappa L = \left(\frac{Bi}{Bi + 1} \right) \left[\alpha (T_{setpoint} - T_{rm}) \right] \tag{4.16}$$

As the Biot number approaches zero, as in the case of very thin parts, curvature approaches zero as well.

4.3.2 Experimental setup for measuring curvature

To evaluate curvature dependence on process temperatures, a hotplate was set at temperatures between room temperature and 230C. At each process temperature, six parts were cured in the blank aluminum mold shown in Figure 4-8, according to Dow Corning's recommended cure times [19], and measured using a KLA-Tencor P10 contact profilometer

shown in Figure 4-9. Each part was 33 mm by 25 mm, and 2.7 mm thick. A 17 mm scan was taken across the center of the part, and the maximum deflection of the sample was measured. This deflection can be converted to curvature by the parabolic approximation in Equation (4.17), where w is the scan length.

$$\kappa \approx \frac{8d_{\max}}{w^2} \tag{4.17}$$

4.3.3 Curvature results

The resulting curvatures are plotted in Figure 4-11. Non-dimensional curvature is plotted in Figure 4-12. One way to interpret these results is to divide Figure 4-11 into three regions. The first region is below 85C, where the polymer reaches a steady state temperature gradient before much of the reaction has occurred. This is where Equation (4.15) is applicable. The dashed red line in Figure 4-11 depicts this linear low temperature model, where constants are given by Table 4.. Between 100C and 150C, the average curvature is mostly unchanged, although the variance is high compared with the other two regions. Curing in the region occurs at the end of the temperature transient, as it approaches steady state. Finally at 170C and above, both curvature and variation appear to increase linearly with the setpoint temperature. In this region, curing occurs while temperature is increasing linearly. Currently, no model exists that is capable of describing all three regions. As with shrinkage, determination of $\Delta T_{gel}(z)$ is required to model mid- to high-temperature regions. Unlike shrinkage, the linear model is much less applicable at high temperatures.

4.4 Cure Models for PDMS

PDMS cure can be modeled as a heat conduction problem with heat generation. The time required for the polymer to transition from a cure extent of p_0 to p_f is estimated to model cure times, where p_0 is the initial cure extent and p_f is the target cure extent. The target cure extent can be any cure extent of interest, such as the gel point or fully cured point. Although a complete solution can be obtained numerically with finite element analysis, this can be tedious and computationally intensive. First, low temperature and high temperature approximations are provided to quickly estimate cure times in the limit and provide design rules. This is followed by

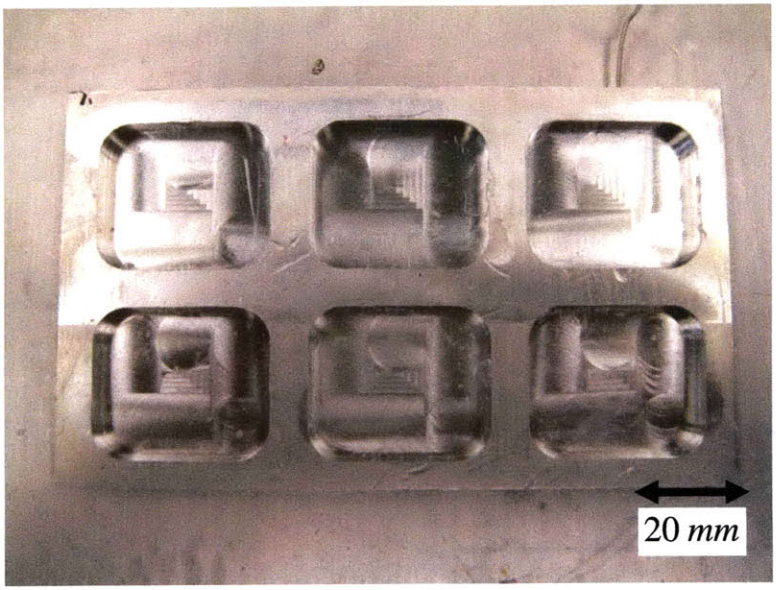

Figure 4-8: Aluminum mold for curvature experiment.

Figure 4-9: KLA-Tencor P10 surface profilometer.

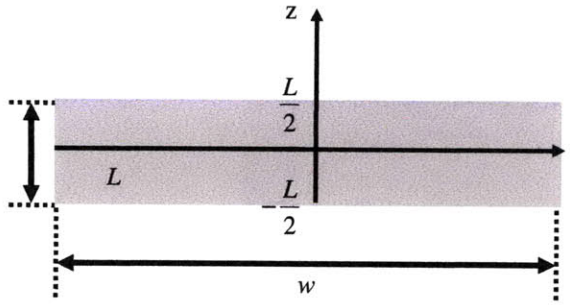

(a) Viscous pre-polymer takes form of mold

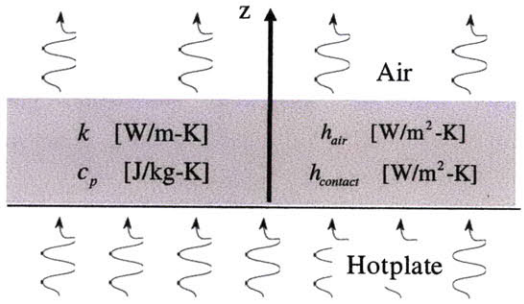

(b) Part temperature varies in space and time

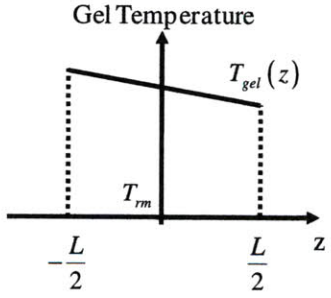

(c) Gel temperature varies in space

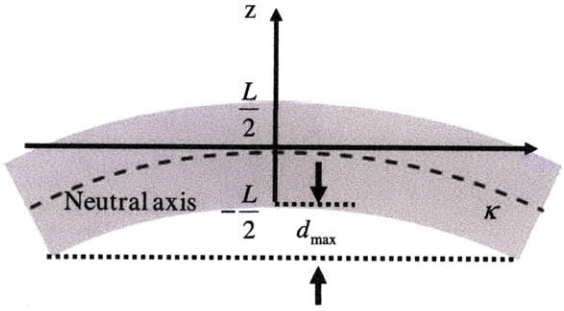

(d) Cooling creates shrinkage and curvature

Figure 4-10: In hotplate curing, curvature is caused when an asymmetric vertical gradient in gel temperature is cured into a part.

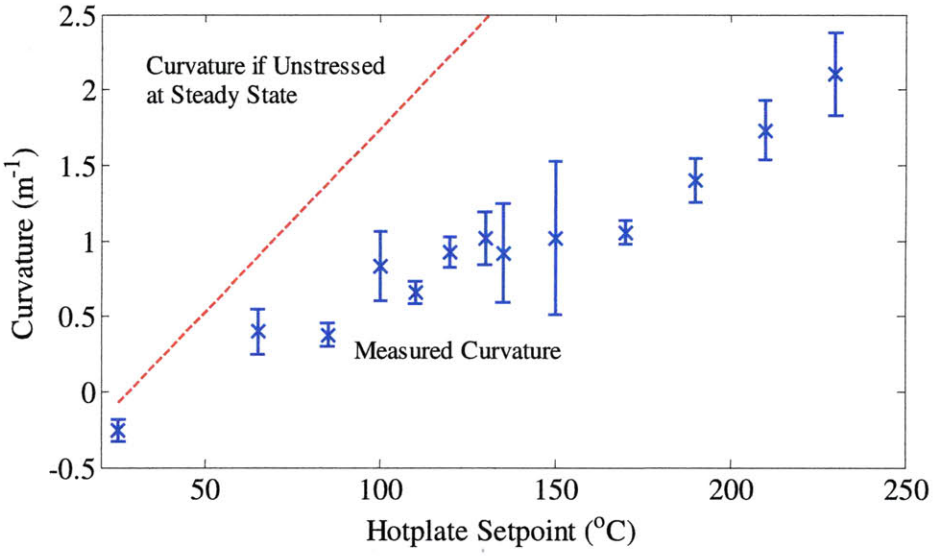

Figure 4-11: Locked in temperature gradient at various cure temperatures.

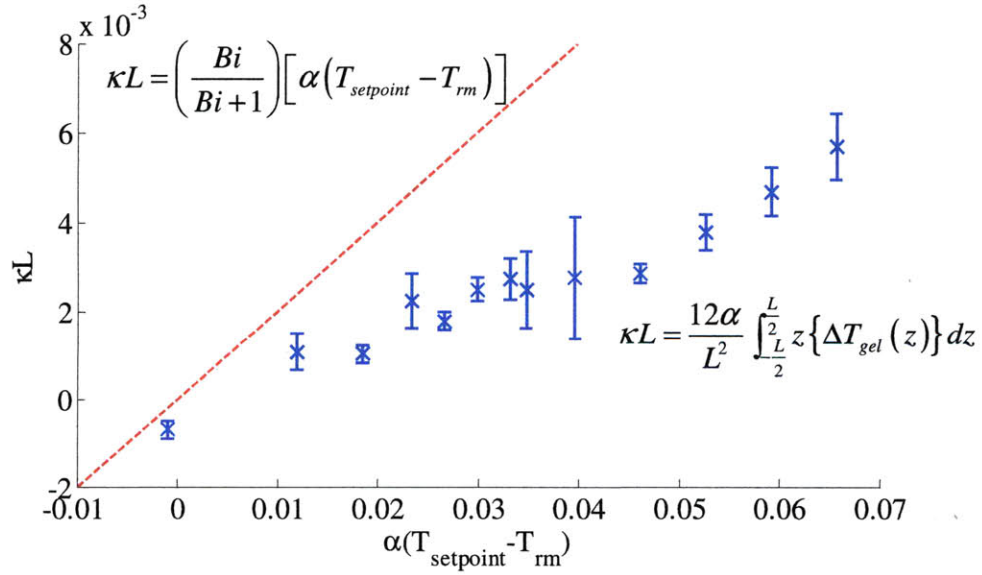

Figure 4-12: Non-dimensional curvature plotted against non-dimensional temperature.

a full numerical approach, when neither approximation suffices.

4.4.1 A thermal-chemical model with heat generation

The thermo-chemical model for the curing process can be described using the general heat conduction equation shown in Equation (4.18), where q is the heat generated from the exothermic crosslinking reaction, and ρ, c_p, and k are the density, specific heat, and conductivity, respectively, if the mixture is assumed to be homogeneous and isotropic.

$$\frac{\partial q}{\partial t} = k \cdot \nabla^2 T - \rho c_p \frac{\partial T}{\partial t} \tag{4.18}$$

Heat generation occurs when functional groups react and form crosslinks in an exothermic reaction. In the case of PDMS, functional groups are the hydrogen and vinyl groups that react to produce crosslinks. A finite amount of energy is released for every crosslink that is produced. The new bond that forms has smaller bond energy than the original hydrogen and vinyl bonds, so the excess energy is released as heat q. If q_{total} is the total heat produced when all crosslinks have formed, the heat generated at a given cure extent p can be written as

$$\frac{\partial q}{\partial t} = q_{total} \cdot \frac{dp}{dt} \tag{4.19}$$

The heat generation in Equation (4.18) is directly proportional to the reaction rate used to describe crosslinking.

4.4.2 Curing kinetics

Sbirrazzuoli [64] gives several forms for the reaction rate equation. Different equations are applicable for different polymers. With Sylgard 184, curing kinetics can be described with the reaction rate and Arrhenius relationship shown in Equation (4.20). Reaction and cure are often used interchangeably, since the reaction is complete when the polymer is fully cured.

$$\frac{dp}{dt} = k(T) p^m (1-p)^n, \quad k(T) = k_0 e^{-E/RT} \tag{4.20}$$

In Equation (4.20), dp/dt is the cure rate, p is the cure extent, k_0 is the pre-exponential constant, E

is the activation energy, R is the gas constant, and T is the polymer temperature. The Arrhenius equation $k(T)$ describes the dependence of cure rate on temperature. The term p^m models the availability of catalyst, while $(1-p)^n$ accounts for the amount of reagents available for reaction. In a thermoset, the reagents are the functional groups that are still available for crosslinking. The initial stage of the reaction resembles standard addition polymerization, where the rate is proportional to p^m. Next, termination reactions become diffusion limited because of an increase in viscosity. Finally, when the material becomes rubbery, the propagation reaction becomes diffusion limited and resembles autoacceleration. Vitrification isolates some of the unreacted functional groups and prevents cure extent from ever reaching 100%.

Both parameters m and n are conventionally found empirically. ASTM procedure E2070-08 outlines procedures to determine the parameters, using data measured with a differential scanning calorimeter (DSC). By applying constant temperature to small volumes of PDMS, isothermal curves can be produced to provide insight to heat generation in the polymer. In addition to model parameters, cure times at various temperatures can be determined from these experiments.

4.4.3 Lumped parameter model

Temperature is coupled with the reaction rate equation, so cure extent is determined by solving Equations (4.18) and (4.20) simultaneously. However, this is difficult to perform analytically, and several simplifying assumptions can be made to estimate a solution. First, a lumped parameter model can be used if the temperature T is approximately uniform throughout the body of the part. This is true for parts with small Biot numbers Bi, defined by Equation (4.5). Next, the heat generation contribution is assumed to be small compared with heat conduction. This is true if the total heat produced does not significantly change the temperature of the part, as in the case when the reaction occurs over a long period of time. Lastly, the top surface of the part is assumed to be a perfect insulator so that $h_{char} = h_{contact}$. When all of these assumptions hold, the temperature history of the part can be characterized by the first order expression

$$T = T_{setpoint} - \left(T_{setpoint} - T_{rm}\right) e^{-t/\tau} \tag{4.21}$$

with time constant τ

$$\tau = \frac{\rho c_p L}{h_{contact}} \tag{4.22}$$

where ρ is the density, c_p is the specific heat, and L is the part thickness. The time constant τ consists of material and geometric properties, which are independent of the process temperature.

The cure time can be found by rewriting Equation (4.20) as dimensionless integrals, and solving for the time difference $\Delta t = t_f - t_0$.

$$\int_{p_0}^{p_f} \frac{1}{p^m (1-p)^n} dp = \int_0^{t_f} k_0 \exp(\frac{-E}{RT}) dt \tag{4.23}$$

When these integrals are taken from the beginning of a cure process, $t_0 = 0$ and p_0 is the initial cure extent. It follows that the time t_f is the time to reach a cure extent of p_f. The quantity $\Delta t/\tau$ tells us if temperature can be approximated as constant or linear with time during the process.

To estimate $\Delta t/\tau$, it can be first assumed that the temperature history is constant. Equation (4.23) is solved directly and if $\Delta t/\tau >> 1$, this assumption is indeed correct. The isothermal analysis in Section 4.4.4 can then be used. This is the case for many low temperature cures, since the reaction rate is small. On the other hand, if $\Delta t/\tau << 1$, it can be assumed that the temperature history increases linearly with time and the analysis in Section 4.4.5 can be used. This is the case for many high temperature cures when the reaction rate is much faster than the time constant τ, or when the part is thick and the interface resistance is large.

4.4.4 Low temperature limit: isothermal approximation

In the low temperature limit, cures occur at a constant temperature over time. This approximation is valid when $\Delta t/\tau >> 1$, or qualitatively for thin parts at low temperatures. To approximate Δt, Equation (4.23) can be solved with $m=n=1$ as

$$\Delta t = -\frac{1}{k_0 e^{\left(\frac{-E}{RT}\right)}} \ln\left(\frac{1-p_f}{1-p_o}\frac{p_o}{p_f}\right) \tag{4.24}$$

The parameters m and n are empirically found when calibrating Equation (4.20), and are usually between 1 and 2, although closer to 1. Qualitatively, increases in the constants m and n skew the

cure extent integrand in Equation (4.23) left and right. The integral is affected most when p_0 is close to 0% or p_f is close to 100%. However, Equations (4.22) and (4.24) provide a quick way to check the isothermal approximation.

Equation (4.24) describes the cure time required for the polymer to transition from a cure extent of p_0 to p_f. In practice, it is difficult to determine p_0 and p_f exactly for two points of interest, and m and n are often found to be between 1 and 2. Alternatively, cure times can be expressed as a dimensionless ratio of cure times at two cure temperatures. This gives an estimate of process time improvement, when comparing different isothermal processing temperatures. Integrating from a cure extent of p_0 to p_f always produces the same constant, so the right side can be evaluated and equated for arbitrary temperature trajectories between p_0 to p_f. For two isothermal temperature cures T_1 and T_2, the ratio of their cure times Δt_{T1} and Δt_{T2} are by

$$\frac{\Delta t_{T_2}}{\Delta t_{T_1}} = \exp\left[-\frac{E}{R}\left(\frac{1}{T_1}-\frac{1}{T_2}\right)\right] \tag{4.25}$$

This result is general, and does not assume that $m=n=1$. If Δt is known for one temperature, all other process times can be quickly extrapolated by using Equation (4.25).

Figure 4-13 shows such a curve on a log-linear plot, calibrated with Equation (4.24) for a cure extent from 0.02% to 67%. An initial cure extent of 0.02% is determined from the heated micro-indentation experiments that were performed in Chapter 3. A final cure extent of 67% is chosen because it is the cure extent at gelation for Sylgard 184. A practical result from this plot is that for isothermal cures performed between room temperature and 100C, the logarithm of cure time is nearly linear with hotplate setpoint. In this operating regime, the cure time decreases by approximately two times for every 10C. A Taylor series expansion of Equation (4.25) near T_1 shows that the slope is approximated by E/RT_1^2.

$$\ln\left(\frac{\Delta t_{T_2}}{\Delta t_{T_1}}\right) \approx \frac{E}{RT_1^2}(T_2 - T_1) + const \tag{4.26}$$

Near an operating point T_1 well above absolute zero, the relationship is linear and insensitive to small temperature changes.

This approximation matches well with cures times recommended by Dow Corning and

those reportedly used by other researchers, which are shown in Table 1.1 and plotted in Figure 4-14. These results show a cure time required to achieve a cure extent that is equivalent to Dow Corning's recommended cure at 100C. Using Equation (4.23), this cure extent is found to be 99.9%. It is interesting to note from Figure 4-14 that many researchers cure to approximately the equivalent cure extent as that recommended by Dow Corning, although cure extent now provides a quantitative metric for how we can achieve such an equivalent cure.

4.4.5 High temperature limit: linear temperature ramp

As the process temperature increases, the cure kinetics become faster and the majority of crosslinking occurs early in the cure cycle. In real thermal systems, heated parts do not instantaneously ramp to the setpoint temperature. Instead, these parts experience transients. If crosslinking occurs quickly, gelation can occur before thermal equilibrium is reached and the expressions in Section 4.4.4 are no longer adequate.

In order to address the case when gelation occurs before thermal equilibrium, the transient temperature response of the part can be examined and compared with the time to reach gelation. Figure 4-15a shows that as process temperature increases, reaction rate increases versus reaction extent. In Figure 4-15b, this shifts the reaction extent curve left versus time, so the time required to reach gelation decreases. In a lumped parameter model, the temperature response of the part is first order and can be described by Equation (4.21). This can be segmented into three regions shown in Figure 4-15c. On one extreme, temperature in Region I can be approximated as increasing linearly with time. On the other extreme, temperature in Region III can be approximated as constant. From Figure 4-15b and Figure 4-15d, as the process temperature increases, the time at gelation shifts from Region III towards Region I. Consequently, the temperature history can be approximated to be linear for cures that are clearly in Region I.

In Region I, the transient temperature response can be linearly approximated by Equation (4.27), where $\Delta T_{setpoint}$ is the temperature difference between room temperature T_{rm} and process temperature $T_{setpoint}$.

$$T = T_{rm} + \frac{\Delta T_{setpoint}}{\tau} t, \quad (t << \tau) \tag{4.27}$$

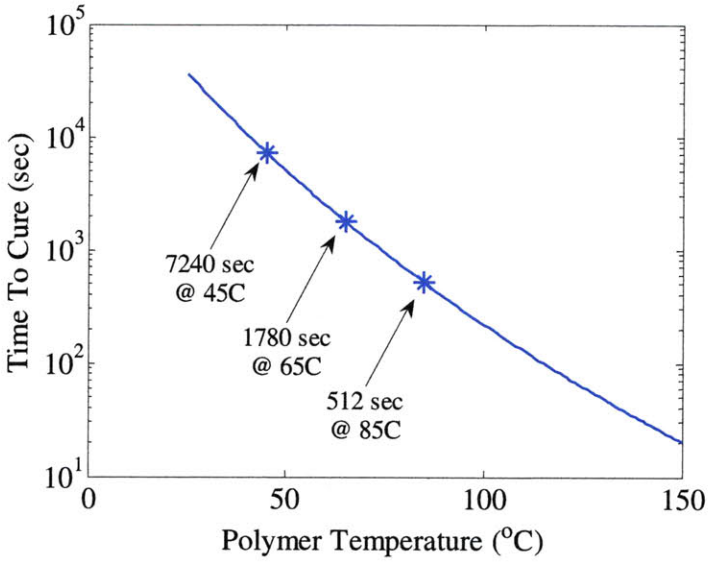

Figure 4-13: Isothermal model for time to gel from 0.02% to 67%.

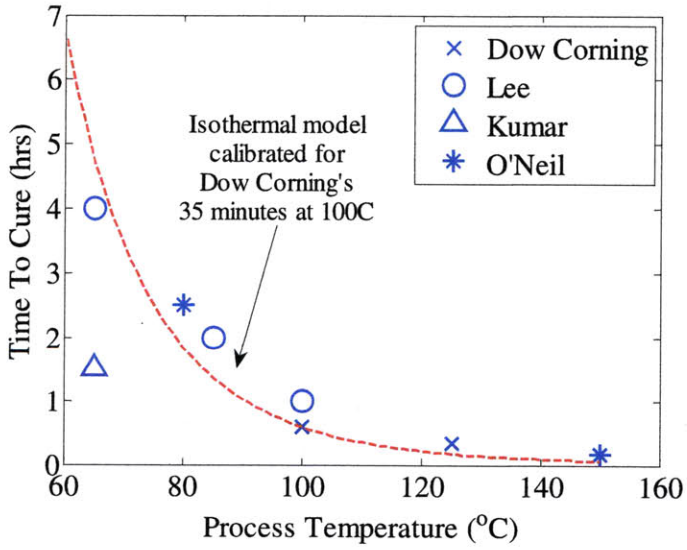

Figure 4-14: Typical cure times at different cure temperatures from Table 1.1, and the isothermal model for cure time calibrated with Dow Corning's 100C cure recommendation.

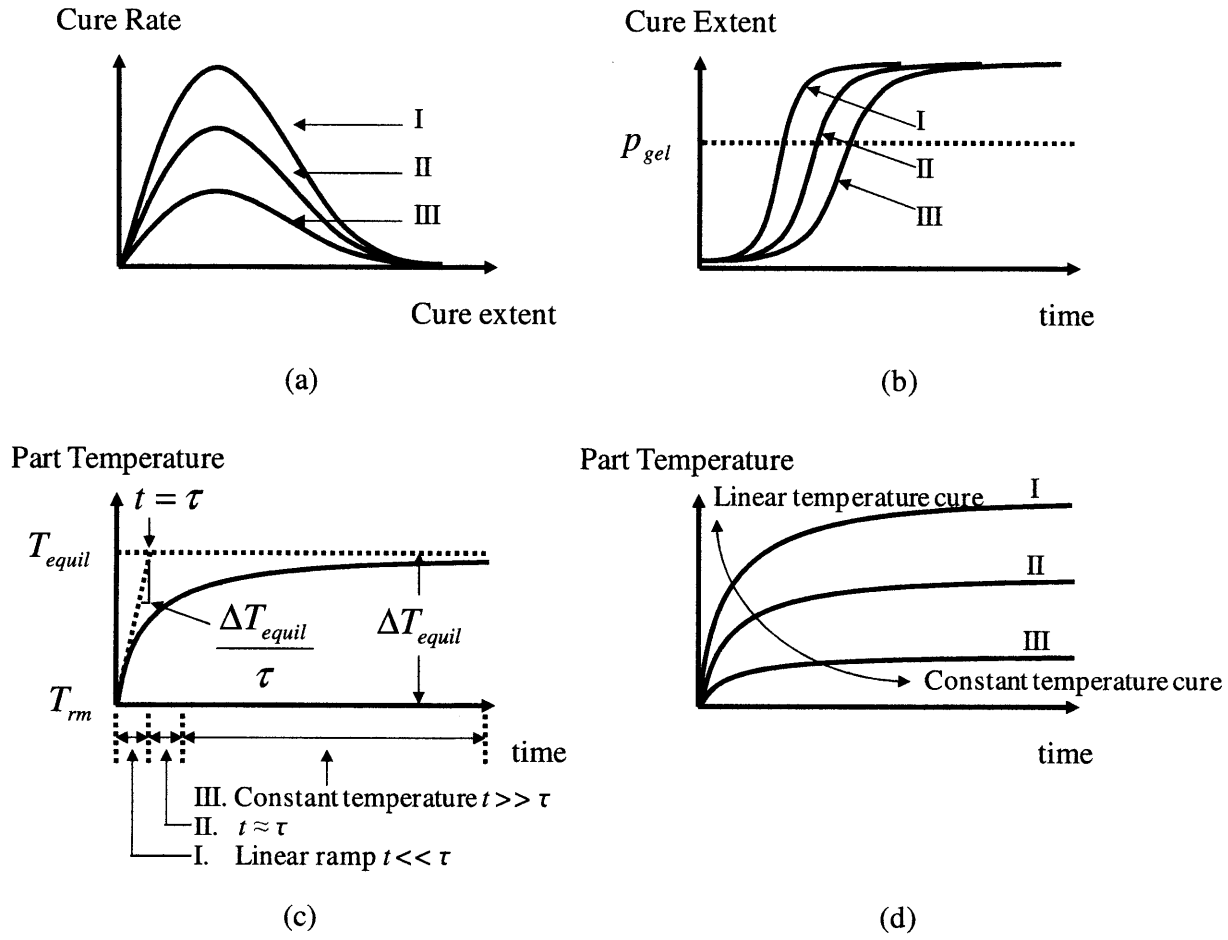

Figure 4-15: Curing at high (I), mid II), and low (III) temperature regimes. Increasing cure rate in (a) causes gelation to occur at an earlier time in (b). The transient temperature response in (c) is shown to occur in three stages, consequently, the gel point in (d) moves towards the linear regime for increasing cure rates.

The following approximation can also be made in Equation (4.28), when $\Delta T << T_{rm}$ and both temperature terms are expressed in Kelvin.

$$\frac{1}{T_{rm}+\frac{\Delta T_{setpoint}}{\tau}t}=\frac{1}{T_{rm}}-\frac{1}{T_{rm}^{\ 2}}t, \quad \left(t<<\frac{T_{rm}\tau}{\Delta T_{setpoint}}\right) \tag{4.28}$$

Equation (4.28) is automatically satisfied with Equation (4.27) when the step change in temperature is less than room temperature. This will always be true for PDMS, since thermal degradation occurs near 200C and curing should not occur at those temperature levels. When Equations (4.27) and (4.28) are applied to Equation (4.23), Equation (4.29) relates two cure times in the high temperature limit.

$$\Delta t_{Tf}=\frac{\ln\left(\frac{\Delta T_f}{\Delta T_i}\left[\exp\left(\frac{E}{R}\left(\frac{\Delta T_i/\tau}{T_{rm}^{\ 2}}\Delta t_{Ti}\right)\right)-1\right]+1\right)}{\frac{E}{R}\left(\frac{\Delta T_f/\tau}{T_{rm}^{\ 2}}\right)} \tag{4.29}$$

Unlike the isothermal expression in Equation (4.25), the high temperature relationship between cure times cannot be related by a pure ratio. The material and geometry parameter τ, and ambient condition T_{rm} impact the time required to cure. When plotted on the same figure, as τ decreases, the high temperature approximation shifts by nearly the same amount.

Plotted in Figure 4-16 are the gel times and gel temperatures for low and high temperature approximations. For gel times in Figure 4-16a, the low and high temperature approximations represent lower bounds that are valid far away from τ. They are lower bounds, since the temperature approximations in Figure 4-15c are always higher than the actual temperature of the part. Consequently, the higher temperatures speed up the reaction rate in the model and underestimate the actual gel time. For gel times much smaller or much greater than τ, the bounds become more realistic. Similarly, for gel temperatures in Figure 4-16b, the low and high temperature approximations represent upper bounds that are valid far away from τ. The reason these are upper bounds can again be seen from Figure 4-15c, since the temperature approximations are always higher than the actual temperature of the part. In both figures in

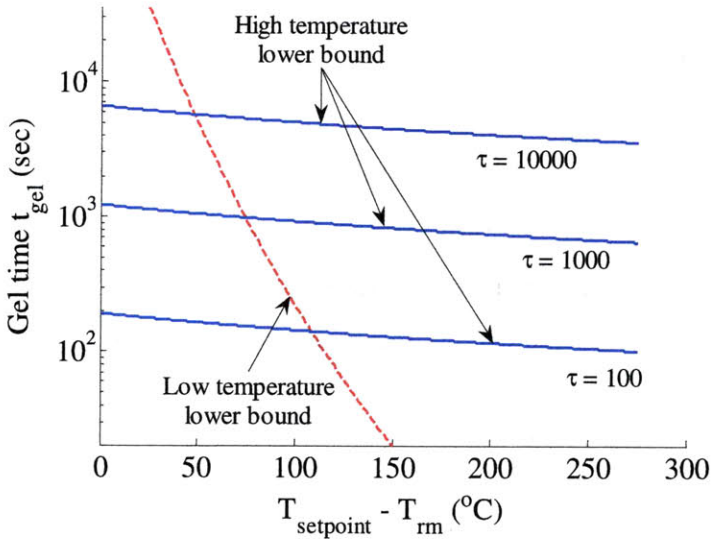

(a)

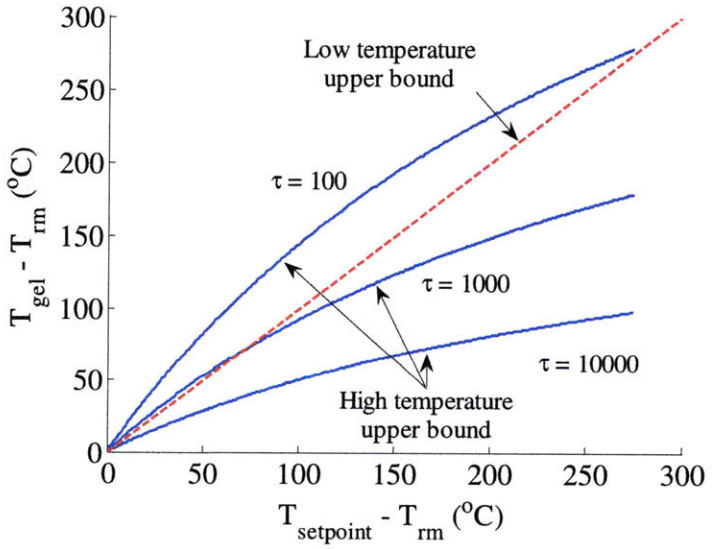

(b)

Figure 4-16: High (solid) and low (dashed) temperature approximations for different τ for (a) gel time and (b) gel temperature.

Figure 4-16, the intersection between high and low temperature approximations pertains to the region where neither approximation is valid, and numerical analysis should be used instead.

Furthermore, it should be noted that in the high temperature regime, reductions in process times are significantly smaller than in the isothermal regime. Consequently, tradeoffs such as thermal degradation and increased geometry variations make operating in the high temperature regime less desirable. Designs should attempt to reduce τ as much as possible, to shift the transition points in Figure 4-16 as far right as possible.

4.4.6 Numerical integration method

When low temperature and high temperature approximations do not apply, the integral in Equation (4.23) can be evaluated numerically. For conditions where the lumped parameter model is no longer sufficient, finite element techniques can be applied. The principle of virtual temperatures is applied to describe a general heat transfer problem [65]. In finite element analysis, the heat conduction equation can be rewritten in the following matrix form:

$$\mathbf{C}\dot{\boldsymbol{\theta}} + \mathbf{K}\boldsymbol{\theta} = \mathbf{Q} \tag{4.30}$$

In Equation (4.30), $\mathbf{C}$ is the heat capacity matrix, $\mathbf{K}$ is the conduction matrix, $\mathbf{Q}$ is the heat generation vector, and $\boldsymbol{\theta}$ is the vector of temperature at each node. The heat capacity and conduction matrices are assumed to be constant through temperature and time, and are determined by material properties, part geometry, and the finite element mesh. The heat generation matrix is also interpolated by the same finite element mesh, but depends on the curing kinetics of the material as well. Previous approximations in Sections 4.4.3, 4.4.4, and 4.4.5 neglect heat generation because it is difficult to analyze analytically. However, finite element analysis can account for these heat generation effects.

To solve for temperature, direct integration can be used to account for the nonlinear heat generation term. An explicit integration method is used, because a smaller time step can be used, when compared with implicit integration, given an arbitrary heat generation vector. For both explicit and implicit integration methods, stability and accuracy must be satisfied. In explicit integration, stability is satisfied if the time step is below $2/\omega_n$, where ω_n is highest mesh frequency. Accuracy is satisfied if the time step is below $\pi/10\omega_{co}$, where ω_{co} is the cutoff

frequency and is set to four times the highest excitation frequency [65]. For arbitrary excitation, ω_{co} is taken to equal ω_n.

Using an implicit integration method, stability is automatically satisfied. Typically, this allows a larger time step to be used to satisfy accuracy because the time step is based on the highest excitation frequency instead of the highest mesh frequency. However, as with explicit integration, an arbitrary excitation frequency requires that the highest mesh frequency be used for accuracy as well. This gives the same equivalent time step as in explicit integration. Because explicit integration is computationally faster for each time step, it is advantageous to use an explicit method since the highest excitation frequency of the heat generation vector is difficult to determine.

In explicit integration, the heat conduction equation is solved for time t as

$$\mathbf{C}\,{}^{t}\dot{\boldsymbol{\theta}} + \mathbf{K}\,{}^{t}\boldsymbol{\theta} = {}^{t}\mathbf{Q} \tag{4.31}$$

where ${}^{t}\mathbf{Q}$ is the heat generation vector at time t, and ${}^{t}\boldsymbol{\theta}$ and ${}^{t}\dot{\boldsymbol{\theta}}$ are the temperature and rate of change of temperature related explicitly by

$${}^{t}\dot{\boldsymbol{\theta}} = \frac{{}^{t+\Delta t}\boldsymbol{\theta} - {}^{t}\boldsymbol{\theta}}{\Delta t} \tag{4.32}$$

The heat generation vector can be discretized in Equation (4.33) by using an interpolation function $\mathbf{H}^{(m)}$, which interpolates and sums the contribution of the m heat generation mesh elements to its nodes. For instructive simplicity, this thesis applies a one-dimensional linear interpolation technique. Additional higher order interpolation functions for one-, two-, and three-dimensions can be found in [65] and can be more computationally efficient for a given accuracy.

$${}^{t}\mathbf{Q} = \sum_{m} \int_{V^{(m)}} \mathbf{H}^{(m)T} (E_{exo}\,{}^{t}\dot{\mathbf{p}}) dV^{(m)} \tag{4.33}$$

The heat generated at each element is a function of the cure rate at that element ${}^{t}\dot{\mathbf{p}}$, scaled by a constant coefficient E_{exo}. This coefficient is the total energy released from forming new bonds at all of the crosslink sites, and given by Equation (4.34). For specific materials, this value can be found empirically as the total exothermic energy per unit volume released during cure.

$$E_{exo} = \int_{t=0}^{\infty} \int_{V^{(m)}} q^B dV^{(m)} dt \tag{4.34}$$

As stated earlier in Equation (4.20), the cure rate is a function of the cure extent and temperature, and can be generically calculated for each element in Equation (4.35),

$$^t\dot{\mathbf{p}} = f(^t\mathbf{p}, \mathbf{H}^{(m)}\, ^t\boldsymbol{\theta}) \tag{4.35}$$

and updated explicitly in

$$^{t+\Delta t}\mathbf{p} = {}^t\mathbf{p} + {}^t\dot{\mathbf{p}}\Delta t \tag{4.36}$$

For each time step, Equations (4.33) through (4.36) are recomputed and used to calculate the new temperature in

$$\mathbf{C}^{t+\Delta t}\boldsymbol{\theta} = \mathbf{C}^t\boldsymbol{\theta} - \left(\mathbf{K}^t\boldsymbol{\theta}\right)\Delta t - \left({}^t\mathbf{Q}\right)\Delta t \tag{4.37}$$

Altogether, this implementation maps temperature and cure extents with time, and can be used with Sections 4.2.1 and 4.3.1 to determine shrinkage and warpage effects once the cure process is completed and cooled back to ambient temperature. The process is shown in Figure 4-17, with a typical four element model shown in Figure 4-18. First, heat generation is computed for each element. Next, the temperature at each node is computed according to the heat equation in Equation (4.37). To determine the temperature at each element, the node temperatures are interpolated. Finally these element temperatures are used to compute the cure extent in each element, and determine if gelation is complete. A typical simulation is shown in Figure 4-19, where the four elements from bottom to top are colored blue, red, green, and black. This color scheme will be used for the remainder of this chapter. Gelation occurs at a constant cure extent, consequently, Figure 4-19 shows that the temperature of the top element lags the bottom element, resulting in both spatial and temporal distributions of gel points throughout the polymer.

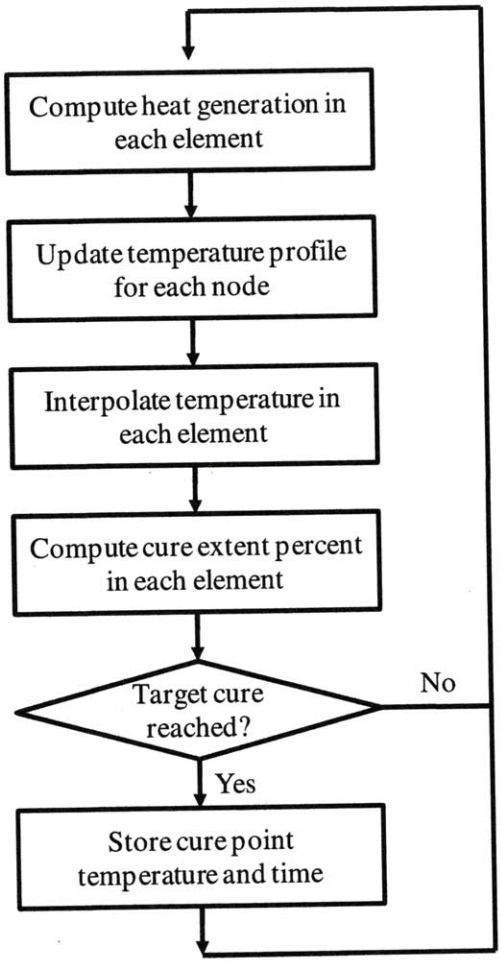

Figure 4-17: Flow chart for cure modeling.

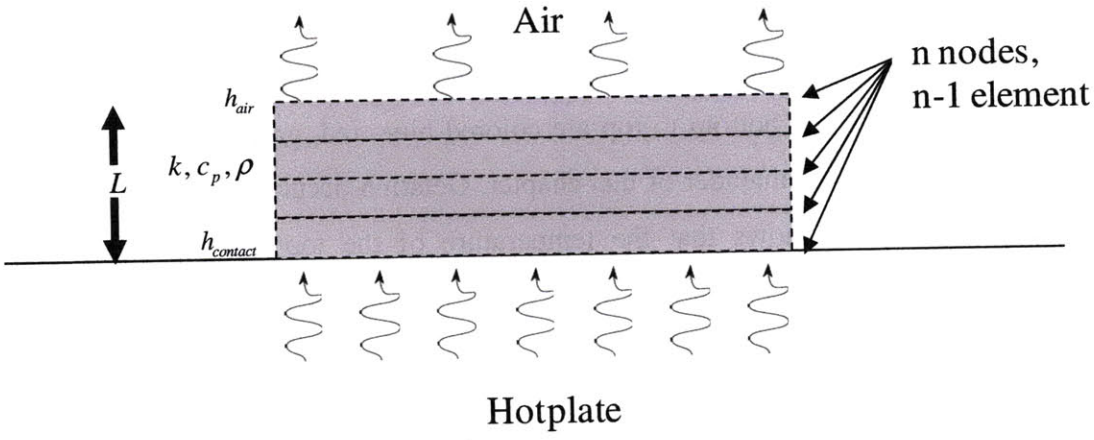

Figure 4-18: One dimensional mathematical model of hotplate heating. The example above has 5 nodes and 4 elements.

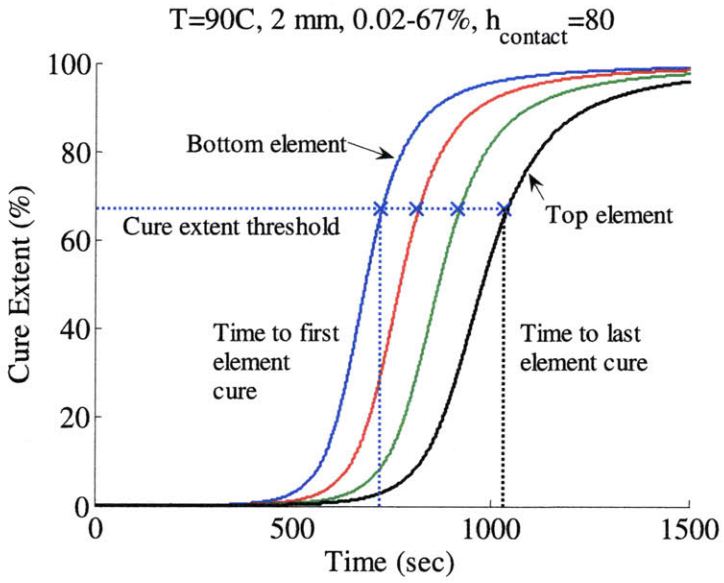

(a)

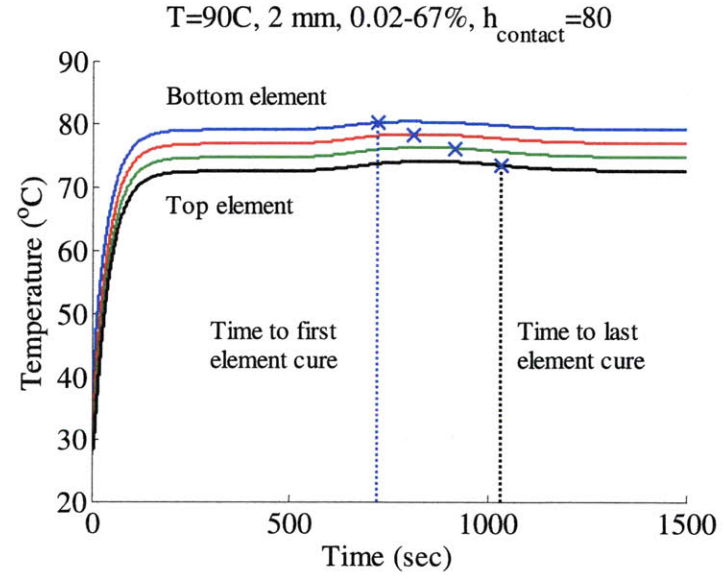

(b)

Figure 4-19: Simulated gel point at each element (a) overlaid with cure extent history and (b) overlaid with temperature history.

4.5 Calibration

4.5.1 Calibration of reaction parameters

Calibration of the parameters for the reaction rate expression in Equation (4.20) was done with a Perkin Elmer Diamond differential scanning calorimeter (DSC), following ASTM procedure E2070-08. Pre-polymer samples of approximately 40 mg were held isothermally for several curing temperatures of interest, while the polymer internally crosslinked. During this reaction, the rate of heat produced was monitored and recorded by the calorimeter. The raw output of the DSC is power versus time, but should be transformed to cure rate versus cure extent to match the form of the reaction rate equation. The transformation and normalization done in Equation (4.38) can be used to determine cure extent.

$$p(t) = \frac{\int_0^t \dot{q}(t)\,dt}{\int_0^\infty \dot{q}(t)\,dt} \tag{4.38}$$

where $q(t)$ is the total exothermic energy released at time t. The denominator is equivalent to q_{total}. Cure extent is subsequently differentiated for cure rate.

$$\dot{p}(t) = \frac{\dot{q}(t)}{\int_0^\infty \dot{q}(t)\,dt} \tag{4.39}$$

Finally, time t is parameterized, and cure rate is a function of cure extent.

Parameters for the curing kinetics equation are found using ASTM procedure E2070-08. By taking the logarithm of both sides of Equation (4.20), a linear equation of the variables k_0, E/R, m, and n can be described by Equation (4.40). These parameters can be computed using a linear least squares minimization technique.

$$\ln(\dot{p}) = \ln(k_0) - \frac{E}{R}\frac{1}{T} + m\ln(p) + n\ln(1-p) \tag{4.40}$$

Inputting raw DSC data into Equation (4.40) inevitably produces erroneous coefficients. The transformation performed by Equations (4.38) and (4.39) biases data points such that they are

more densely clustered at high cure extents or low cure rates, when data is sampled with a constant time step. Without re-sampling, the high reaction rate kinetics is lost in the fit. These are important to the model, since high cure rates occur near gelation. To compensate for this effect, data points are interpolated after they have been transformed to the cure extent-temperature space and prior to fitting. The raw data and solid interpolation mesh are shown in Figure 4-20, and final model mesh overlaid in Figure 4-21. Cure rate is plotted as a function of the dependent variables cure extent and part temperature. The coefficients of Equation (4.40) are found and tabulated in Table 4. for several commonly used mixing ratios of base to curing agent for Sylgard 184. Qualitatively, m decreases as the mixing ratio of base to curing agent increases, since it models the availability of catalyst, which is contained in the curing agent. Also, n is largest for the 10:1 mixing ratio, since it represents the availability of reagents and from Chapter 2 is highest near the stoichiometric ratio.

One caveat with using DSC data in calibration is that only temperatures below 150C can be used. The DSC attempts to keep a finite mass at constant temperature, and at high temperatures the heating transients begin to be comparable with the cure times. This reiterates the importance of modeling high temperature curing kinetics, since empirical data cannot be easily collected.

4.5.2 Calibration of thermal parameters

A simple experimental setup was used to calibrate thermal properties. A 50 by 50 mm aluminum cavity was created to store PDMS while it cured. Several bare 30 AWG K-type thermocouples (Omega P/N 5SRTC-GG-K-30-36) were used to measure temperature in the setup. A single thermocouple was placed inside the aluminum mold to record temperature at the PDMS-aluminum interface, while four additional thermocouples were placed 1, 3, 5, and 7 mm above the bottom of the cavity to record temperature inside the PDMS. This setup is shown in Figure 4-22. These coincide with the centers of a four element model for an 8 mm sample of PDMS. Finally, 8 mm of PDMS was poured into the cavity and allowed to cure. The large thickness is not representative for typical microfluidic devices, but allows us to measure the temperature gradient across the thickness of the sample and calibrate the thermal conductance, specific heat, contact resistance, and convection coefficients.

To decouple heat generation, PDMS can be fully cured before exposing it to the same

Table 4.4: Arrhenius reaction rate coefficients for various mixing ratios.

Coefficients	5:1	10:1	20:1
R [J/mol-K]	8.3140	8.3140	8.3140
k_0 [1/s]	4.8956×10^8	5.8569×10^7	4.6236×10^7
E [J]	6.6084×10^4	6.2696×10^4	6.5671×10^4
m	1.3766	1.1536	0.5210
n	1.3050	1.5891	1.3637

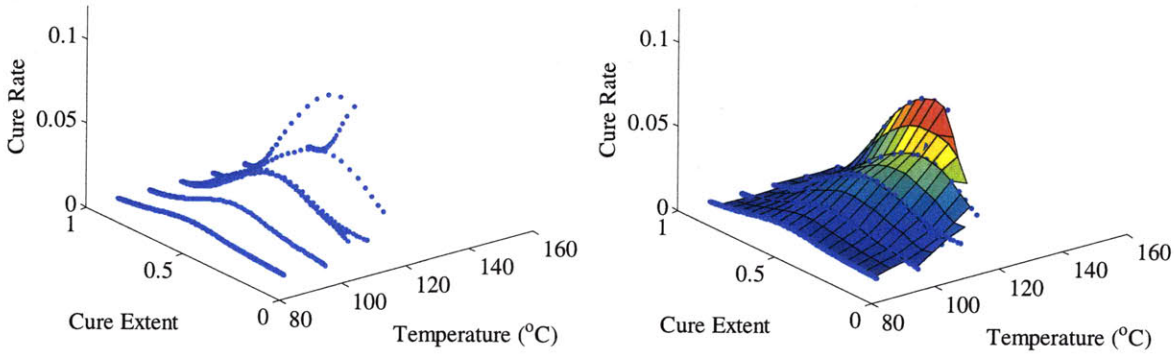

Figure 4-20: DSC data is (a) plotted and (b) interpolated for a 10:1 mixing ratio.

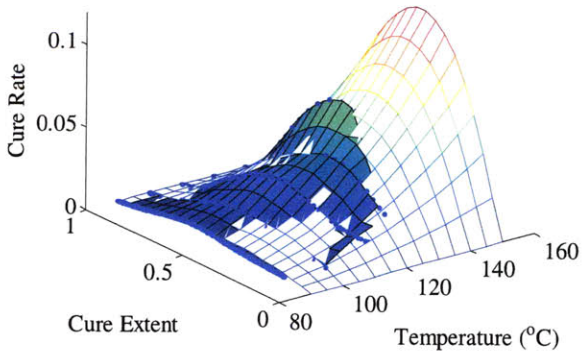

Figure 4-21: Fitting the reaction rate equation for a 10:1 mixing ratio.

temperature cycle. According to Dow Corning, conductivity and specific heat are virtually unchanged between the uncured state and the cured state. This means that the only difference between the temperature profiles taken of uncured PDMS heating and cured PDMS heating is the heat generation term from the uncured PDMS crosslinking. All other thermal behaviors and constants are identical.

For Sylgard 184, thermal conductivity (k) and density (ρ) are given by Dow Corning's spec sheet [19]. Heat capacity (c_p), interfacial heat transfer coefficient ($h_{contact}$), and natural convection (h_{air}) are calibrated by minimizing least squares between experiment and simulation profiles of fully cured PDMS. The final parameters are listed in Table 4., and final profiles shown in Figure 4-23. At each depth, the top profiles plotted includes heat generation due to crosslinking, while the bottom profiles do not. The actual mold temperature from the experiment is shown in brown inside Figure 4-23a, and is used as a boundary condition for the simulation in Figure 4-23b.

4.6 Simulation Results

The numerical model of Section 4.4.6 has been implemented in one-dimension using an explicit integration scheme in MATLAB. Calibration of the rate constants and thermal parameters are described in Section 4.5 and used for the following results. The most important outputs of the model are the temperature and time at arbitrary cure extents, and its spatial distribution. In particular, the spatial distribution of the temperature at gelation can be used with the linear thermal strain Equations (4.1) and (4.11) to calculate dimensionality changes. The cure extent at gelation is approximately 67% for PDMS, and is denoted by an "x" on the time-temperature plots in this section.

4.6.1 Process temperature

In a perfect hotplate, the hotplate steps to the setpoint temperature instantaneously. The PDMS-hotplate contact resistance is set by the calibrated value determined in Table 4.. A 2 mm thick sample is modeled by the four element model shown in Figure 4-18, and the temperature response at the center of each element is plotted in Figure 4-24 according to the color scheme in Figure 4-19. At 90C, gelation occurs near thermal equilibrium and is analogous to the low temperature approximation discussed earlier in Equation (4.3). The total energy produced by

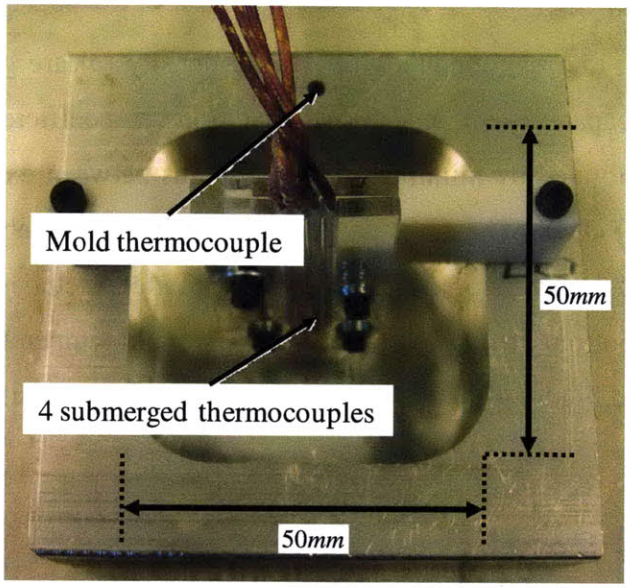

Figure 4-22: Heating profiles are recorded using thermocouples encased in acrylic.

Table 4.5: Material properties of PDMS and its interface.

Parameter	Value
k	0.18 W/m-K
c_p	1540 J/kg-K
ρ	1030 kg/m^3
h_{air}	18 W/m^2-K
$h_{contact}$	80 W/m^2-K

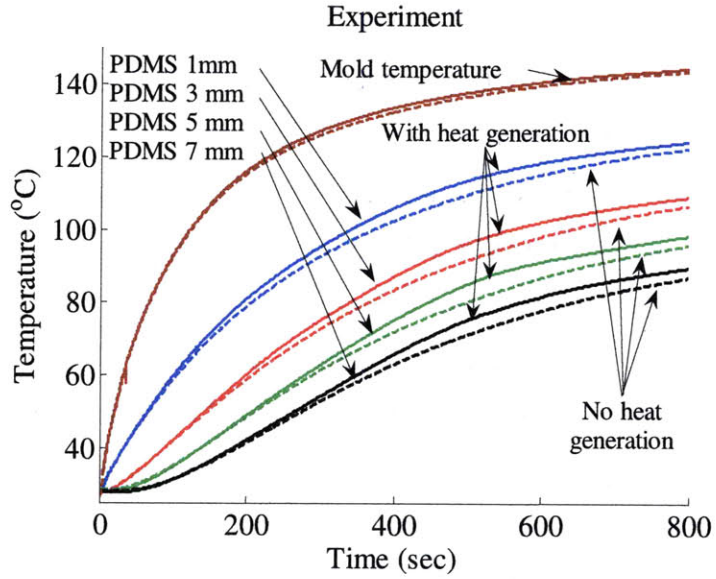

(a)

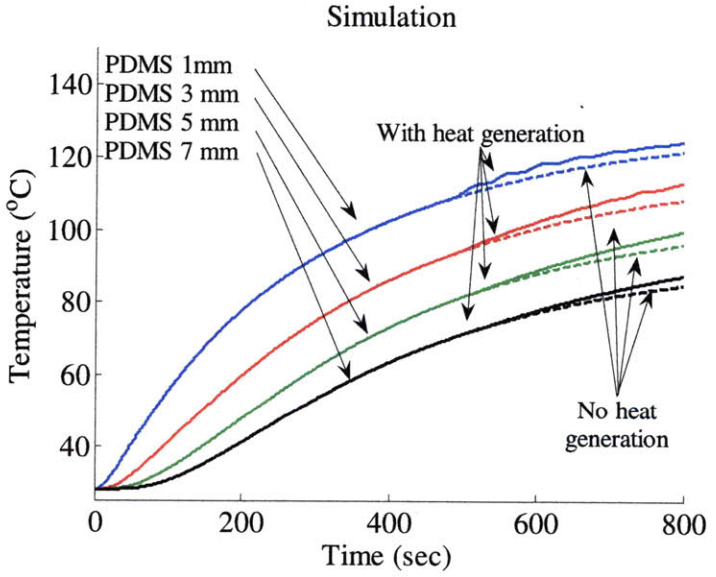

(b)

Figure 4-23: Experiment (left) and simulation (right) of internal temperature histories for temperature cycles during cure and after cure.

crosslinking is distributed throughout the long cure time. Consequently, the gel temperature is only slightly above that of thermal equilibrium. At 120C, the same energy is released in a shorter period, causing a larger overshoot in temperature profile. Because the top surface cures at a slower rate, the gel temperature at the top occurs closer to this peak, and has the effect of creating a smaller gel temperature gradient, compared with 90C. The smaller gradient is directly related to the smaller curvature that results. As the process temperature increases further, gelation begins to occur as the polymer is still increasing in temperature. Consequently, the gel temperature shown in Figure 4-25 continues to increase with process temperature, but at a much slower rate. The average gel temperature is related to shrinkage, and this effect explains the nonlinear dependence on process temperature that is observed in Figure 4-7.

Another interesting result of these simulations is the time to reach gelation. In Chapter 5, it will be shown that a faster cure process can be designed by increasing temperature after the entire part has reached gelation. Consequently, this time is determined by the gel time of the slowest element. In the case of hotplate curing, the slowest element is the top element. At 90C, the gel times for the top and bottom elements are different by 312 sec, while at 180C they are only different by 28 sec. Figure 4-25 shows the gel time and gel temperature dependence on the hotplate setpoint temperature. As this process temperature increases, the gel point clusters closer together. Consequently, the bottom element spends less time waiting for the top element to gel. There are two main problems with curing at too high a temperature. First, thermal degradation begins to occur in PDMS around 150C, and causes the part to lose transparency and turn yellow. Second, the process becomes more sensitive to the gel point. Small changes to the gel point at thermal equilibrium have little effect on the gel temperature. However, small changes to the gel point as the polymer is heating up will depend on the slope of the ramp, which increases with process temperature. Consequently, as was shown in Figure 4-11, the variance increases linearly with process temperature above 150C.

4.6.2 Part thickness

Another important parameter is the thickness of the part. Thick layers of PDMS are commonly used to form the substrate, while thin layers are used to form membranes. In the case of Thorsen's large scale integrated valve system, a 5 mm thick layer of PDMS is used for the control channels, while a 30 μm thin layer is used for the flow channels [21]. The thickness of

the part can affect the thermal response of the system and the final gel point. Figure 4-26 simulates the impact of thickness on the gel point, while Figure 4-27 summarizes the effect on gel times and gel temperatures. Since thicker parts experience smaller shrinkage, these plots should be taken into consideration when designing features on thin and thick parts that need to mate.

4.6.3 Heating mechanism

In most cases, hotplates have finite thermal mass and non-negligible heating times. Furthermore, the controlled temperature at the hotplate may be a significant distance from the PDMS-hotplate interface. These delays can be lumped into the heat transfer coefficient, $h_{contact}$, and examined in Figure 4-28. Figure 4-29 summarizes the effect on gel times and gel temperatures. By keeping temperature constant, as $h_{contact}$ decreases, the polymer temperature decreases and this is qualitatively the same effect of decreasing process temperature.

The control systems in the hotplate themselves may also add some additional dynamics or delays to the system. In Figure 4-30, it is assumed that the control system is overdamped and that it can be approximated by a first order response with a time constant of τ_{ctrl}. Figure 4-31 summarizes the effect on gel times and gel temperatures. The effect is similar to the real hotplate condition described above, except that the overall temperature does not decrease. As with increasing process temperature, increasing τ_{ctrl} causes the gel point to move away from thermal equilibrium, and the gel temperature to decrease relative to the process temperature.

4.6.4 Gel point variation

The gel point is taken to occur at a cure extent of 67%. From Equation (2.9), the gelation point is dependent on the average functionality of the polymer. For average functionalities between 3 and 6, the cure extent at gelation is between 67% and 33% and is plotted in Figure 4-32. Figure 4-33 summarizes the effect on gel times and gel temperatures, which are not significantly different when the cure extent at gelation is within this range. This can be partially understood by plotting the left integrand of Equation (4.23). For any values of m and n, the integrand approaches infinity for cure extent p close to 0 and 1. Consequently, when p_0 is small and p_f is close to 0.5, small change in p_f have little impact on the integral. The integrand has this form, since reaction rates are largest when p is near 0.5. Because gelation tends to happen in this

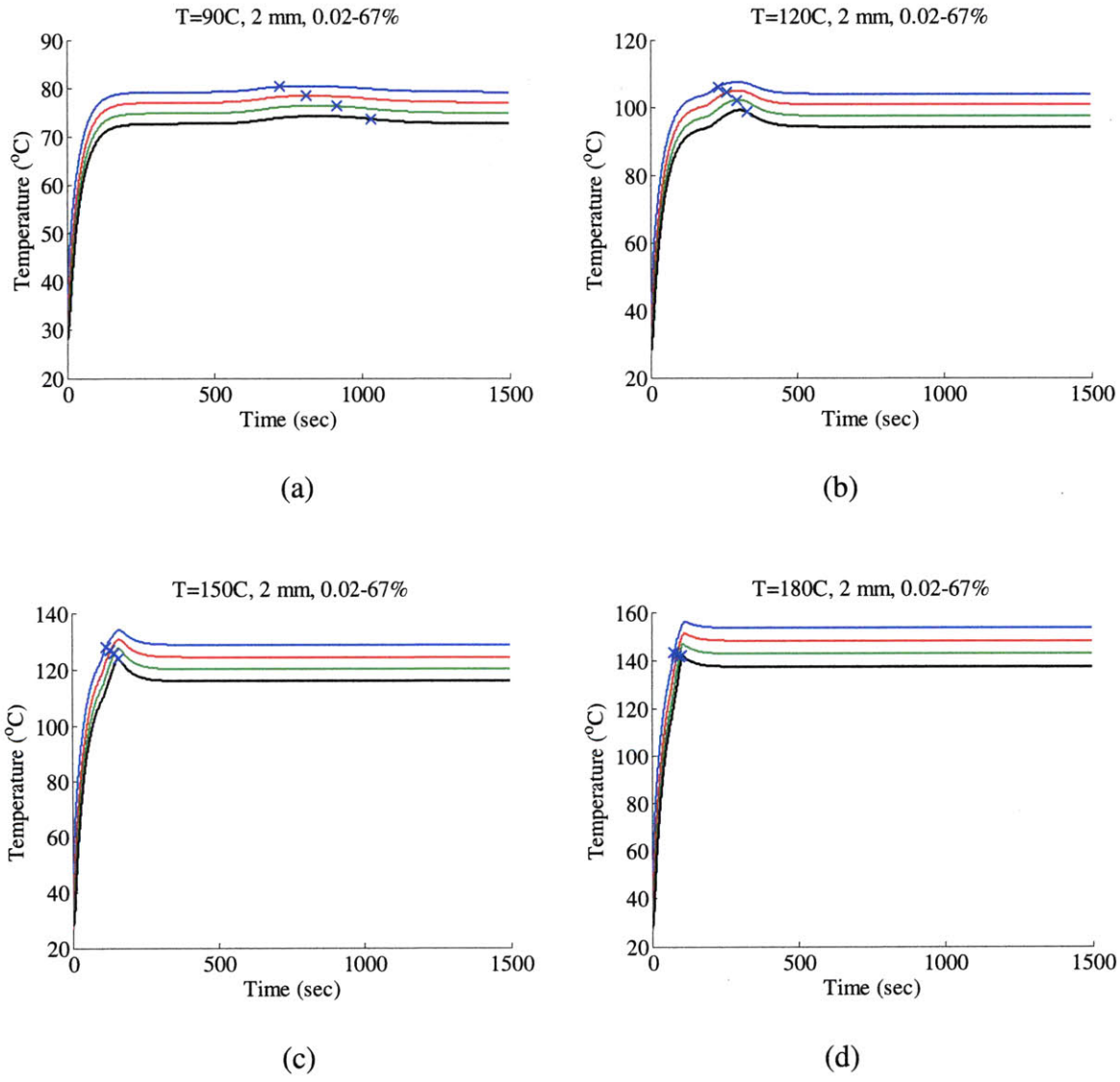

Figure 4-24: Simulated impact of temperature on gel point.

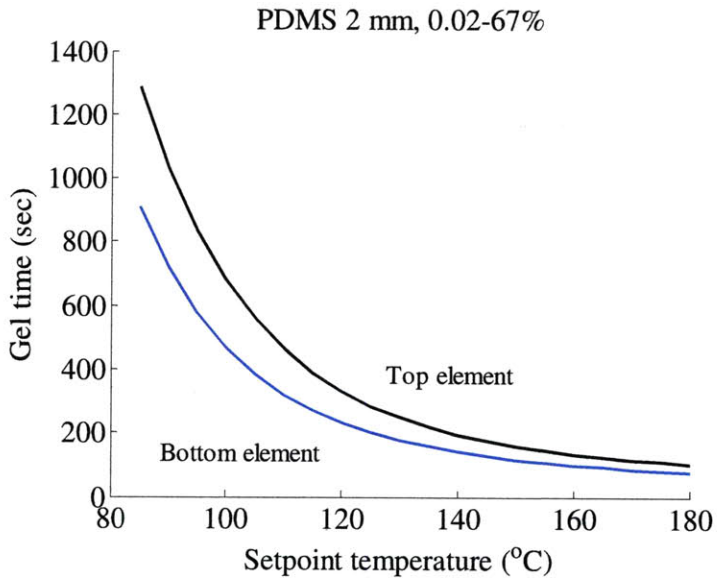

(a)

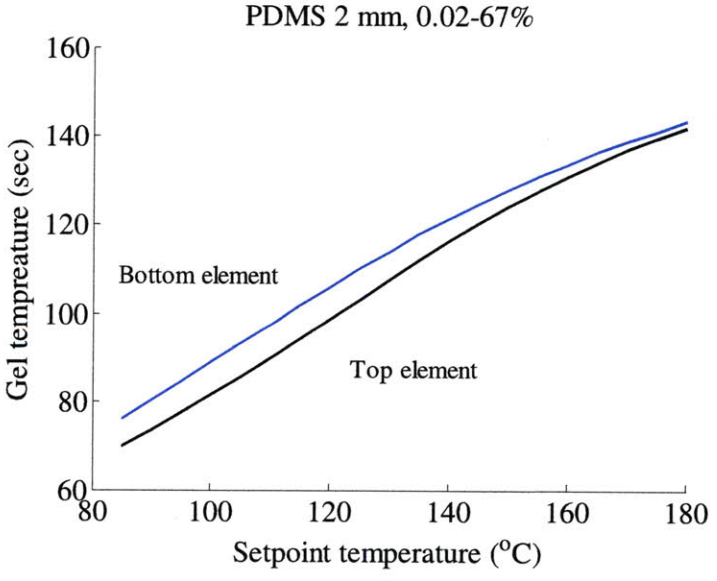

(b)

Figure 4-25: Simulated impact of temperature on (a) gel time and (b) gel temperature.

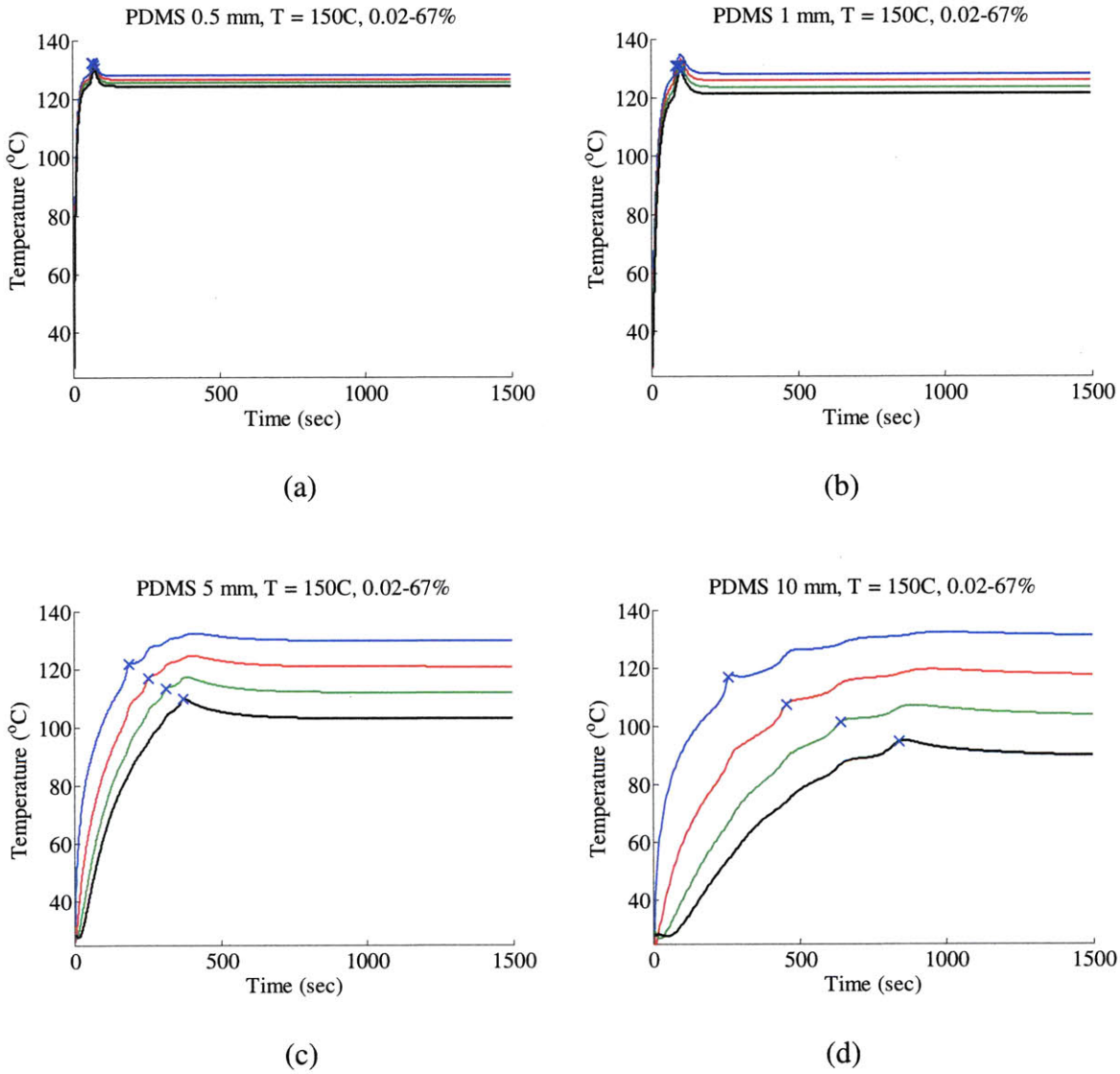

Figure 4-26: Simulated impact of thickness on gel point.

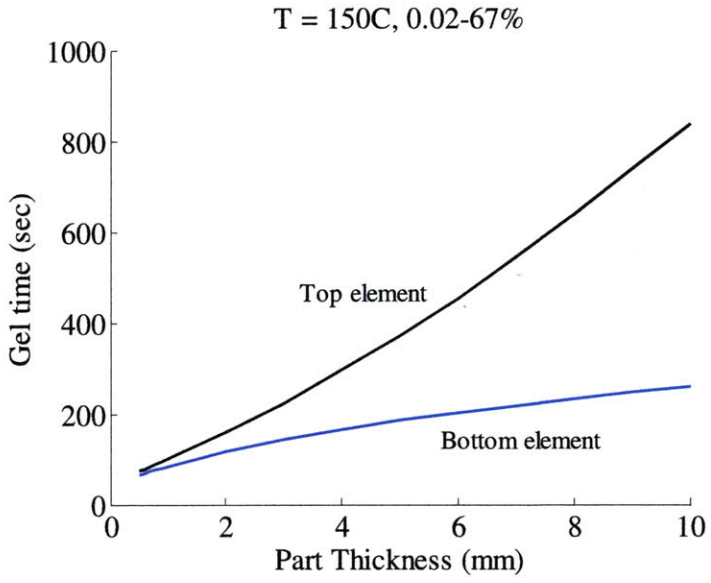

(a)

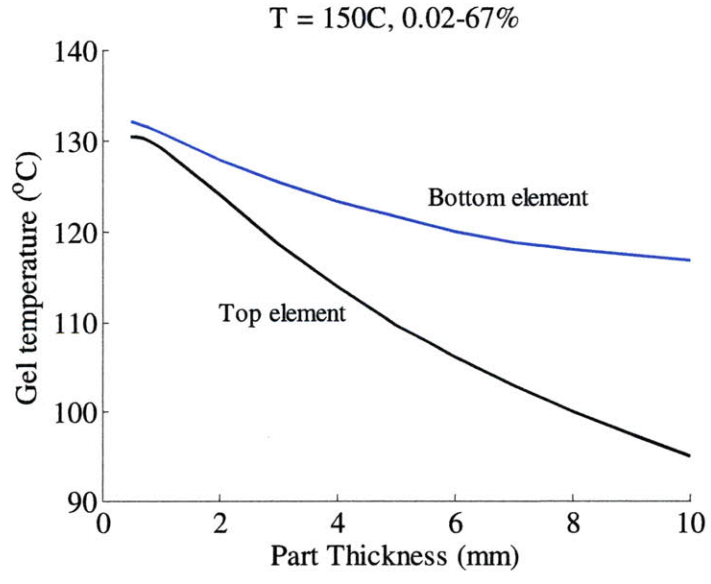

(b)

Figure 4-27: Simulated impact of thickness on (a) gel time and (b) gel temperature.

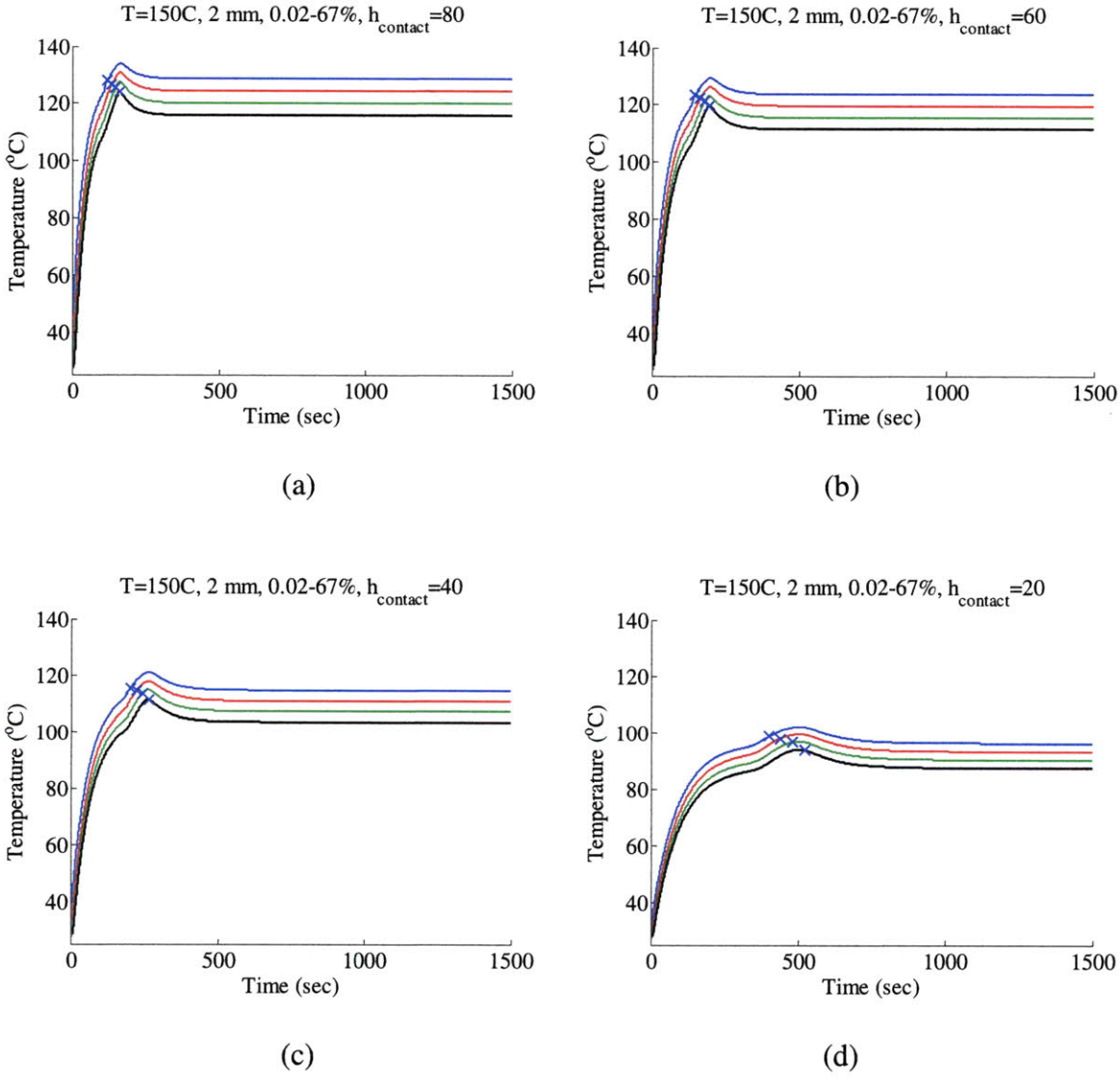

Figure 4-28: Simulated impact of hotplate contact resistance on gel point.

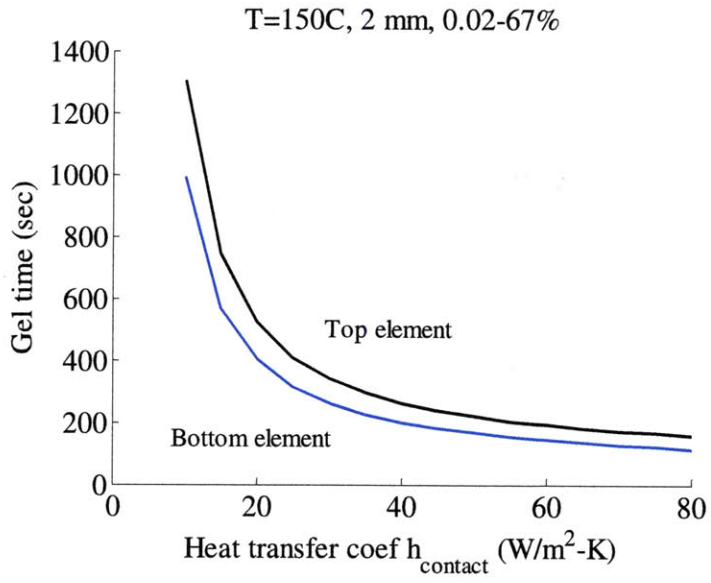

(a)

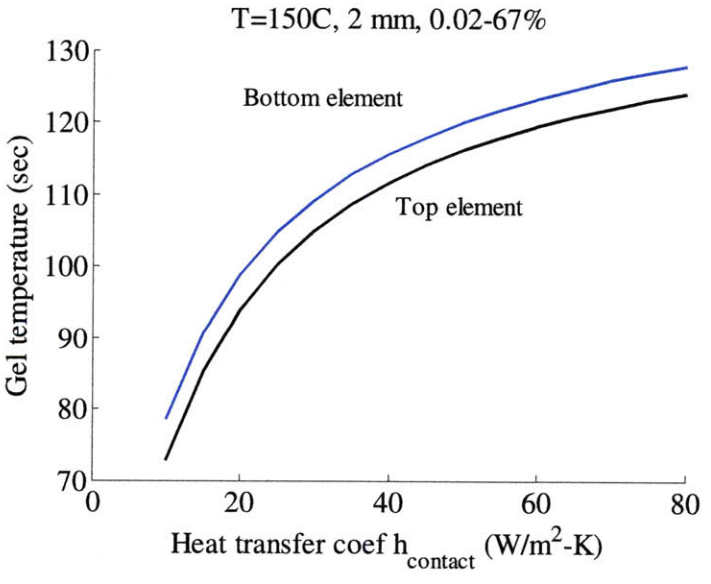

(b)

Figure 4-29: Simulated impact of hotplate contact resistance on (a) gel time and (b) gel temperature.

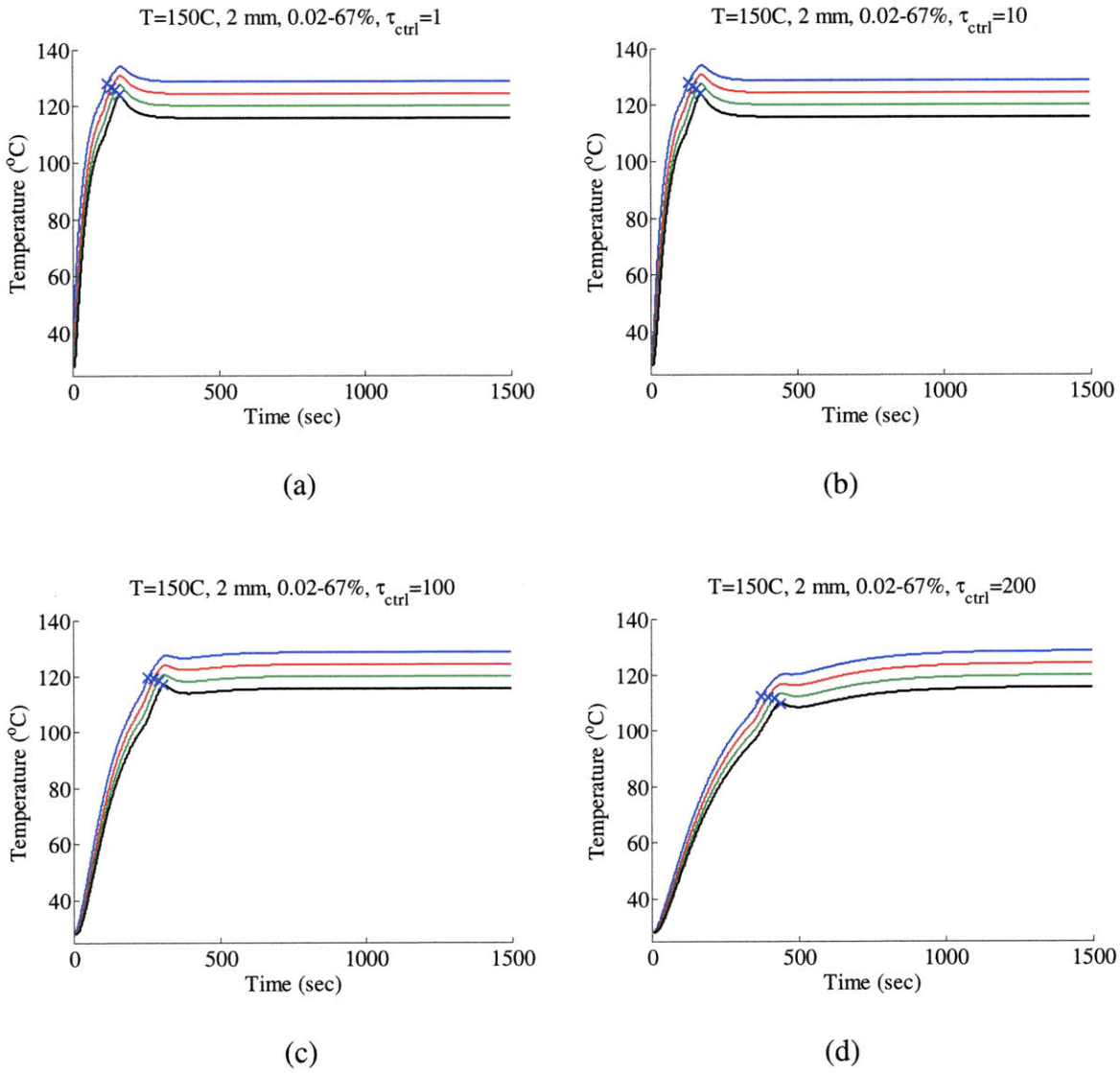

Figure 4-30: Simulated impact of non-perfect hotplate on gel point.

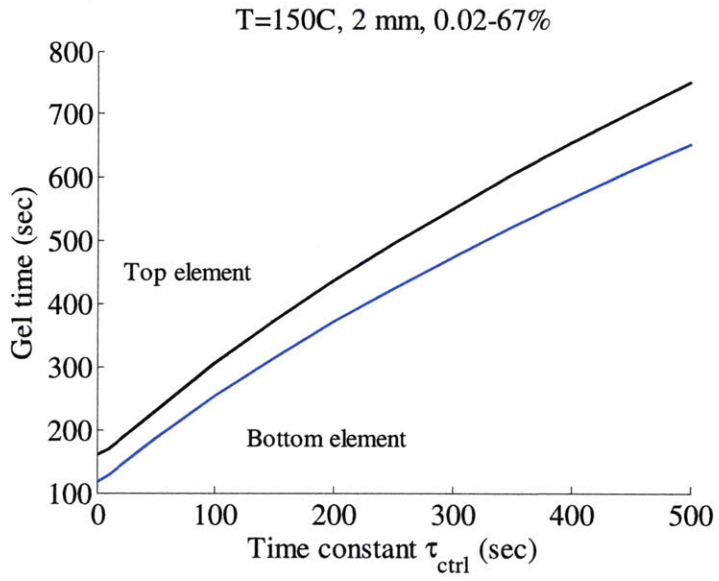

(a)

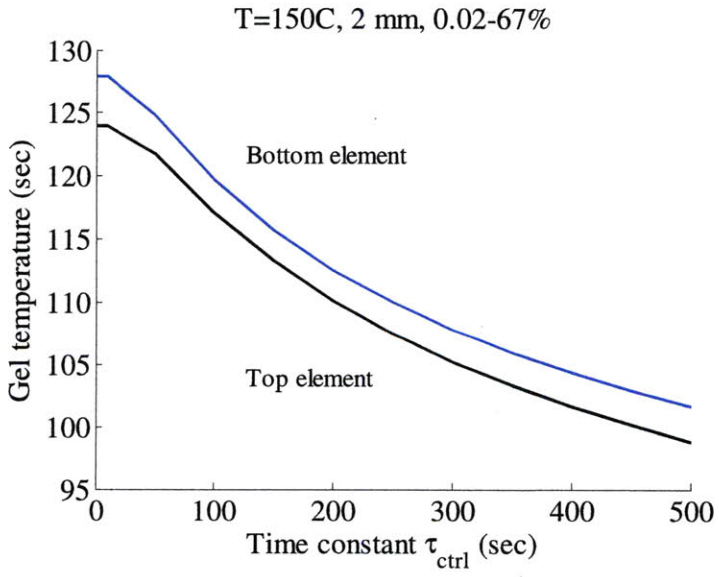

(b)

Figure 4-31: Simulated impact of non-perfect hotplate on (a) gel time and (b) gel temperature.

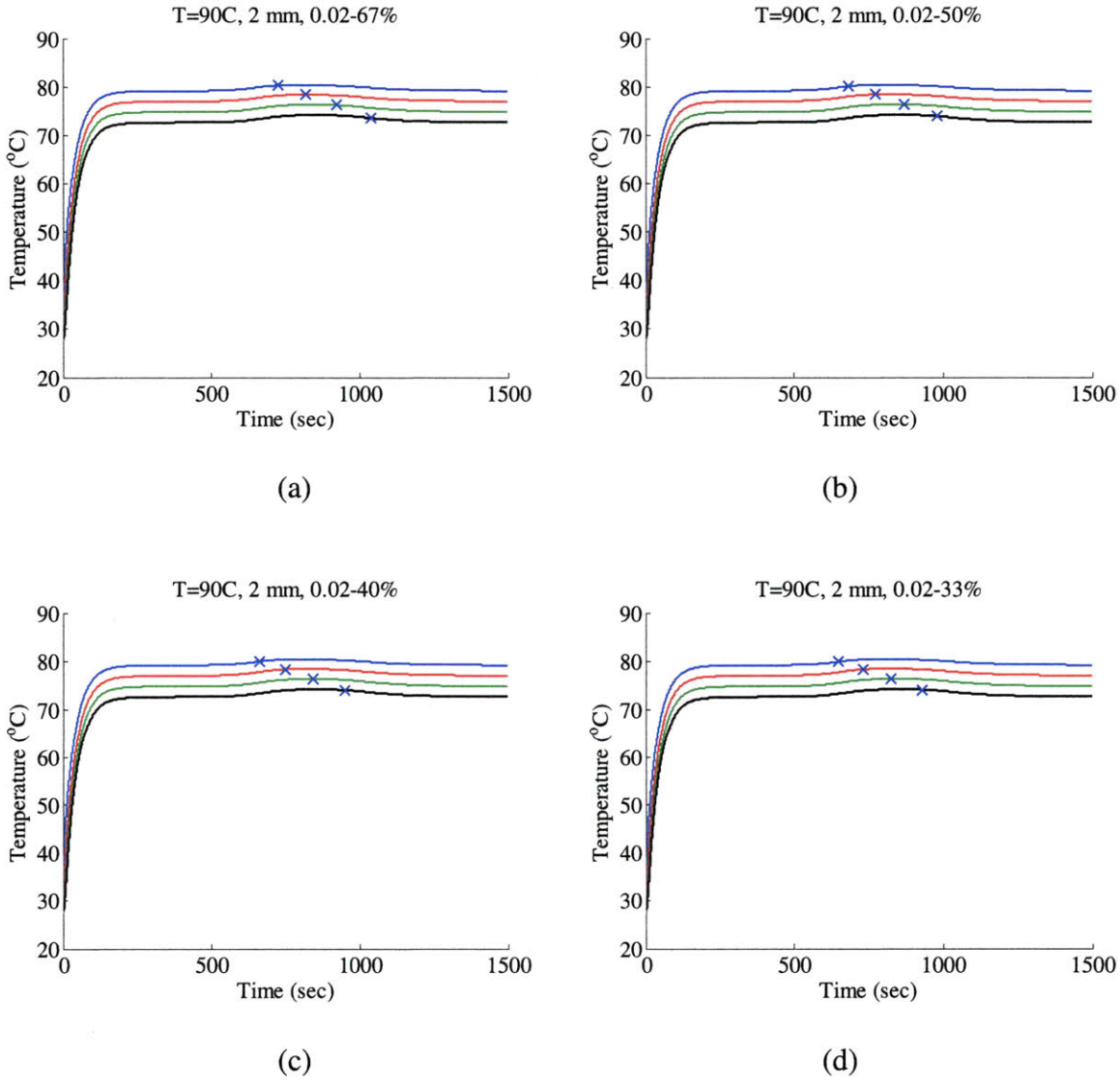

Figure 4-32: Simulated impact of final cure extent on gel point.

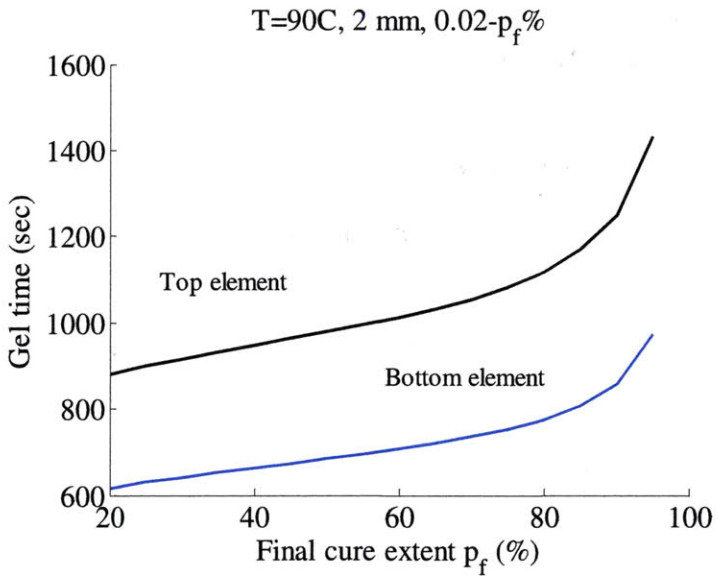

(a)

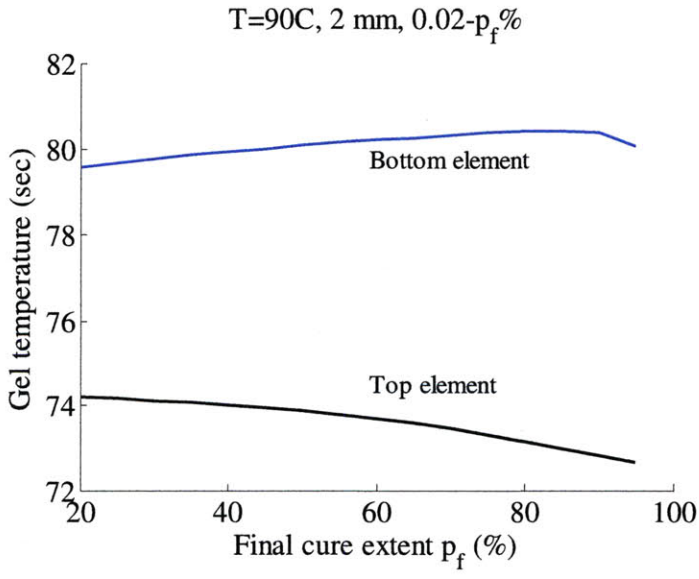

(b)

Figure 4-33: Simulated impact of final cure extent on (a) gel time and (b) gel temperature.

same range, the gel time and temperature are insensitive. This suggests that engineering the polymer to larger average functionality will not significantly reduce the gel time, and that the cure process is tolerant to potential variability in the average functionality of the pre-polymer.

4.7 Experimental Results

4.7.1 Thickness and the isothermal approximation

As a simple experiment, two different thickness substrates are cured, and the time required to reach the same cure extent is examined for different process temperatures. Thinner materials should be more closely approximated by the isothermal approximation. As shown in Chapter 2, cure extent is monotonically related to modulus. Also, by Equation (3.1), durometer measurements are monotonically related to modulus. Consequently a durometer can be used to measure the relative cure extent of samples cured at different temperatures and thicknesses.

In these measurements, a Longacre Racing Tire Hardness Tester was used, shown in Figure 3-2. Two test conditions of different thicknesses, 2.7 mm and 8 mm, were cured at hotplate setpoints of 65C, 75C, and 85C. Because the polymer was initially viscous, measurements were only taken once the sample appeared to pass gelation, and was capable of supporting indentation by the durometer. Durometer Shore A readings were taken from both test thicknesses, and plotted against time in Figure 4-34. The thinner 2.7 mm part reached a higher Shore A hardness earlier, since its time constant τ is nearly 9 times faster than the 8 mm part. More importantly, this faster time constant has the effect of putting the 2.7 mm part closer to the isothermal regime at test temperatures. Section 4.4.4 mentioned that in the isothermal regime, every 10C should have the effect of decreasing cure time at any arbitrary cure extent by a factor of approximately two. In Figure 4-34a, the 2.7 mm sample shows this relationship for almost all Shore A hardness. In Figure 4-34b, the 8 mm sample shows this relationship between 65C and 75C, but shows a much smaller reduction from 75C to 85C. The speed of cure is comparable the speed of the heating mechanism and the isothermal approximation is no longer sufficient. When the isothermal approximation is overlaid in Figure 4-35 for Shore A hardness between 40 and 50, this exact phenomenon is observed.

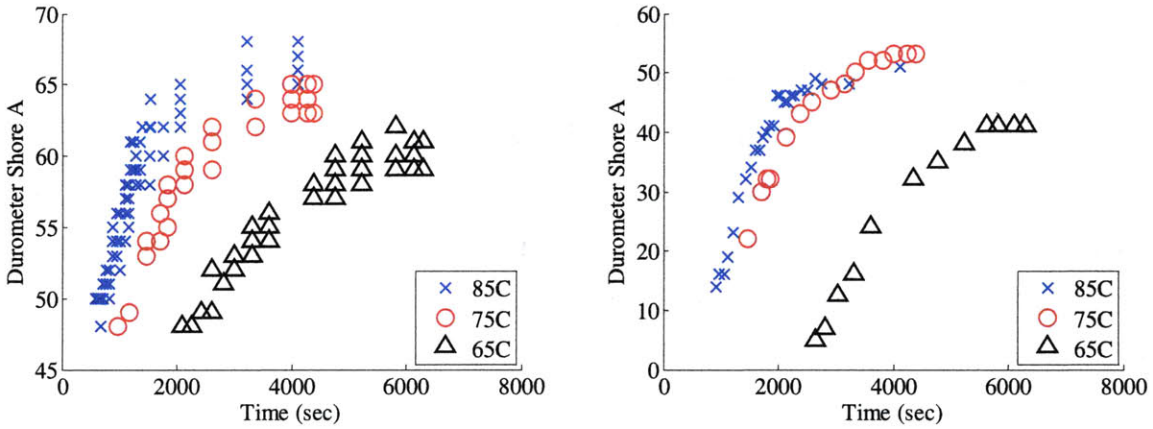

Figure 4-34: Modulus history for (a) 2.7 mm and (b) 8 mm parts.

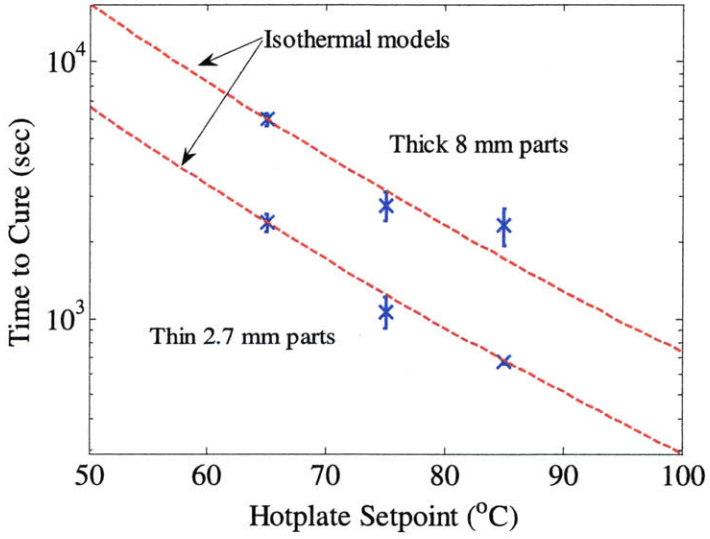

Figure 4-35: Cure time plotted against setpoint temperature for 2.7 mm ("x") and 8 mm ("o") samples to reach a Shore A hardness of 40-50.

4.7.2 Shrinkage and curvature

Numerical models and the experimental shrinkage and curvature measurements from Sections 4.2.3 and 4.3.3 can be used to verify that the gel temperature is indeed the primary factor in determining shrinkage and warpage in a part.

The shrinkage measurements are shown in Figure 4-36 with the isothermal approximation and numerical simulation overlaid. The measurements and numerical results both show that gel temperature is linear to process temperature at low process temperatures. This is consistent with the linear model in Equation (4.8). For high process temperatures, shrinkage is smaller than that predicted by the isothermal model, because the gel time decreases and gel temperature decreases to below the temperature at thermal equilibrium. As mentioned in Section 4.4.5, the isothermal approximation provides an upper bound for the gel temperature, consequently it also provides an upper bound for the shrinkage that is observed.

The curvature measurements are shown in Figure 4-37 with the isothermal approximation and numerical simulation overlaid. The measurements and numerical results both show that gel temperature is linear to process temperature, when cured at low process temperatures. This is consistent with the linear model shown in Equation (4.16). Again, the isothermal approximation provides an upper bound for the gel temperature. Consequently, it also provides an upper bound for the curvature that is observed. As the gel time approaches the transient time constant τ of the thermal system, the bottom surface cures faster than the top surface. The bottom surface cures fast enough such that gelation occurs long before thermal equilibrium is reached. On the other hand, the top surface has more time to cure, and is closer to its temperature at thermal equilibrium. Consequently, this rate difference causes the gel temperature of the two surfaces to be closer together, and the curvature to decrease and show a local minimum for mid range process temperatures. Finally at high process temperatures, both top and bottom surfaces cure quickly and long before thermal equilibrium is reached. Both experience temperature increases that are approximately linear with time, so the temperature difference again diverges and causes the curvature to increase.

4.8 Summary

When shrinkage is linear with process temperature, it can be designed into the part, or

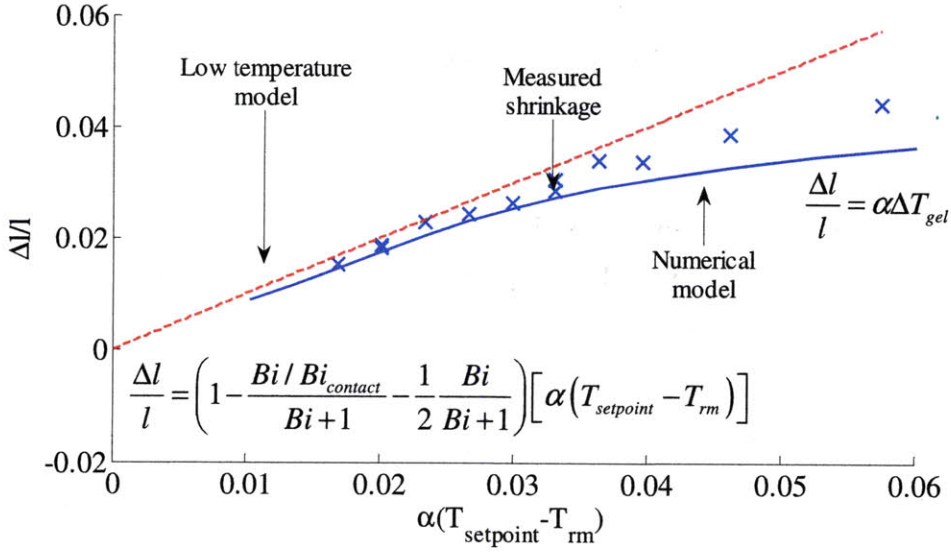

Figure 4-36: Numerical model for lateral shrinkage and experimental data.

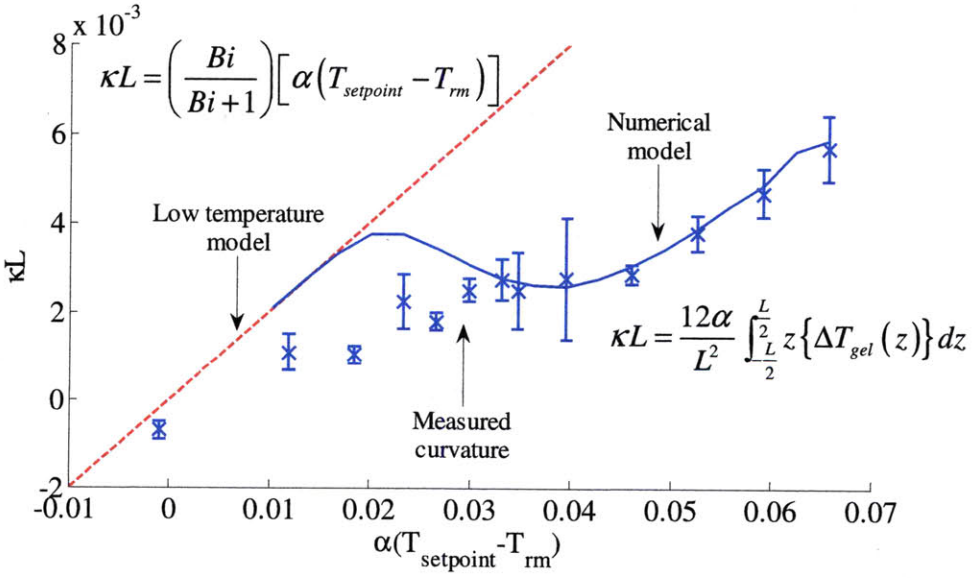

Figure 4-37: Numerical model for curvature and experimental data.

easily compensated for with the process. Equations (4.8) and (4.16) make up the simplified linear models for low temperature cures of PDMS. Equations (4.6) and (4.7) show that thin and thermally conductive parts produce small Biot numbers much less than one. Consequently, these parts produce a linear shrinkage slope near one and a curvature slope near *Bi*. However, when shrinkage is no longer linear at high temperatures, additional analysis is required to determine the gel temperature. Linear models for shrinkage and curvature are initially proposed, which are applicable for low temperatures cures and are functions of the Biot number. For general cure temperature distributions, shrinkage and warpage are described as a function of $\Delta T_{gel}(z)$.

Determination of $\Delta T_{gel}(z)$ is achieved by modeling the cure extent of the crosslinking process, and finding the time of gelation. In this chapter, several different methods are demonstrated to calculate gel time and then gel temperature. These values are important in determining the actual shape change that the part will undergo. These methods vary in their complexity, and should be applied in order of their complexity. Figure 4-38 gives a flow chart for the approximations and solutions that should be applied depending on the assumptions that can be made. First, if the Biot number is large but the time constant is small, the low temperature approximation shown in Sections 4.2.1 and 4.3.1 is applicable. Second, if the Biot number is small and the time constant is small, the low temperature lumped parameter model in Section 4.4.4 should be applied. Third, if the Biot number is small and time constant is large, the high temperature lumped parameter model in Section 4.4.5 should be applied. Fourth, if the Biot number is small and the time constant is comparable to the isothermal cure time, the lumped parameter model in Section 4.4.3 should be solved numerically. Finally, if none of these conditions apply, fully coupled finite element analysis should be used.

All of these methods are capable of determining gel temperature and gel time. When used with shrinkage and warpage models in Sections 4.2.1 and 4.3.1, these can be used to predict shrinkage and curvature dependence on the process temperature. This is useful as a process design tool, when shrinkage and curvature specs are given and the proper process temperature needs to be determined. Furthermore, once a process temperature has been found, simple analysis can determine the operating regime of the process, and give insight into potential process time improvements with incremental process temperature increases. The largest process time reductions can be gained by the same incremental temperature increase, when the process is in the low temperature isothermal regime.

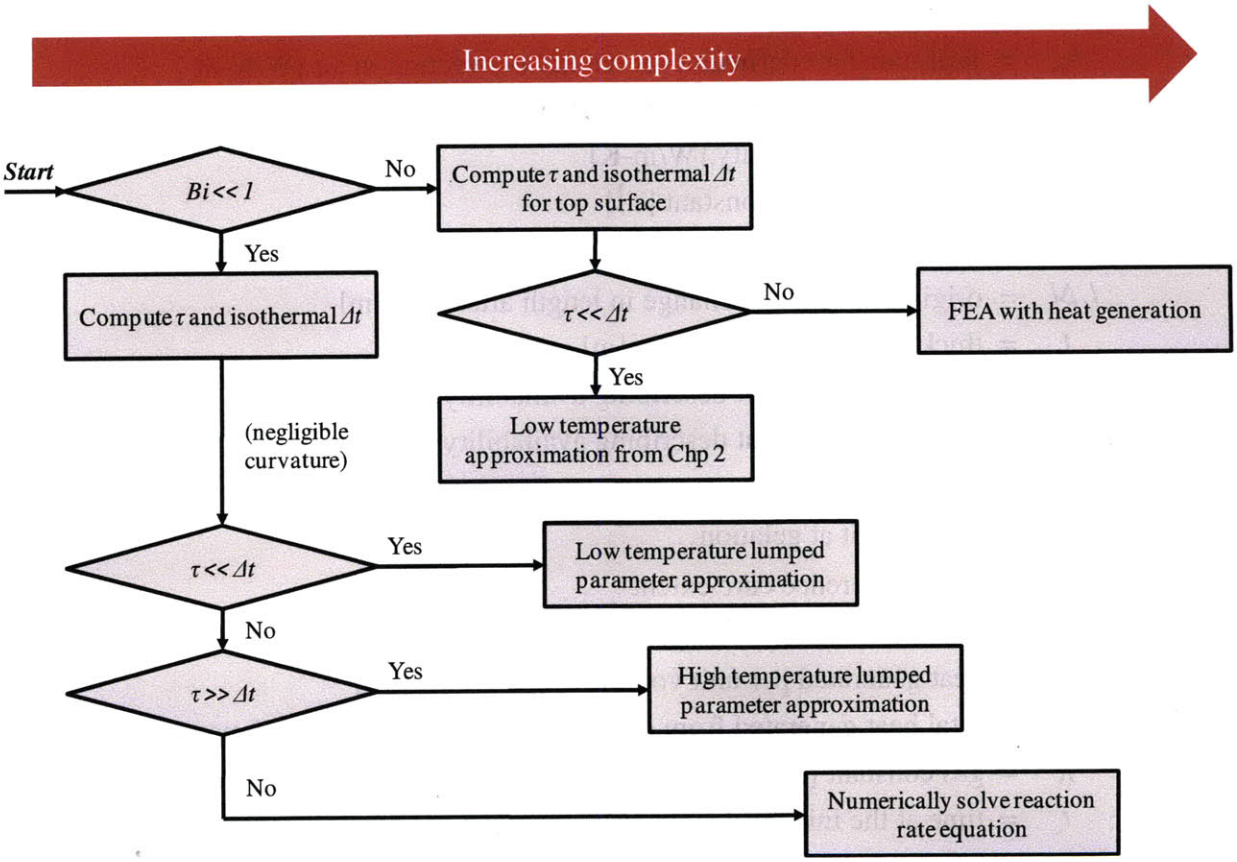

Figure 4-38: Flow chart for determining cure time and temperature.

Nomenclature

$Bi, Bi_{contact}$ = dimensionless Biot numbers

c_p = specific heat of the material [J/kg-K]

$d_{\max}$ = vertical bowed distance of bottom center of PDMS sample [m]

E = activation energy [J]

f_{avg} = average functional ends per strand in the pre-polymer

$h_{contact}$ = heat transfer coefficient for the hotplate-sample interface [W/K-m^2]

h_{air} = heat transfer coefficient for natural convection in air [W/K-m^2]

h_{char} = characteristic heat transfer coefficient [W/K-m^2]

k = thermal conductivity [W/m-K]

k_0 = pre-exponential constant [s^{-1}]

$k(T)$ = Arrhenius dependence on temperature [s^{-1}]

$l, \Delta l$ = original length and change in length after cure [m]

L = thickness of PDMS sample [m]

m = empirical exponent describing availability of catalyst

n = empirical exponent describing availability of reagents

p = cure extent

p_{gel} = cure extent at gelation

p_o = initial reference cure extent

p_f = final reference cure extent

q = heat generated per unit volume of material [J/m^3]

q_{total} = total heat generated from crosslinking per unit volume of material [J]

R = gas constant [J/mol-K]

t_o = time at the initial reference cure extent, typically zero [s]

t_f = time at the final reference cure extent [s]

t_{gel} = time to reach gelation for a given cure process [s]

Δt = time from t_o to t_f [s]

$\Delta t_{T_1}, \Delta t_{T_2}$ = time from t_o to t_f for cures performed at different reference temperatures [s]

T = temperature of the material [K]

T_{rm} = ambient room temperature [K]

T_{gel} = temperature sample gels at [K]

ΔT_{gel} = temperature above room temperature sample gels at [K]

ΔT_{total} = cure temperature difference between top and bottom surfaces of sample [K]

T_1, T_2 = initial and final reference temperatures [K]

$\Delta T_1, \Delta T_2$ = temperature above room temperature of reference temperatures [K]

$T_{setpoint}$ = hotplate setpoint temperature [K]

$\Delta T_{setpoint}$ = temperature above room temperature of the hotplate setpoint temperature [K]

w = width of PDMS sample [m]

z = vertical distance from center of PDMS sample [m]

α = thermal expansion coefficient

ε = shrinkage

κ = curvature [m^{-1}]

ρ = density [kg/m^3]

τ = time constant characterizing the heating response of the material [s]

τ_{ctrl} = time constant characterizing the heating response of the heater [s]

$\mathbf{C}$ = heat capacity matrix [J/m^3-K]

$\mathbf{H}$ = interpolation matrix

$\mathbf{K}$ = conduction matrix [W/m^3-K]

$\mathbf{Q}$ = heat generation vector [W/m^3]

$\boldsymbol{\theta}$ = temperature vector [K]

CHAPTER

5

GELATION AND CURE SCHEDULING FOR PROCESS TIME REDUCTION

As described in Chapter 2, gelation occurs when the macromolecule is formed. As a macromolecule, the polymer no longer flows freely as a liquid and instead conforms to the shape of its mold. Past gelation, additional crosslinks continue to stiffen the polymer matrix, but its unstrained shape is effectively locked at the gel point. Consequently, process temperature can be increased directly after gelation to accelerate the remainder of the cure. In this chapter, a two temperature cure process is proposed to control the part temperature at gelation. With this strategy, the total cure time can be decreased by a factor of five times, while maintaining the same shrinkage achieved with a single low temperature cure.

5.1 Background

Traditionally, PDMS is cured to a point where it is "firm to touch" [32]. What this means, is that PDMS is cured until it behaves as an elastomer, and recovers completely from any perturbations to its surface. In our experience, this occurs when Young's modulus is above 75% of its final modulus value, which corresponds to a cure extent above 90% by relationships found in Chapter 2. However, in practice, most researchers are more conservative in their experiments, and choose to cure to a much higher cure extent. One reason is because of an aging phenomenon, where parts continue to stiffen after the cure process is complete [14, 35]. This can be problematic, because stiffness will drift from its originally designed value and affect the performance of the part. Consequently, cures are often performed to cure extents that are very

close to 100%. For an isothermal cure at room temperature, Dow Corning recommends a cure time of 48 hrs for Sylgard 184, which computes to a final cure extent of 99.9% when the initial cure extent is 0.02%. The equivalent time to reach the gelation point at 67% is under 9 hrs. Consequently, curing from gelation to the final cure state currently consumes more than 80% of the total process time.

5.2 Process Time Improvements

5.2.1 Cure time reduction in the isothermal regime

PDMS is typically cured using a single temperature cure process, shown in Figure 5-1. The gel time is denoted t_{gel}, while the total process time is denoted t_1 for a process temperature of T_1. To minimize aging effects, the final cure extent p_f at time t_1 is chosen near 100%. However, as p_f approaches 100%, the reaction slows and t_1 increases dramatically, as shown in Figure 5-2. Consequently, t_1 is typically much larger than t_{gel}.

Alternatively, a two temperature cure process can be used to decrease process time. Since shrinkage and curvature are dependent on the part temperature at gelation, the process temperature can be increased after gelation from T_1 to an arbitrarily large value T_2, as shown in Figure 5-3. Ideally T_2 is selected large enough such that the remainder of the cure occurs nearly instantaneously, or in a time much smaller than the gel time t_{gel}. Consequently, in the two temperature cure process, the total process time is approximately equal to t_{gel}.

By using this two temperature process time strategy, process time can be reduced by a factor of t_1/t_{gel}. Taking temperature to be constant over time, the Arrhenius temperature terms disappear from Equation (4.23) and result in Equation (5.1).

$$\frac{t_1}{t_{gel}} = \frac{\int_{p_0}^{p_f} \frac{1}{p^m(1-p)^n}\,dp}{\int_{p_0}^{p_{gel}} \frac{1}{p^m(1-p)^n}\,dp} \tag{5.1}$$

For an initial cure extent of 0.02%, the potential process time reduction is plotted in Figure 5-4 for a gelation point of 67%. Dow Corning's recommended cure times correspond to a cure extent of approximately 99.9%, which should yield a process time reduction of about five

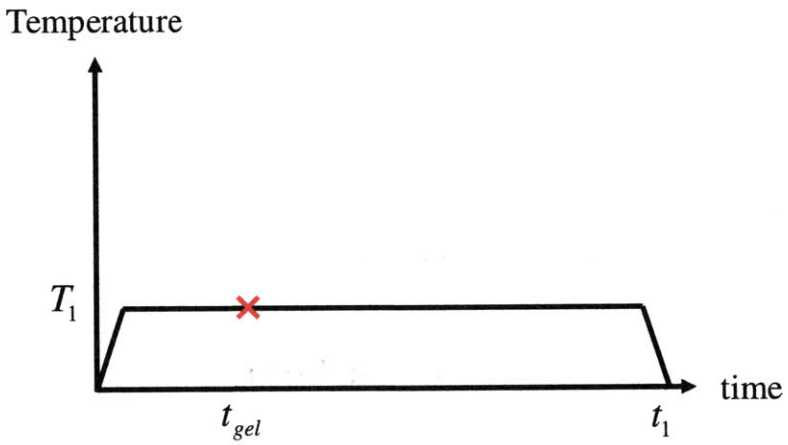

Figure 5-1: Standard single temperature cure process.

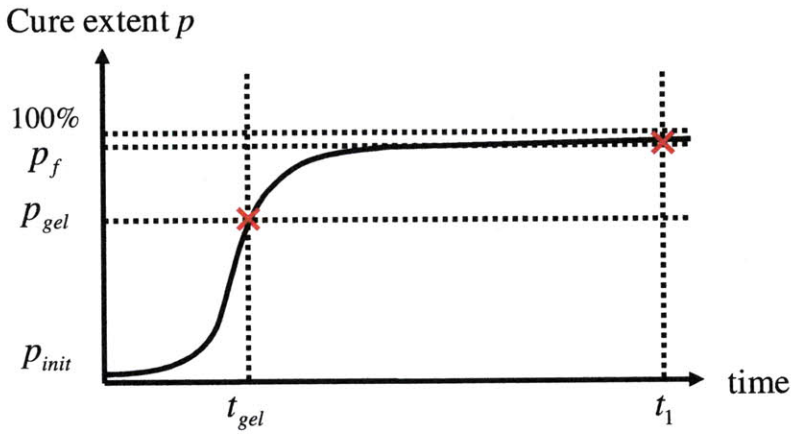

Figure 5-2: Additional cure time after gelation can be much longer than before gelation.

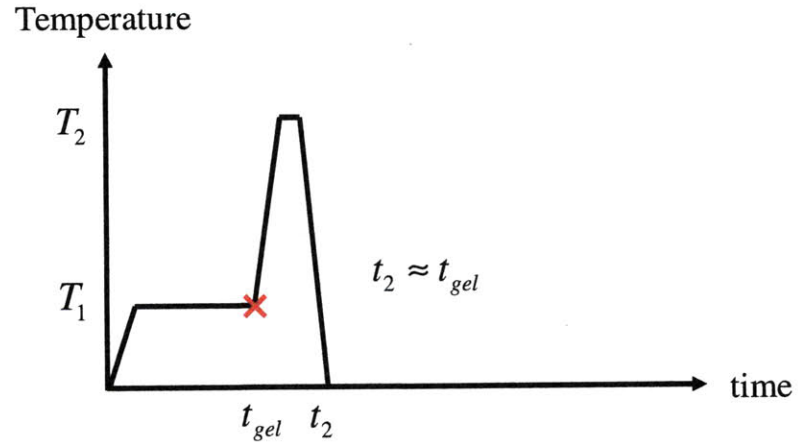

Figure 5-3: Faster two temperature cure process.

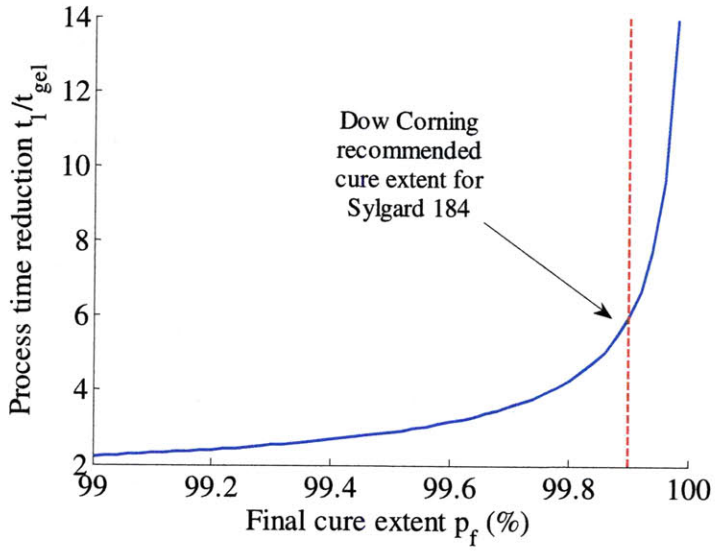

Figure 5-4: Potential factor of process time reduction for various target cure extents.

times. For more conservative cures beyond 99.9%, the factor of process time reduction increases further and the benefits of a two temperature cure is even larger. A conservative estimate of Equation (5.1) is found by assuming $m=n=1$. This form shows the qualitative effects of changing initial cure extent p_o and the final cure extent p_f.

$$\frac{t_1}{t_{gel}} = \frac{\ln\left(\frac{p_f}{1-p_f}\right)+\ln\left(\frac{1-p_o}{p_o}\right)}{\ln\left(\frac{p_{gel}}{1-p_{gel}}\right)+\ln\left(\frac{1-p_o}{p_o}\right)} \tag{5.2}$$

First, as the desired final cure extent approaches 100%, the ratio in Equation (5.2) increases. This applies for applications where aging effects are problematic. Since the reaction rate decreases as cure extent approaches 100%, it takes much more time to reach the final cure extent. Second, as p_o approaches zero the right hand terms dominate and the ratio approaches unity. The initial cure extent is a material parameter, but pre-cures can increase its effective value, which will be discussed in Section 5.4.

5.2.2 Cure time reduction in the mid and high temperature regimes

If the process is not isothermal, the process times for both single and two temperature processes will increase. As shown in Figure 4-16, the polymer temperature in a single temperature hold process is overestimated with an isothermal approximation, but more so when $t < t_{gel}$ than when $t_{gel} < t < t_1$. Consequently, the isothermal factor of reduction in Equation (5.1), t_1/ t_{gel}, becomes an overestimation of the true ratio and there is less incentive to implement a two temperature hold process. Furthermore, since gelation occurs before thermal equilibrium, the gel temperature is more sensitive to the gel time, and consequently more sensitive to process variations.

5.3 Experimental Setup and Results

Several experiments were performed to validate that a two temperature process can indeed maintain the same dimensional quality as a one temperature process. As with Section 4.3.2, curvature can be used to quantify the dimensional results, and is preferable to lateral

shrinkage measurements because the measurement technique is continuous, and not localized to a small portion of the sample. Figure 5-5 shows the control case, where a single temperature cure process was performed at 85C, and held beyond a cure extent of 99.9%. The green line indicates the gel time predicted by the gelation model, the red line indicates the time to reach 99.9% cure, and the blue line represents the actual process time. Twelve 2.7 mm PDMS samples were prepared and measured, and their mean and standard deviation are plotted in Figure 5-5.

Figure 5-6 shows a two temperature process, where the transition to the second temperature occurs before gelation. Consequently, the gel temperature will be a value between the blue and green lines. In other words, if the transition is very fast, the gel temperature will be the same as a single temperature process with process temperature of T_2. As the transition point approaches the gel point, the gel temperature approaches that of T_1. In these experiments, T_1 was 85C and held for different times t_1 less than t_{gel}. At time t_1, the parts were moved to a hotplate with a T_2 temperature of 135C, and held for 15 minutes to finish the cure. At 135C, PDMS cures from 67% to 99.9% in less than 3 minutes. The additional heating time at 135C accommodated for any heating lag to ensure that all products were fully cured. For each time t_1, six 2.7 mm PDMS samples were prepared and measured.

Figure 5-7 shows the two temperature process when the transition occurs after gelation. Now the gel temperature is similar to that of the control case in Figure 5-5. Again, T_1 was set to 85C, but now held for different t_1 times greater than t_{gel}. The second temperature T_2 remained at 135C and samples were again held for 15 minutes to bring the cure extent far beyond the 99.9% control case. For each time t_1, six 2.7 mm PDMS samples were prepared and measured.

5.4 Summary

The means and one standard deviation intervals for all three cases are summarized in Figure 5-7. There is a sharp decrease in curvature as t_1 becomes greater than t_{gel}, and becomes very similar to the single temperature control case. Consequently, a two temperature cure that holds the first temperature past the gel time will have comparable quality with a single temperature cure held five times longer. If curing can be performed isothermally, the factor improvement is equal at all temperatures. In Figure 5-8, cure times are then reduced from the red line to the green line, and cures above 85C can be performed in under 10 minutes.

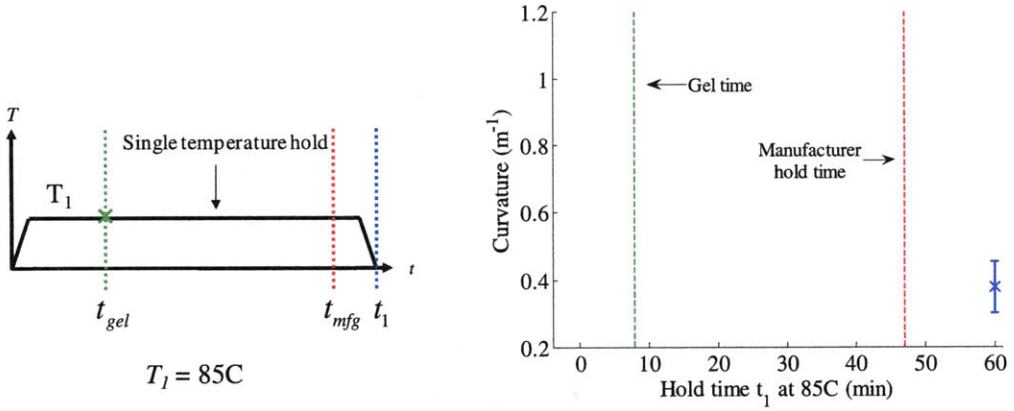

Figure 5-5: The control case is taken where the sample is heated past manufacturer specifications at a single temperature.

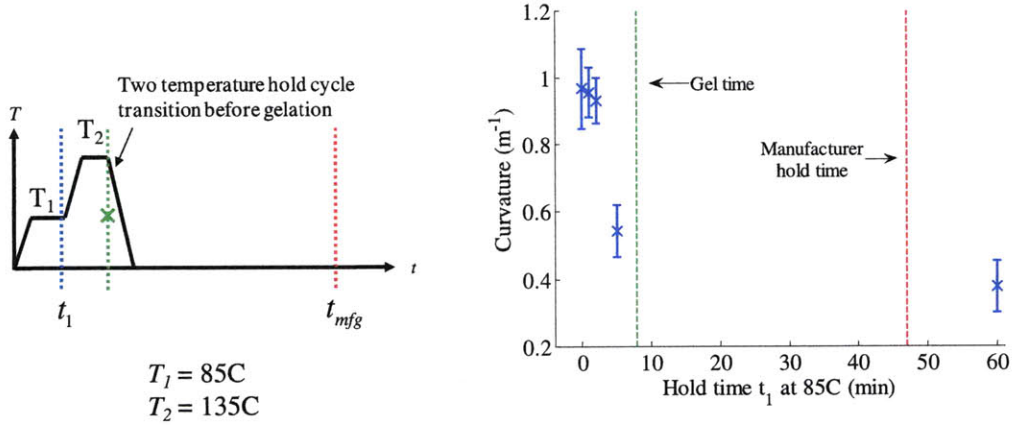

Figure 5-6: When the temperature transition occurs before the original gel point, the gel temperature will be higher than the original hold temperature.

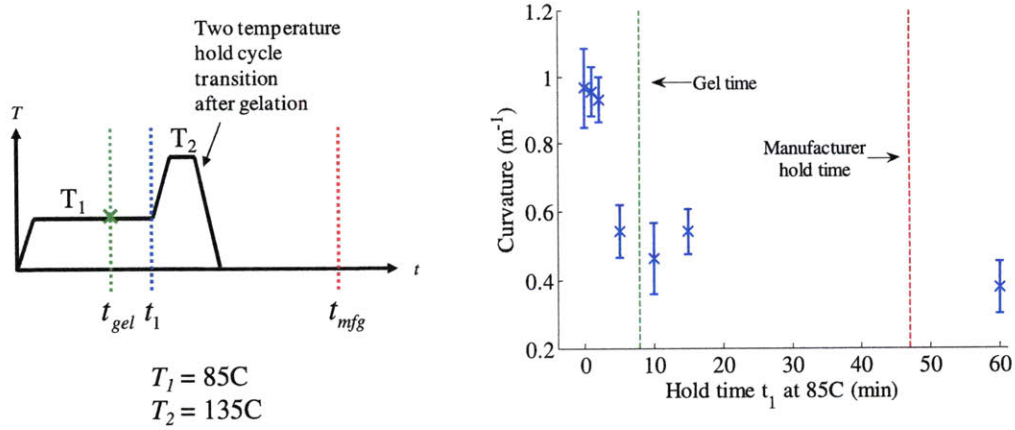

Figure 5-7: When the temperature transition occurs after the original gel point, the gel temperature will be nearly equal to the original hold temperature.

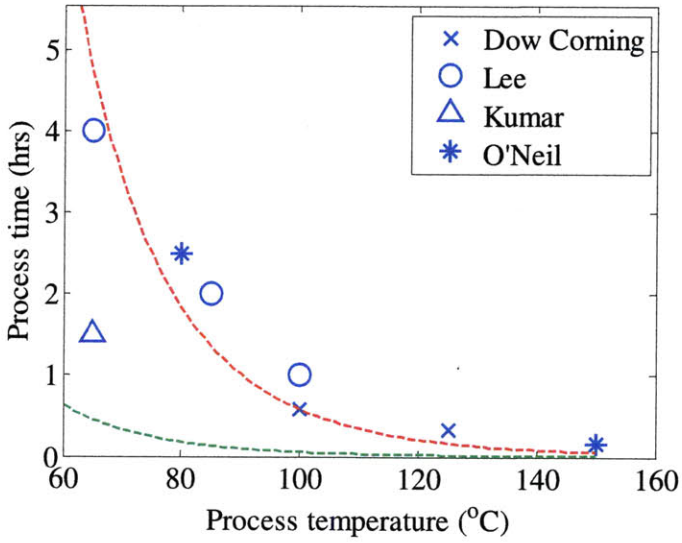

Figure 5-8: The difference between manufacturer specifications for hold time and the gel time is over a 5X improvement if curing occurs isothermally.

The gel point has been identified as a sharp transition point at which the dimensionality of the part is locked in. Section 5.2.1 showed that changes in initial cure extent can also have a significant impact in the reduction of total cure time. One possibility is to increase this initial cure extent quickly at an elevated temperature without crossing the gel point. After cooling the part down back to a target cure temperature, it should be held until it crosses the new gel point, after which the same high temperature post-cure can be applied to finish curing the part. This is schematically shown in Figure 5-9. The maximum potential process time reduction of increasing initial cure extents from a two temperature process can be seen in Figure 5-10, and is calculated as the ratio of the current gel time to the gel time from a larger initial cure extent p_o. As p_o approaches p_{gel}, the new gel time (t_{gel} - t_{po}) approaches zero. However, care should be taken such that gelation does not occur during the pre-cure step, so heating and cooling transients may account for the bulk of the process time. These transient times can be approximated by combining the lumped parameter model in Section 4.4.3, with the time constant of the heating mechanism. Thin parts with fast heater control systems will benefit most from a three temperature cure process.

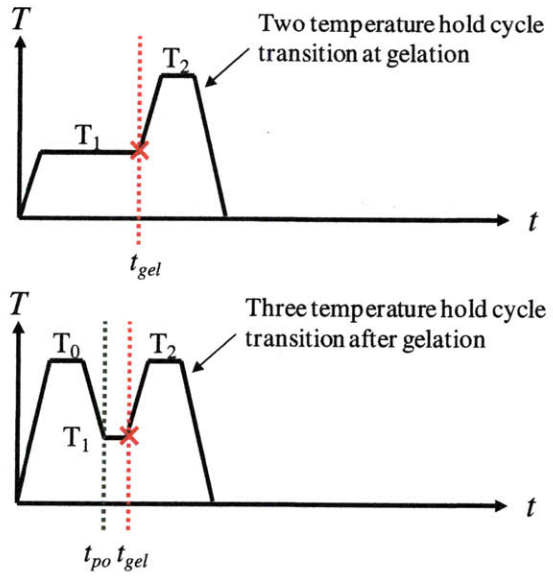

Figure 5-9: Potential three stage curing for process time improvement.

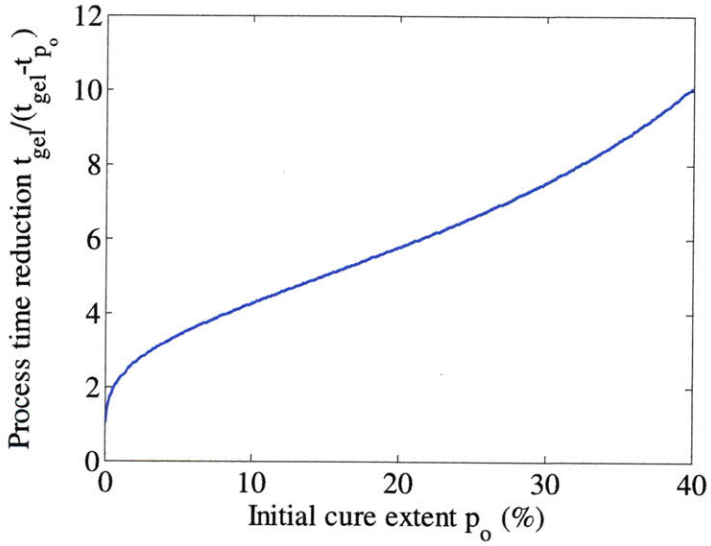

Figure 5-10: Potential factor of process time reduction by varying initial cure extents.

Nomenclature

p = cure extent
p_{gel} = cure extent at gelation
p_o = initial cure extent
p_f = final cure extent at process completion
t_1 = time for first temperature hold [s]
t_o = time at the initial cure extent (typically zero) [s]
t_{p_o} = time at the new initial cure extent [s]
t_{gel} = time at gelation [s]
t_{mfg} = recommended cure time from the manufacturer [s]
T_0 = process temperature for increasing the initial cure extent [K]
T_1 = process temperature for first temperature hold [K]
T_2 = process temperature for second temperature hold [K]
T_{gel} = gel temperature [K]

CHAPTER 6

CONCLUSION

Although PDMS continues to be used extensively in research environments, little previously has been understood about how to systematically design a PDMS microfluidic device for manufacturing. The absence of this knowledge has hitherto kept many PDMS devices from being seriously considered for mass manufacturing. This thesis serves to quash some of the uncertainty involved with PDMS manufacturing, by quantifying and controlling important factors during cure, namely the stability of modulus in PDMS parts and the process-induced dimensional variability.

In Chapter 2, a statistical mechanics approach is applied to model the time evolution of modulus during cure. A Pade approximant is used to improve the Arruda-Boyce eight chain network model for rubbers such as PDMS, which have small locking stretches. This enables device designers to predictably alter the modulus of their device by changing the mixing composition of pre-polymer. This also enables mechanical testing methods to be utilized to measure modulus during cure, and return the gel point and the cure extent of the process. Chapter 3 experimentally validates the modulus relations described in Chapter 2. First, tension and durometer experiments on fully cured PDMS are analyzed, and validate the model developed for small locking stretch materials. Next, heated micro-indentation is shown to measure modulus during cure. These experiments show that the gel point can indeed be observed, and that the model developed for the time evolution of modulus is correct.

In Chapter 4, a detailed study on shrinkage and curvature is performed on PDMS. The temperature at the gel point is found to describe the process-induced shrinkage and curvature. Simple models show that the gel temperature can be well approximated by the temperature at thermal equilibrium for low reaction rate cures. Models based on thermal equilibrium are found to be insufficient, and motivate the need for more complex models. These analytical and

numerical models are presented that are more applicable at higher temperature cures, and show how shrinkage and curvature are related to process temperature. Generation of these shrinkage and curvature relationships can be used to determine the process temperature that should be used for devices designed with certain shrinkage or curvature specs.

Finally, faster cure schedules are described in Chapter 5, which utilize the ability to identify the gel point. Once the part is cured to gelation, the process temperature can be altered to complete the cure process, while preserving the dimensional accuracy of the original design. The cure extent recommended by Dow Corning for Sylgard 184 is determined to be approximately 99.9%, and curing beyond the gel point can reduce the cure process time by five times, compared with a single temperature cure process to the same 99.9% cure extent. Because aging effects are observed at the manufacturer recommended cure extent, higher cure extents should be used for modulus sensitive devices. The reduction in cure time is consequently higher. Once cured past gelation, curvature is observed to be similar for any subsequent heating profiles.

6.1 Contributions of this Thesis

6.1.1 Rational process design for PDMS manufacturing

The main contribution of this work is a methodology for designing PDMS devices that can be rapidly manufactured. Shrinkage and curvature are shown to be directly linked to the process temperature, and consequently to the minimum total cure time that can be achieved. The subsequent aging that can be tolerated is also shown to have a direct impact on the cure time that is necessary. For parts that are insensitive to modulus changes, the total cure time can be significantly shortened. By considering shrinkage and curvature, and modulus requirements, chip designers are capable of creating faster manufacturable chips across different heating platforms, which preserve the dimensional accuracy of their original design.

6.1.2 Systematic modeling of polymerization

Gelation is found to impact the dimensional accuracy of the final part. Consequently, a systematic approach to modeling polymerization is provided to determine the spatial and temporal distribution of cure extent. The gelation temperature at each point can then be combined to determine the total thermal strain on the part when it cools back down after cure,

and produce a measure of shrinkage and curvature. By modeling the dependence of shrinkage and curvature on process temperature, this thesis can provide guidance into the process temperatures that should be used.

6.1.3 Novel experimental technique for gel point detection in thin films

Mechanical testing methods can be utilized to measure modulus during cure, and calculate the gel point and the cure extent of the process. Several mechanical test equipments exist to measure modulus, but none are capable of measuring a thin polymer as it cures from a liquid to solid state. A novel heated micro-indentation setup is proposed and shown to accomplish this feat. In situ monitoring of cure can provide real-time feedback into the state of the cure process, detect the gel point, and estimate when the cure process is complete.

6.1.4 Analytical and numerical models for determination of gel point

Although numerical models have been produced to model cure extent in composites, simpler models are proposed that are less computationally intensive, and can provide immediate insight into the time dependence of parameters such as process temperature. For Sylgard 184 mixed at a base to curing agent ratio of 10:1, the time to gelation is shown to increase approximately two times for every 10C decrease in polymer temperature. Determination of gel point also enables multi-temperature cure schedules to be designed that are significantly faster than current single temperature cure cycles.

6.1.5 Shrinkage and curvature study for PDMS

Shrinkage is commonly observed in PDMS processing, and usually calibrated for in the design. From a lack of shrinkage data in the literature, researchers have incorrectly assumed shrinkage to be a linear function of process temperature. This thesis is the first to examine shrinkage for a process temperature range in excess of 100C, and find the relationship to be linear with gel temperature and not process temperature. Furthermore, out of plane gel temperature gradients is found to also impact the curvature of the part, which has not been reported in the past.

6.2 Future Work

6.2.1 Concurrent pre-cure and degassing

Gelation temperature was found to be critical in determining the shrinkage and curvature of a produced part. A two temperature strategy was shown to increase the cure rate after gelation, and a three temperature strategy was proposed as a potential way to increase the cure rate before gelation as well. This three temperature cure model can potentially be performed in parallel during the degassing step of the PDMS manufacturing process. Because viscosity increases as cure approaches gelation, an interesting problem is to study the tradeoffs with centrifugal degassing [12] at higher cure extents, and potentially find optimal process conditions for concurrent pre-cure and degassing.

6.2.2 Assembly and bonding processes

PDMS was selected for this thesis because of its common use in research environments. As such, most of the assembly and bonding work has been done by hand and has been dependent on the skill of the operator. A more in depth study on automation in assembly and bonding can yield insight into how bond strength decreases with curvature. The quantitative impact of curvature on assembly can provide new constraints on the process conditions that are tolerable during the cure process.

6.2.3 Radiation curing

Dow Corning has attempted some work with microwave radiation for faster and more uniform cures. They have used a variable frequency microwave to transfer energy into the pre-polymer (Lambda Technologies, Inc, 860 Aviation Parkway, Suite 900, Morrisville, NC 27560, 888-290-2873). Radiation heating provides an interesting alternative to conduction, since it can be toggled on or off instantaneously. And with radiation curing from the top surface, the concavity of the resultant curvature may be advantageous for assembly.

REFERENCES

[1] S. C. Terry, J. H. Jerman and J. B. Angell, "A gas chromatographic air analyzer fabricated on a silicon wafer," *IEEE Trans. Electron Devices,* vol. 26, pp. 1880-1886, 1979.

[2] G. M. Whitesides, "The origins and the future of microfluidics," *Nature,* vol. 442, pp. 368-373, 2006.

[3] S. N. Korb, Massachusetts Institute of Technology and Dept. of Mechanical Engineering, *Towards the Manufacturing of Microfluidic Devices: Fluid Flow in Multilayer Devices as a Test Case,* 2006.

[4] Y. Chen, E. E. Roller and X. Huang, "DNA sequencing by denaturation: experimental proof of concept with an integrated fluidic device," *Lab on a Chip,* vol. 10, pp. 1153-1159, 2010.

[5] J. O. Tegenfeldt, C. Prinz, H. Cao, R. L. Huang, R. H. Austin, S. Y. Chou, E. C. Cox and J. C. Sturm, "Micro-and nanofluidics for DNA analysis," *Analytical and Bioanalytical Chemistry,* vol. 378, pp. 1678-1692, 2004.

[6] D. T. Chiu, N. L. Jeon, S. Huang, R. S. Kane, C. J. Wargo, I. S. Choi, D. E. Ingber and G. M. Whitesides, "Patterned deposition of cells and proteins onto surfaces by using three-dimensional microfluidic systems," *Proceedings of the National Academy of Sciences,* vol. 97, pp. 2408, 2000.

[7] A. Ulman, "Formation and structure of self-assembled monolayers," *Chem. Rev.,* vol. 96, pp. 1533-1554, 1996.

[8] D. E. Hardt, B. W. Anthony and S. B. Tor, "A teaching factory for polymer microfabrication - μFac," in *6th International Symposium on Nanomanufacturing,* Athens, Greece, 2008, .

[9] E. Wong, S. Kumar, A. Mazzeo, J. H. Chun and D. E. Hardt, "Functional test system design for microfluidic applications," in *10th Anniv Singapore-MIT Alliance Symposium,* 2009, .

[10] H. Becker and C. Gärtner, "Polymer microfabrication methods for microfluidic analytical applications," *Electrophoresis,* vol. 21, pp. 12-26, 1999.

[11] M. E. Dirckx, "Design of a fast cycle time hot micro-embossing machine," 2005.

[12] A. D. Mazzeo, "Centrifugal Casting and Fast Curing of Polydimethylsiloxane (PDMS) for the Manufacture of Micro and Nano Featured Components," 2009.

[13] D. Armani, C. Liu and N. Aluru, "Re-configurable fluid circuits by PDMS elastomer micromachining," in *Twelfth IEEE International Conference on Micro Electro Mechanical Systems, 1999. MEMS'99,* 1999, pp. 222-227.

[14] D. T. Eddington, W. C. Crone and D. J. Beebe, "Development of process protocols to fine tune polydimethylsiloxane material properties," *7th International Conference on Miniaturized Chemical and Biochemical Analysis Systems,* 2003.

[15] F. Chambon and H. H. Winter, "Linear viscoelasticity at the gel point of a crosslinking PDMS with imbalanced stoichiometry," *J. Rheol.,* vol. 31, pp. 683, 1987.

[16] S. K. Venkataraman, L. Coyne, F. Chambon, M. Gottlieb and H. H. Winter, "Critical extent of reaction of a polydimethylsiloxane polymer network," *Polymer,* vol. 30, pp. 2222-2226, 1989.

[17] A. Kumar and G. M. Whitesides, "Features of gold having micrometer to centimeter dimensions can be formed through a combination of stamping with an elastomeric stamp and an alkanethiol ''ink''followed by chemical etching," *Appl. Phys. Lett.,* vol. 63, pp. 2002, 1993.

[18] Y. Xia and G. M. Whitesides, "Soft lithography," *Angew.Chem.Int.Ed,* vol. 37, pp. 550-575, 1998.

[19] Dow Corning Product Information, "Information about Dow Corning® brand Silicone Encapsulants," 2005.

[20] S. W. Lee and S. S. Lee, "Shrinkage ratio of PDMS and its alignment method for the wafer level process," *Microsystem Technologies,* vol. 14, pp. 205-208, 2008.

[21] M. A. Unger, H. P. Chou, T. Thorsen, A. Scherer and S. R. Quake, "Monolithic Microfabricated Valves and Pumps by Multilayer Soft Lithography," *Science,* vol. 288, pp. 113-116, 2000.

[22] T. Thorsen, S. J. Maerkl and S. R. Quake, "Microfluidic Large-Scale Integration," *Science,* vol. 298, pp. 580-584, 2002.

[23] E. Leclerc, Y. Sakai and T. Fujii, "Cell culture in 3-dimensional microfluidic structure of PDMS (polydimethylsiloxane)," *Biomed. Microdevices,* vol. 5, pp. 109-114, 2003.

[24] E. Leclerc, Y. Sakai and T. Fujii, "Microfluidic PDMS (polydimethylsiloxane) bioreactor for large-scale culture of hepatocytes," *Biotechnol. Prog.,* vol. 20, pp. 750-755, 2008.

[25] H. Becker, "Polymer microfabrication - an industrialist view," 2009.

[26] T. C. Merkel, V. I. Bondar, K. Nagai, B. D. Freeman and I. Pinnau, "Gas sorption, diffusion, and permeation in poly (dimethylsiloxane)," *Journal of Polymer Science Part B: Polymer Physics,* vol. 38, pp. 415-434, 2000.

[27] S. H. Choi, J. H. Kim and S. B. Lee, "Sorption and permeation behaviors of a series of olefins and nitrogen through PDMS membranes," *J. Membr. Sci.,* vol. 299, pp. 54-62, 2007.

[28] J. R. Anderson, D. T. Chiu, R. J. Jackman, O. Cherniavskaya, J. C. McDonald, H. Wu, S. H. Whitesides and G. M. Whitesides, "Fabrication of Topologically Complex Three-Dimensional Microfluidic," *Anal. Chem.,* vol. 72, pp. 3158-3164, 2000.

[29] S. R. Quake and A. Scherer, "From Micro- to Nanofabrication with Soft Materials," *Science,* vol. 290, pp. 1536-1540, 2000.

[30] A. M. Kendale and D. L. Trumper, *Microcontact Printing,* 2006.

[31] S. Krishnan and S. E. Sarma, "On the manufacture of very thin elastomeric films by spin-coating," 2007.

[32] J. W. Munyan, H. V. Fuentes, M. Draper, R. T. Kelly and A. T. Woolley, "Electrically actuated, pressure-driven microfluidic pumps," *Lab on a Chip,* vol. 3, pp. 217-220, 2003.

[33] A. Folch, S. Mezzour, M. Du¨ ring, O. Hurtado, M. Toner and R. Mu¨ ller, "Stacks of microfabricated structures as scaffolds for cell culture and tissue engineering," *Biomed. Microdevices,* vol. 2, pp. 207-214, 2000.

[34] J. A. Rogers, K. E. Paul and G. M. Whitesides, "Quantifying distortions in soft lithography," *Journal of Vacuum Science & Technology B: Microelectronics and Nanometer Structures,* vol. 16, pp. 88, 1998.

[35] R. C. Huang and L. Anand, "Non-linear elastic response of Poly(dimethylsiloxane) (PDMS) as a function of composition, curing time and curing temperature," 2005.

[36] Y. Xia, E. Kim, X. M. Zhao, J. A. Rogers, M. Prentiss and G. M. Whitesides, "Complex optical surfaces formed by replica molding against elastomeric masters," *Science,* vol. 273, pp. 347, 1996.

[37] A. Kumar, H. A. Biebuyck and G. M. Whitesides, "Patterning self-assembled monolayers: applications in materials science," *Langmuir,* vol. 10, pp. 1498-1511, 1994.

[38] A. O'Neill, J. S. Hoo and G. Walker, "Chips & Tips: Rapid curing of PDMS for microfluidic applications," *Lab on a Chip,* 2008.

[39] G. G. Odian, *Principles of Polymerization.* Wiley-Interscience, 2004.

[40] S. K. Venkataraman and H. H. Winter, "Finite shear strain behavior of a crosslinking polydimethylsiloxane near its gel point," *Rheologica Acta,* vol. 29, pp. 423-432, 1990.

[41] L. R. G. Treloar, "The elasticity and related properties of rubbers," *Reports on Progress in Physics,* vol. 36, pp. 755-826, 1973.

[42] M. C. Wang and E. Guth, "Statistical Theory of Networks of Non-Gaussian Flexible Chains," *J. Chem. Phys.,* vol. 20, pp. 1144, 1952.

[43] P. J. Flory and J. Rehner Jr, "Statistical Mechanics of Cross-Linked Polymer Networks I. Rubberlike Elasticity," *J. Chem. Phys.,* vol. 11, pp. 512, 1943.

[44] E. M. Arruda and M. C. Boyce, "Characterization of the strain hardening response of amorphous polymers," 1992.

[45] E. M. Arruda and M. C. Boyce, "A three-dimensional constitutive model for the large stretch behavior of rubber elastic materials," *J. Mech. Phys. Solids,* vol. 41, pp. 389-389, 1993.

[46] W. Kuhn and F. Grun, "Relationships between elastic constants and stretching double refraction of highly elastic substances," *Kolloid Z,* vol. 101, pp. 248, 1942.

[47] H. M. James and E. Guth, "Theory of the elastic properties of rubber," *J. Chem. Phys.,* vol. 11, pp. 455, 1943.

[48] B. P. Gearing, "Constitutive equations and failure criteria for amorphous polymeric solids," *Massachusetts Institute of Technology,* 2002.

[49] A. Cohen, "A Padé approximant to the inverse Langevin function," *Rheologica Acta,* vol. 30, pp. 270-273, 1991.

[50] R. C. Huang and L. Anand, "Non-linear mechanical behavior of the elastomer polydimethylsiloxane (PDMS) used in the manufacture of microfluidic devices," 2005.

[51] H. J. Qi, K. Joyce and M. C. Boyce, "Durometer hardness and the stress-strain behavior of elastomeric materials," *Rubber Chemistry and Technology,* vol. 76, pp. 419-435, 2003.

[52] I. N. Sneddon, "The relation between load and penetration in the axisymmetric Boussinesq problem for a punch of arbitrary profile," *Int. J. Eng. Sci.,* vol. 3, pp. 47–57, 1965.

[53] B. J. Briscoe, K. S. Sebastian and M. J. Adams, "The effect of indenter geometry on the elastic response to indentation," *Journal of Physics-London-D Applied Physics,* vol. 27, pp. 1156-1156, 1994.

[54] W. C. Oliver and G. M. Pharr, "Improved technique for determining hardness and elastic modulus using load and displacement sensing indentation experiments," *J. Mater. Res.,* vol. 7, pp. 1564-1583, 1992.

[55] J. A. Rogers, Z. Bao, K. Baldwin, A. Dodabalapur, B. Crone, V. R. Raju, V. Kuck, H. Katz, K. Amundson and J. Ewing, "Paper-like electronic displays: Large-area rubber-stamped plastic sheets of electronics and microencapsulated electrophoretic inks," *Proc. Natl. Acad. Sci. U. S. A.,* vol. 98, pp. 4835, 2001.

[56] K. M. Choi and J. A. Rogers, "A photocurable poly (dimethylsiloxane) chemistry designed for soft lithographic molding and printing in the nanometer regime," *J. Am. Chem. Soc.,* vol. 125, pp. 4060–4061, 2003.

[57] H. Schmid and B. Michel, "Siloxane Polymers for High-Resolution, High-Accuracy Soft Lithography," *Macromolecules,* vol. 33, pp. 3042-3049, 2000.

[58] A. Kocabas and A. Aydinli, "Polymeric waveguide Bragg grating filter using soft lithography," *Phys.Lett,* vol. 79, pp. 3576-3578, 2001.

[59] S. Olcum, A. Kocabas, G. Ertas, A. Atalar and A. Aydinli, "Tunable surface plasmon resonance on an elastomeric substrate," *Opt.Express,* vol. 17, pp. 8542-8547, 2009.

[60] B. Michel, A. Bernard, A. Bietsch, E. Delamarche, M. Geissler, D. Juncker, H. Kind, J. P. Renault, H. Rothuizen and H. Schmid, "Printing meets lithography: Soft approaches to high-resolution patterning," *IBM J.Res.Dev,* vol. 45, pp. 697–719, 2001.

[61] Y. Srivastava, C. Rhodes, M. Marquez and T. Thorsen, "Electrospinning hollow and core/sheath nanofibers using hydrodynamic fluid focusing," *Microfluidics and Nanofluidics,* vol. 5, pp. 455-458, 2008.

[62] S. Pagliara, L. Persano, A. Camposeo, R. Cingolani and D. Pisignano, "Registration accuracy in multilevel soft lithography," *Nanotechnology,* vol. 18, pp. 175302, 2007.

[63] O. Haruyama, Y. Nakayama, R. Wada, H. Tokunaga, J. Okada, T. Ishikawa and Y. Yokoyama, "Volume and enthalpy relaxation in Zr55Cu30Ni5Al10 bulk metallic glass," *Acta Materialia,* 2009.

[64] N. Sbirrazzuoli, D. Brunel and L. Elegant, "Different kinetic equations analysis," *Journal of Thermal Analysis and Calorimetry,* vol. 38, pp. 1509-1524, 1992.

[65] K. J. Bathe, "Finite Element Procedures," *Englewood Cliffs,* 1996.